Thin Film Growth, Structural and Magnetic Studies of Magnetic Nanocrystalline Topological Insulators





Joshua Bibby

St. Catherine's College

University of Oxford

A thesis submitted for the degree of

Doctor of Philosophy

Acknowledgments

The proverb 'it takes a village to raise a child' also feels apt for a DPhil student, and as such there are many people to thank for their contributions. Firstly, my supervisor, Prof. Thorsten Hesjedal, who guided projects, edited written work, and found solutions to problems when I was unable to do so. Without his help I would have found myself stranded, and I am very grateful for his contributions. Additionally, Prof. Gerrit van der Laan, despite not holding formal supervisory responsibility for me, generously provided very useful advice on the acquisition and analysis of XMCD/LD data, and his contributions enabled effective magnetic characterisation of thin films. In addition to more supervisory roles, Dr. Angadjit Singh and Dr. Barat Achinuq provided support with training on equipment, help with measurement plans, and day-to-day guidance on how to conduct my studies to ensure I made the most of my time. Their willingness to put in time outside of their own work helped immensely in getting me settled at Oxford, and their departure from the group was felt. I have no doubt I still had much to learn from them both. My fellow DPhil students, Jack Bollard, Emily Heppell, and Ethan Arnold, also assisted me a great deal, taking night shifts on beamtimes, helping me write Python scripts, and dealing with many a lunchtime rant when results were not as expected. It was truly a pleasure to work with everyone in this research group, where every member brought their own expertise, and their company made the most stressful

points manageable.

Beyond my direct colleagues, I would like to thank all the scientists and support staff at shared user facilities, particularly the staff at the I10 and I06 beamlines at the Diamond Light Source, BL29 at ALBA, and ID32 at ESRF. The job of coming in to fix a beamline at two in the morning because your users tried to change something in the middle of the night is one I do not envy! However, without their efforts, this thesis would not contain some essential data, so I am very grateful for their hard work.

Outside of the lab, I have to thank all my friends, family, loved ones and teammates for their support. Your contributions come in thousands of moments that allowed me to forget about the stress of research, providing the grounding I needed to refocus and tackle my work with a clear mind. Final and special thanks are due to my parents, Hugo and Wendy, who, as always, wore many hats while helping me through these four years, acting as proofreaders, personal chefs, therapists, chauffeurs, and supporters. It's been a very long time since the evenings you spent reading a children's science encyclopedia to me; your support from then to now has been invaluable every step of the way, and I couldn't be more grateful.

To every single one of you mentioned, the most sincere and heartfelt thanks are given. These four years have been a truly exciting time, and every one of you played a role in making that happen.

Abstract

Topological insulators (TIs) are a class of material which are bulk insulators but house conducting surface states protected by bulk band topology. These states are spin-momentum locked, gapless, and resistant to scattering off impurities that do not break time-reversal symmetry. In terms of band structure, the surface band dispersion is defined by a Dirac cone at time reversal invariant momenta points. However, the introduction of ferromagnetic order via transition metal doping, and therefore the breaking of time reversal symmetry, will open up a bandgap. This symmetry breaking allows for the observation of emergent phenomena, such as the quantum anomalous Hall effect (QAHE), axion insulators, and Majorana edge states. In addition, owing to spin-momentum locking of the surface states, TIs provide an excellent platform for generating high spin-orbit torques, which are ideal for applications in spintronic memory and logic devices.

However, issues have persisted in realising the potential of TIs experimentally. Firstly, the QAHE can currently only be observed in TIs at very low temperatures, as well as intrinsic defects increasing bulk conductivity, which suppresses the relative contributions of surface states that give rise to the more novel physics. The increase in bulk conductivity reduces the proportion of injected current flowing through the surface states, therefore reducing the charge-to-spin conversion efficiency and the spin-orbit torques required for high-performance devices.

Attempts to resolve these issues by pushing for ultra-high-quality films have proven unsuccessful, with defect densities remaining too high. However, an alternative approach, focusing on a high defect density to the point of nanocrystallinity, offers a potential solution. As the surface states sit slightly below the surface, small grains within a film remove much of the bulk state, therefore enhancing the effect of the spin-momentum locked states.

This thesis focuses on the growth and characterisation of magnetic TI thin films produced using magnetron sputtering, enabling nanocrystalline growth modes. Results showing structural and magnetic measurements of Mn-doped Bi_2Te_3 and Cr-doped Sb_2Te_3 both exhibited pairs of magnetic transitions at ∼10 and 43.3 K, and ∼38 and 82 K, respectively. These pairs of magnetic transitions indicate the structural inhomogeneities present in both materials, with secondary phases and variable dopant distribution resulting in a more complex magnetic state.

In addition to standard magnetic TIs, $MnBi_2Te_4$ was studied. In this case, magnetic ions are directly incorporated into the lattice. This is of particular interest due to the A-type antiferromagnetism exhibited by the film, where the number of septuple-layer stacking units determines whether the film is fully compensated or uncompensated, supporting the QAHE and axion insulator states, respectively. Owing to the thickness sensitivity of the film's properties, literature has shown that it is challenging to measure these states using techniques such as X-ray magnetic spectroscopy. Due to the difference in nucleation compared to other techniques, this issue is potentially resolved by sputtering. Growing $MnBi_2Te_4$ thin films resulted in a film with sub-nanometer roughness and magnetic transition temperatures of ∼8 and 30 K measured by SQUID magnetometry. These two transitions are indicative of an antiferromagnetic and ferromagnetic phase; however,

x-ray magnetic linear dichroism displayed no certain results, suggesting that residual disorder disrupts the interlayer coupling enough to destabilise the antiferromagnetic order.

Finally, the spin-orbit torque efficiency of undoped Bi_2Te_3 was tested at room temperature using a Bi_2Te_3-$Ni_{20}Fe_{80}$ bilayer device. This resulted in a spin Hall angle of $\theta_H = 4.4 \pm 5.7$, measured using anomalous and planar Hall effects, which is comparable to existing literature considering the thickness of the ferromagnetic layer used. However, due to issues with the method used and compounding errors from measuring the individual thickness of the layers, the results exhibited a very high error.

Overall, the work demonstrates the viability of nanocrystalline TIs and doping with transition metals, yielding nanocrystalline ferromagnetic films. Additionally, the viability of sputter growth of the intrinsic magnetic topological insulator $MnBi_2Te_4$ was established, giving potential for the observation of a thin film antiferromagnetic TI. However, impurities and structural discontinuities still limit the observation of emergent phenomena, with further refinement required to explore the full potential of nanocrystalline TIs.

Publications

D. M. Burn, J. C. Lin, R. Fujita, B. Achinuq, J. Bibby, A. Singh, A. Frisk, G. van der Laan, and T. Hesjedal, *Spin pumping through nanocrystalline topological insulators*, Nanotechnology, **34**, 27, 275001 (2023).

J. Bibby, A. Singh, E. Heppell, J. Bollard, B. Achinuq, S. J. Haigh, G. van der Laan, and T. Hesjedal, *Synthesis of Nanocrystalline Mn-doped Bi_2Te_3 Thin Films via Magnetron Sputtering*, Crystals, **15**, 54 (2025).

J. Bibby, E. Heppell, J. Bollard, E. L. Arnold, J. Herrero-Martín, G. van der Laan, and T. Hesjedal, *Sputter-Grown $MnBi_2Te_4$ Thin Films: Magnetic Ground States and Phase Control*, physica status solidi (RRL), 19:e2500329 (2025).

J. Bibby, A. Singh, E. Heppell, J. Bollard, B. Achinuq, J. C. A. do Nascimento, C. Murrill, V. K. Lazarov, G. van der Laan, and T. Hesjedal, *Structural and Magnetic Properties of Sputtered Chromium-Doped Sb_2Te_3 Thin Films*, Crystals, **15**, 896 (2025).

Contents

1 Introduction and Theory **1**

1.1 Introduction 1

1.2 Theoretical Discussion 2

1.2.1 Hall and Quantum Hall Effects 2

1.2.2 Spin and Anomalous Hall Effect 5

1.2.3 Quantum Spin Hall Effect 6

1.2.4 3D Topological Insulators 7

1.2.5 Time Reversal Symmetry and Quantum Anomalous Hall Effects . 12

1.3 Outline of Thesis 13

2 Methodology **15**

2.1 Magnetron Sputtering 15

2.1.1 DC Magnetron Sputtering 15

2.1.2 RF Magnetron Sputtering 20

2.2 Structural Characterization Techniques 20

2.2.1 X-ray Diffraction 20

2.2.2 X-Ray Reflectivity 23

2.2.3 Atomic Force Microscopy 25

2.2.4 Scanning Electron Microscopy and Energy Dispersive X-ray Spectroscopy . . . 26
2.2.5 Scanning Transmission Electron Microscopy . . . 29
2.3 Magnetic Characterization Techniques . . . 31
2.3.1 SQUID Vibrating Sample Magnetometry . . . 31
2.3.2 X-ray Magnetic Spectroscopy . . . 33
2.4 Growth of Topological Insulators . . . 39
2.4.1 Bismuth Telluride and Antimony Telluride . . . 40
2.4.2 Substrate Selection and Preparation . . . 40
2.4.3 Establishment of a Growth Recipe for Bi_2Te_3 and Sb_2Te_3 . . . 41
2.5 UV Photolithography . . . 46

3 Transition Metal Doping of Topological Insulators 51

3.1 Motivation . . . 51
3.2 Mn-doped Nanocrystalline Bi_2Te_3 Thin Films . . . 53
3.2.1 Growth of Mn:Bi_2Te_3 Thin Films . . . 53
3.2.2 Structural Analysis of Mn:Bi_2Te_3 Thin Films . . . 55
3.2.3 Magnetic Characterization of Mn:Bi_2Te_3 Thin Films . . . 65
3.2.4 Discussion . . . 71
3.3 Cr-doping of Nanocrystalline Sb_2Te_3 Thin Films . . . 74
3.3.1 Growth of Cr-doped Thin Films . . . 74
3.3.2 Structural Characterisation of Cr:Sb_2Te_3 Films . . . 75
3.3.3 Magnetic Measurements of Cr:Sb_2Te_3 Thin Films . . . 82
3.3.4 Discussion . . . 88

4 Growth and Characterisation of the Intrinsic Mangetic Topological Insulator $MnBi_2Te_4$ 89

4.1 Motivation . . . 89

4.2 Growth of $MnBi_2Te_4$ Thin Films . . . 92

4.3 Structural Analysis . . . 93

4.4 Magnetic Characterisation . . . 97

4.5 Discussion . . . 105

5 Spin-Orbit Torque Measurements of a Nanocrystalline Topological Insulator-Ferromagnetic Bilayer 110

5.1 Motivation . . . 110

5.2 Growth and Fabrication of Bilayer Devices . . . 112

5.3 Methodology for the Determination of Spin Hall Angle . . . 116

5.4 Results . . . 119

5.5 Discussion . . . 123

6 Conclusions 126

A List of Acronyms and Abbreviations 131

B Details on the Preparation of Substrates 134

List of Figures

1.1 QHE: Simple Model of Electron Paths. 4

1.2 Illustrative Model of SHE and QSHE. 7

1.3 Diagram of Band Inversion. 8

1.4 Diagram of Band Splitting due to strong SOC. 10

1.5 Dispersion Relations with and without SOC. 11

2.1 Diagram of a Generalised Sputter System. 16

2.2 Images of the Sputter System. 17

2.3 Photographs of Substrate Holder and Manipulator. 19

2.4 Diagrams of XRD Measurement Geometries. 22

2.5 Example of XRR Data. 24

2.6 Image and Diagram of AFM Equipment. 26

2.7 Example EDS Spectrum. 28

2.8 TEM Measurement Geometry. 30

2.9 Image and Diagram of SQUID-VSM Equipment. 33

2.10 Simple model and Example of XMCD. 35

2.11 XRD of Bi_2Te_3 at Various Growth Temperatures and Substates. 44

2.12 Photograph of a UV Lithography Mask. 47

3.1 Mn-Doped Bi_2Te_3: XRD and GI-XRD for a series of Mn concentrations. 57
3.2 Asymmetric RSM Studies for a Series of Films with varying Mn Concentrations. 59
3.3 Mn-Doped Bi_2Te_3: RSM measurements of the 006 Peak. 60
3.4 Comparison of AFM Images for Undoped and Mn-Doped Bi_2Te_3. 61
3.5 EDS Maps of a Mn-Doped Sample. 62
3.6 TEM of a 1.6% Mn-Doped Bi_2Te_3. 63
3.7 TEM of a 3.8% Mn-Doped Bi_2Te_3. 64
3.8 HAADF and EDS Maps for both 1.6% and 3.8% Mn Films. 66
3.9 SQUID-VSM $M(H)$ and $M(T)$ studies on Mn-Doped Bi_2Te_3 films. . . . 67
3.10 Mn-Doped Bi_2Te_3: XMCD and Peak Asymmetry as a Function of Mn content and Comparison to Calculations. 70
3.11 XRD Measurements of a Series of Cr-Doped Sb_2Te_3 Thin Films. 76
3.12 Asymmetric RSM Studies for Cr-Doped Films. 78
3.13 HAADF-STEM of Two Cr-Doped Sb_2Te_3 Thin Films. 79
3.14 STEM and STEM-EDS Images of Two Cr-Doped Thin Films. 80
3.15 RSM Maps of Sb_2Te_3 Films with an Abnormal Crystal Orientation. . . . 81
3.16 Pole Figures of Sb_2Te_3 Films with Normal and Abnormal Crystal Orientations. 83
3.17 SQUID-VSM $M(H)$ and $M(T)$ measurements of a 6% Cr-Doped Sb_2Te_3 Film. 84
3.18 XAS and XMCD Spectra for a 6% Cr-Doped Film Compared to Simulated Spectra. 86
3.19 XAS and XMCD Spectra for a 6% Cr-Doped Film Along with their Integrals. 87

4.1 Diagram of Lattice Structure and A-type Antiferromagnetism in $MnBi_2Te_4$. 90
4.2 XRD plots Showing the In-Plane and Rotational Symmetries of $MnBi_2Te_4$ Thin Films. 94
4.3 Asymmetric RSM for a Pair of $MnBi_2Te_4$ Thin Films of Differing Stoichiometries. 96
4.4 Comparison of AFM Images of $MnBi_2Te_4$ Films with Excess and Compositionally Correct Mn Content. 97
4.5 $M(H)$ and $M(T)$ SQUID Measurements for $MnBi_2Te_4$ Thin Films. . . . 98
4.6 In-plane $M(H)$ SQUID Measurements for $MnBi_2Te_4$ Thin Films. 100
4.7 XAS and XMCD Spectra for 2 $MnBi_2Te_4$ Thin Films. 102
4.8 Sum Rules Analysis for XMCD Measurement of $MnBi_2Te_4$. 103
4.9 Hysteresis Loop of and $MnBi_2Te_4$ Thin Film Measured Using XMCD on the L_3 Edge. 104

5.1 XRD Studies on the Effect of Different Thickness Al Spacer Layers on Bi_2Te_3-$Ni_{20}Fe_{80}$ Bilayers. 113
5.2 Hysteresis Loops for NiFe Layers 114
5.3 Images of Cross-Pattern Hall Effect Devices. 115
5.4 Diagram of Measurement Geometry for Anomalous and Planar Hall Effect. 118
5.5 Results of Anomalous and Planar Hall Effect Measurements. 120
5.6 Graphs of Fitting Parameters Plotted Against Input Current for Planar Hall Effect Measurements. 122
5.7 VSM $M(H)$ loop of a Bi_2Te_3-$Ni_{20}Fe_{80}$ Bilayer. 123

List of Tables

2.1 Grain Size as Measured against Substrate Temperature. 43

3.1 EDS Studies of a Series of Mn-doped Bi_2Te_3 Thin Films. 55

3.2 EDS Studies of a Series of Cr-doped Sb_2Te_3 Thin Films. 74

4.1 Sputter Powers and Elemental Composition of a Series of ∼12 nm-thick $MnBi_2Te_4$ films (with the exception of sample 593, which is ∼16 nm). . . 93

5.1 Fitting Parameters Extracted from Planar Hall Effect Data at Multiple Currents. 121

5.2 Device Dimensions, Material Constants and Values Extracted from AHE and PHE Measurements. 121

Chapter 1

Introduction and Theory

1.1 Introduction

Topological insulators (TIs) are a novel state of matter, with physical properties underpinned by topological band theory [1–4]. The theory for TIs is an expansion of Haldane's work that laid down a framework for a quantum Hall effect that exists without a net magnetic field through the breaking of time reversal symmetry [5]. Topological insulators are bulk insulators with topologically protected metallic surface states that provide spin-polarised carrier transport. These surface states give TIs the potential to demonstrate a wide range of emergent physics, with the prototypical TI Bi_2Te_3, permitting the observation of phenomena such as the quantum spin Hall effect [1, 4], quantum anomalous hall effect [6, 7], and Majorana Fermions [8, 9], among others. These effects are not just interesting as explorations in quantum physics, but also show promise for application in the developing field of spintronics [10–13].

Attempts have been made to realise the functional applications of TIs by doping with transition metals and rare earth elements [14–34]. This has been done to break time reversal symmetry and open up a bandgap in the topologically protected surface state, opening up possibilities for spintronic applications in memory and logic devices.

However, realising the potential of topological insulators has proven difficult. Intrinsic defects inherent to even very high-quality films result in relatively high conductance for an insulator, suppressing the surface states' contribution to total conduction [25]. As such, a reduction of bulk material, without hybridising the surface states, which sit a few nanometres below the surface, could solve this issue. This has been attempted using nanoribbons [35], but difficulties with the growth mechanism mean this does not offer practical advantages over traditional thin films [36]. However, nanocrystalline clusters offer an approach that combines the reduced bulk of nanoribbons with the practicality of thin films [37]. Careful selection of the growth method and conditions allows for tunable grain sizes and the reduction of the bulk material contained within each cluster, thereby enhancing the effects resulting from surface states relative to 'higher quality' films.

1.2 Theoretical Discussion

Before results are discussed, this section provides a qualitative overview of the theory of TIs, allowing for a basic understanding of key concepts while highlighting the essential literature required for a full derivation. To achieve this, a discussion of the various Hall effects will be built into a model to understand 2D topological insulators. This will then be expanded into 3D topological insulators, which form the entirety of this thesis.

1.2.1 Hall and Quantum Hall Effects

The Hall effect occurs when carriers travel within an applied magnetic field, when at least a component of their velocity is orthogonal to the field. For the simplest case, we will consider an electron's motion through a plate conductor perpendicular to an applied field, in which case the Lorentz force will act as described in equation 1.1.

$$\vec{F} = -e\vec{F} \times \vec{B} \tag{1.1}$$

This results in the electrons travelling a curved path across the plate, resulting in an electric field (E_{H}) defined as:

$$\overrightarrow{E_{\mathrm{H}}} = R_H \vec{B} \times \vec{j} \tag{1.2}$$

Where R_{H} is the hall resistance and $\vec{j}$ is the current density.

The result of this is that a measurable potential is produced through the interaction of the field and charge carriers, allowing the measurement of a resistance perpendicular to the initial current, which holds the relation $R_{\mathrm{H}} = -1/ne$, where e is the elementary charge and n is the carrier density.

While this case is trivial, additional complexities arise in different materials at low temperatures and/or high fields, which necessitate the application of quantum mechanics to explain them. The most well-known of these is the Quantum Hall Effect (QHE), first observed by von Klitzing [38, 39], which can be observed in semiconductors in a high magnetic field. If we consider a two-dimensional electron gas (2DEG) as a sea of free electrons in two dimensions, but confined by an 'infinite' potential in the third dimension. Such 2DEGs are formed when electrons are confined at the interface of a p-n junction (such as AlGaAs/GaAs) due to the formation of a depletion layer at these interfaces. Under high magnetic fields and low temperatures, the electronic states will be restricted to discrete Landau levels described by the Hamiltonian:

$$\hat{H} = \frac{\hat{p_x^2}}{2m} + \frac{1}{2} m\omega_c^2 \left(\hat{x} - \frac{\hbar k_y}{m\omega_c} \right)^2 . \tag{1.3}$$

Where $\hat{H}$ is the Hamiltonian operator, $\hat{p_x^2}$ is the momentum operator in x, m is mass, $\omega_c = eB/m$ is the cyclotron frequency, $\hat{x}$ is the x position operator and k_y is the y momentum [39]. The x,y, and z axes are defined in Fig 1.1. It can be seen that this

Hamiltonian follows the form of a harmonic oscillator, with eigenvalues equal to:

$$E_n = \hbar\omega_c \left(n + \frac{1}{2}\right). \tag{1.4}$$

This quantisation of electron energies results in both the quantisation of the transverse resistivity and the elimination of the longitudinal resistivity. As the magnetic field increases, the Landau levels' energy increases, increasing the occupation of lower energy levels as fewer levels remain below the chemical potential. As such, a quantised change in resistivity will occur when an exact integer of Landau levels are filled, occurring at $B_i = \frac{n_e h}{ie}$ where n_e is the electron density and i is an integer [39].

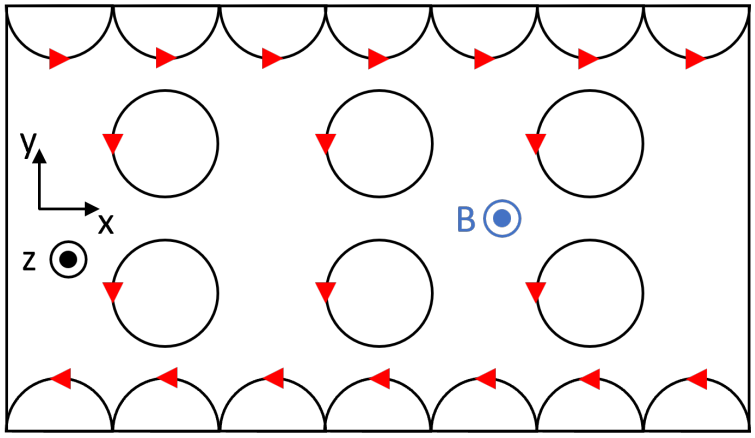


Figure 1.1: Simple model of electron paths in the QHE. It can be seen that while most electrons are confined in the bulk to complete cyclotron orbits, some are confined to partial loops in edge states.

An important consideration that this discussion has not yet included is that of edge states, which can be considered semi-classically via the Lorentz force. Therefore, in the presence of a strong magnetic field, most electrons will be confined to cyclotron orbits in the middle of the material, resulting in them not contributing to conductivity. However, some electrons will encounter the edge of the material in their orbits, resulting in them

'skimming' the edge of the material in one dimension. This effect is illustrated in Fig. 1.1 and is an example of the bulk band structure leading to a defined edge/surface state.

This approach is flawed, however, as it is limited to the modelling of single electrons. For a more complete discussion, the bending of the Landau levels at the edge of the sample, driven by the addition of the confinement potential of the 2DEG into the Hamiltonian, must be considered. This results in the Landau levels acting as a confining potential for the edge electrons, leading to the definition of the edge states.

1.2.2 Spin and Anomalous Hall Effect

While the effects that have been discussed so far rely on the presence of an external magnetic field, the first of which we discuss is the spin Hall effect (SHE). This effect demonstrates it is possible to generate Hall effects without the application of a field, with the spin-orbit interaction instead driving the process.

Consider a slab of material with high spin-orbit coupling (SOC) with the same geometry as the previous sections. If a current is passed through the film, electrons can be skew-scattered, leading to a transverse spin imbalance building within the slab. As spin accumulates on the edges of the slab, it can be asserted that it will circulate, just as charge circulates in the edge states of the regular Hall effect. This causes the generation of a spin current, i.e. the transport of spin without the aid of a magnetic field, which is an essential process in the emerging field of spintronics [40–43].

The other Hall effect that can occur without the presence of an external magnetic field is the anomalous Hall effect (AHE). This is a much simpler effect to explain, still being driven by spin-orbit coupling, but with an external magnetic field being replaced by internal magnetisation via ferromagnetic order. This effect can be detected alongside the Hall effect in ferromagnetic materials, often at a higher magnitude. This analogy provides

a simplified framework for understanding the origins of the effect, with a more detailed discussion of the spin-orbit interaction, as well as intrinsic (Berry-phase curvature) and extrinsic (skew and side-jump scattering off impurities) processes, available in Ref. [44].

1.2.3 Quantum Spin Hall Effect

The quantum spin Hall effect (QSHE) is foundational for the understanding of topological insulators and can be understood most simply as a combination of elements of the QHE and SHE, as the name may suggest. First proposed by C. L. Kane and E. J. Mele [1, 2], the effect combines the edge states in the QHE, which allow the presence of separate $+k_x$ and $-k_x$ conducting channels, with the spin-orbit coupling-driven spin transport of the SHE. This leads to a splitting of the channels at each edge by both spin and momentum, and since no magnetic field needs to be applied, the system now conserves time-reversal symmetry (TRS). This is illustrated in Fig. 1.2(b), where it can be seen that electrons on the same edge of the material but of opposite spin cannot travel in the same direction. Both the QHE (Fig. 1.2(a)) and QSHE (Fig. 1.2(b)) shown in this figure display how the edge states suppress scattering. In the QHE, the spatial separation of momentum channels prevents scattering, but only in the 1D case.

However, the QSHE prohibits backscattering off non-magnetic impurities at a more fundamental level owing to interference effects. Fig. 1.2(c,d) illustrates the two possible scattering paths around an impurity with one showing a spin rotation of π and the other of $-\pi$. As TRS is preserved, each scattering path is equally likely, and as the total path difference between them is 2π, they will destructively interfere as spin-1/2 wavefunctions flip sign under a 2π rotation. This means that the edge states in the QSHE effect allow for dissipationless transport of electrons, and the breaking of TRS, the introduction of magnetic impurities, or applied fields can be used to control the scattering process in

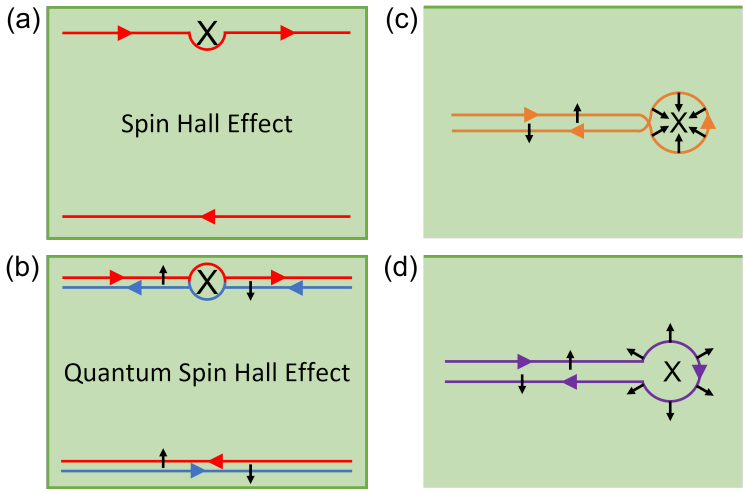


Figure 1.2: (a) Illustrates the SHE with spin-polarised edge states. Note how these channels are protected from scattering off a non-magnetic impurity. (b) Basic model of the edge states in the QSHE, with spin up and down channels counter-propagating along the edge. Note the momentum inversion of the states on the bottom versus the top. (c,d) Display how spin-momenta locked channels are protected from scattering off non-magnetic impurities, with the two possible, but equally likely, path lengths destructively interfering and suppressing scattering. Figure adapted from Ref. [45].

such systems. Experimentally, this effect was first observed in CdTe-HgTe quantum wells in Ref. [46, 47].

While it is easier to visualise the surface states in 2D, the materials used in this project are 3D materials, and to understand this effect in 3D, a consideration of band theory is required. In the following Subsection 1.2.4, a discussion of band inversion and the $\mathbb{Z}_2$ topological invariant.

1.2.4 3D Topological Insulators

Topological insulators are characterised as bulk insulators with spin-momentum-locked metallic surface states. This, for the materials used in this thesis (Bi_2Te_3 and Sb_2Te_3),

is in itself a misnomer, as they are not true insulators, but instead semiconductors. As discussed in Section 1.1, this makes studying the surface states difficult, hence the efforts to reduce the amount of bulk material using nanocrystalline films in this thesis.

The explanation presented in this section follows the summary given in Ref. [48]. Firstly, we should consider a 'normal' direct band gap semiconductor with valence and conduction bands (VB and CB, respectively), with the Fermi level situated between the bands. Here, we can assume that the valence band is full and the conduction band is empty. Additionally, for most normal semiconductors, the VB has a positive parity (s character) and the CB has negative parity (p character). Now we consider a second semiconductor with inverted band parity, and a junction between these two materials. At this junction, the flip of parity necessitates that the bands cross the Fermi energy, resulting in metallic surface states. These band structures are illustrated in Fig. 1.3.

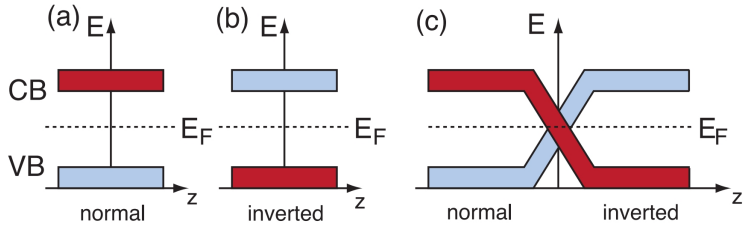


Figure 1.3: Basic model of bands at the interface between materials with inverted and normal band structure. (a) Positive (red) and negative (blue) parity bands in a 'normal' semiconductor. (b) Inverted parity semiconductor with negative conduction band and positive valence band, driven by the band splitting due to strong spin-orbit coupling. (c) Upon joining the materials shown in (a) and (b), the parity must invert at the interface. This results in the bands crossing the Fermi level and results in a metallic state at the surface. Figure taken from Ref. [48].

It is important to realise that while these states exist on or near the surface, they are not in fact due to any property of the surface and are instead a consequence of bulk

properties. A common analogy to understand this is a hypothetical border crossing between a nation with roads where vehicles travel on the right and another where they travel on the left. At this boundary, a 'flipper bridge' is required to invert the flow of traffic. This provides a real-world example where a 'bulk property', i.e. the handedness of the roads in a country, leads to unique circumstances on the edge of the system. It should also be noted that more complex bridges are permitted solutions to this problem, provided that they have an odd number of inversions across their span. This becomes significant as we begin the discussion of the $\mathbb{Z}_2$ topological invariant in the coming pages.

A strong spin-orbit interaction drives this sort of band inversion in TIs. If we consider the direct band gap semiconductor discussed above, where the VB is of p character and the CB of s character. In a material with this band structure and strong spin-orbit coupling, the degeneracy of the p level is lifted, with the creation of $j = 3/2$ and $j = 1/2$ states. If the SOC is strong enough, then the $j = 3/2$ state can shift above the s band, resulting in the parity inversion required for TI edge states. A simplified illustration of this band splitting and inversion is shown in Fig. 1.4.

This simple model provides a straightforward explanation of the stability of topologically protected surface states, but it neglects essential details, such as the role of time-reversal symmetry. It also fails to explain the existence of surface states between TIs and a vacuum, instead only focusing on the interface between two materials. The following text will aim to provide an explanation that resolves the shortcomings of this model, now that an intuitive understanding has been established.

To approach this issue through a more direct consideration of electronic structure, we first model a free-electron surface state of parabolic dispersion, centred at the Γ of the surface Brillouin zone (SBZ), such as those found on (111) surfaces of noble metals

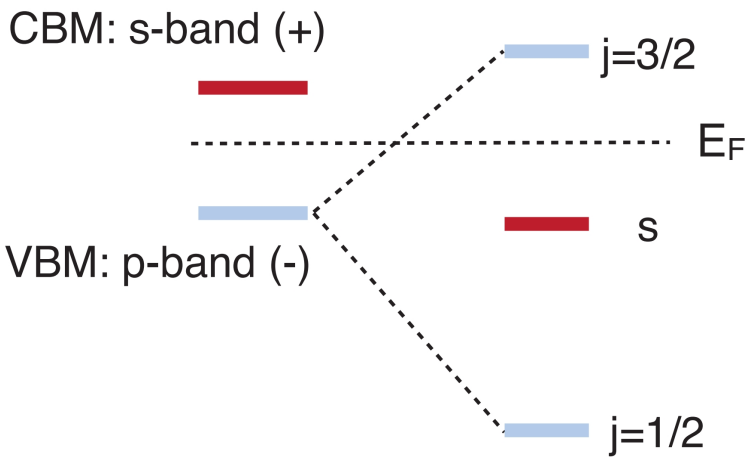


Figure 1.4: Representation of band splitting due to strong spin-orbit coupling This coupling lifts the spin-degeneracy of the p-band, pushing the $j = 3/2$ state over the conduction s-band and a parity inversion. Figure taken from Ref. [48].

[49]. These states can only exist in projected gaps of the surface band structure, and their dispersion is shown in Fig. 1.5(a).

Introducing a strong spin-orbit interaction to this system lifts spin degeneracy and is illustrated in Fig. 1.5(b). This can be described mathematically by the Rashba model [50, 51]. This model is designed to explain 2DEGs in the presence of perpendicular electric fields to the plane of the electron gas, in which the electron's energy is dependent on its spin. This is due to it experiencing the electric field as a Lorentz-transformed magnetic field. This can be assessed analytically via adding a spin-orbit term to the Schrödinger equation for a free electron in two dimensions:

$$\hat{H}_{SO} = -\frac{\hbar}{4m_e c^2}(\hat{p} \times \hat{E})\hat{\sigma} = \alpha(\hat{n} \times \hat{p})\hat{\sigma}. \tag{1.5}$$

where $\hat{p}$ is the momentum operator, $\hat{E}$ is the electric field, $\hat{\sigma}$ is the Pauli spin operator, and $\hat{n}$ is a unit vector normal to the surface [48]. Combining this with the Hamiltonian

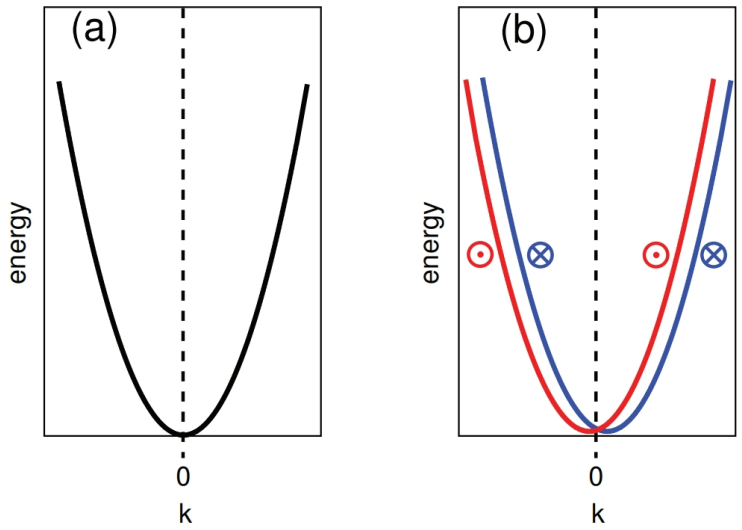


Figure 1.5: (a) 1D cut of the 2D dispersion relation of a metallic surface state without spin-orbit coupling. (b) The same dispersion with the strong spin-orbit coupling, lifting spin-degeneracy, and shifting the dispersion via the Rashba effect. Figure adapted from Ref. [48].

of the free electron and solving analytically, you get the following energies:

$$E = \frac{\hbar^2 k^2}{2m_e} \pm \alpha \hbar k. \tag{1.6}$$

where the $\pm$ sign represents different spin directions [48]. The Equ. 1.6 shows that the system is always degenerate at Γ, a consequence of TRS known as Kramers degeneracy. Kramers' degeneracy states for every state with an odd number of spin 1/2 particles, the system remains at least double degenerate in the absence of a magnetic field [52, 53]. This is because for every state with wave and spin vector ($\vec{k}$, $\uparrow$), TRS guarantees an equivalent solution (-$\vec{k}$, $\downarrow$). Thus, for $\vec{k} = (0, 0)$ the states must be spin degenerate.

This can be related to TIs by considering spin-split surface states in a hexagonal lattice. Combining TRS with crystal symmetry enables the observation of more degeneracies. A hexagonal SBZ with a surface state at ($\vec{k} = \bar{M}$, $\uparrow$) will have a degenerate state at (-$\vec{k}$,

$\downarrow$), but due to lattice symmetry, this point is also a $\bar{M}$ point. Therefore, there must be two degenerate states for both spins at every $\bar{M}$ point in the lattice. Points such as these are known as surface time-reversal invariant momenta (TRIM), which exist at several points of the SBZ.

The most significant parameter to determine whether an insulator is topologically trivial or non-trivial is the number of Fermi level crossings between two surface TRIM points. An odd number of crossings is non-trivial, as no smooth deformation of the band structure can eliminate the crossing point; conversely, the opposite is true for an even number of crossings. This information is contained within the $\mathbb{Z}_2$ topological invariant, which can be calculated via the bulk band structure, as shown in Equ. 1.7.

$$(-1)^{\nu_0} = \prod_{i=0}^{n} \delta(\Gamma_i) \tag{1.7}$$

where n is the number of bulk TRIM points, and $\delta(\Gamma_i)$ is the parity invariant for each relevant TRIM (i.e. Γ) [48]. This is defined as $\delta(\Gamma_i) = \prod_n \xi(\Gamma_i)$, where $\xi_{2n}(\Gamma_i) = \pm 1$ are the parity eigenvalues for the n occupied band at the TRIM[48]. In general, $\nu_0 = -1$ for non-trivial insulators and $\nu_0 = 1$ for trivial cases [48]. It should be noted that the prototypical TI Bi_2Te_3 has an $n = 8$ and a topological invariant of one for all TRIM points, except for Γ, where it is equal to -1, resulting in a total product of -1, which permits the TI state to exist. In 3D, this band structure takes the form of a single Dirac cone at the Γ point [54].

1.2.5 Time Reversal Symmetry and Quantum Anomalous Hall Effects

Time reversal symmetry is an essential component of TIs, playing a vital role in the protection of the surface states. The breaking of time reversal symmetry via the introduction of ferromagnetic order removes the protection against backscattering common

to TIs and the QSHE, as magnetic impurities in the lattice mean the two possible scattering paths are no longer equally likely. Additionally, magnetic order can result in a band gap opening in the otherwise gapless edge states [55–57]. This leads to the transition from a massless Dirac fermion, a particle with dispersion defined by the Dirac cone and an effective mass linked to the band gap, to a massive Dirac fermion [54]. This opening of the band gap allows for the observation of interesting phenomena, most notably the quantum anomalous Hall effect (QAHE).

The quantum anomalous Hall effect has been observed in magnetic topological insulators [7] and was predicted in both 2D magnetic insulators and 3D TIs [25]. This effect can be considered as a combination of the QHE and AHE, displaying quantised conductance without the presence of an external magnetic field. Such an effect has potential applications in spintronic devices, with the quantised conductance levels allowing for the encoding of information across a QAHE device.

The potential of this effect for use in logical devices is what drives the research in this thesis, with the QAHE effect having been observed in Cr-doped $(Bi_xSb_y)_2Te_3$ thin films [7]. However, this effect is small and often overshadowed by other Hall effects, and it is only observed at very low temperatures. As such, a focus on enhancing these effects, alongside increasing the magnetic transition temperature of magnetic TI (MTI) films, is essential for making devices more scalable. This is where the reduced bulk material and suppression of bulk conductivity of nanocrystalline films discussed in Section 1.1 provide a possible solution for this issue.

1.3 Outline of Thesis

This thesis focuses primarily on the introduction of magnetic order into nanocrystalline TI thin films. To achieve this, a range of structural, magnetic and electronic

characterisation techniques will be used on films of various chalcogenide materials. This allows the determination of optimal growth conditions as well as the limitations of each material. Each chapter is built around a single material/multilayer, with the bulk of the work displayed forming the basis for either peer-reviewed published work or publications currently under review.

Chapter 2 explores experimental methods, covering both the underlying physics and the practical aspects of the techniques used. Growth of undoped TIs is covered in this section, as this provides the foundation for all subsequent chapters. Chapter 3 investigates Mn-doping of Bi_2Te_3 and Cr-doping of Sb_2Te_3. Chapter 4 discusses the growth and characterisation of the intrinsic magnetic topological insulator $MnBi_2Te_4$. Chapter 5 covers the patterning and measurement of Bi_2Te_3-$Ni_{20}Fe_{80}$ bilayers for spin-orbit devices. Finally, Chapter 6 summarises the main findings of the work and looks to the future advances that can be made in the field.

Chapter 2

Methodology

2.1 Magnetron Sputtering

2.1.1 DC Magnetron Sputtering

Magnetron sputtering is a physical vapour deposition technique commonly used in industry due to its fast deposition rate and high scalability. Sputtering is not as optimal as molecular beam epitaxy (MBE) for producing ultra-pure, low-defect films, owing to the high-energy nature of the deposition. However, this technique can be exploited to achieve the ideal method for tuning nanocrystalline grain sizes and suppressing the bulk contribution to conductivity.

DC magnetron sputtering works by generating a plasma from an inert gas, in this case Ar, in a vacuum chamber. The plasma is produced by passing a DC potential between an anode and a cathode, which, in the case of a magnetron sputter system, is typically a cylindrical grounded shield and a circular target held at potential. This combined system, consisting of a cathode, anode, target, and magnet, is referred to as a 'sputter gun'. Underneath this target is a toroidal magnet that confines the plasma into a similar shape above the target. The ions in this plasma will then collide with the surface of the target, ejecting atoms towards the substrate. A schematic of a typical DC

magnetron sputter system is shown in Fig. 2.1 [58].

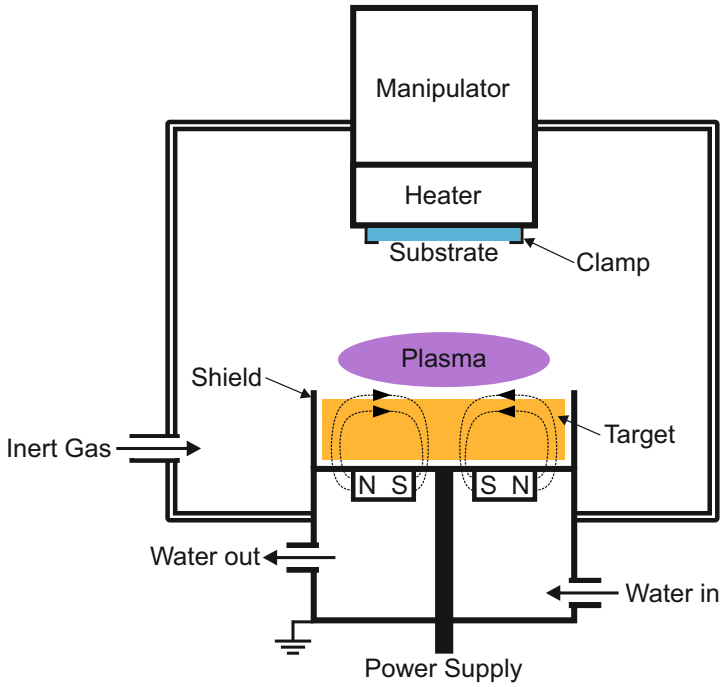


Figure 2.1: Diagram of a generalised sputter system, showing the sputter target held at a potential mounted within the grounded shield. The toroidal magnet used to confine the plasma above the target is also illustrated. The water flow through the sputter gun exists to cool the electronics to prevent damage during extended operation. At the top of the diagram, the manipulator, heating element, and substrate, held in place with clamps, are all displayed.

A sputter system requires the use of turbomolecular and/or ion pumps to achieve the lowest possible vacuum. This is to prevent both target oxidation and limit impurities within the chamber, thereby reducing defect density and preserving the film's crystallinity. The sputter chamber used for the research was the chalcogenide sputter system located at the Clarendon Laboratory, University of Oxford. This system consisted of two chambers (later expanded to three), a load lock for loading/unloading into the system and a growth

chamber, as illustrated in Fig. 2.2.

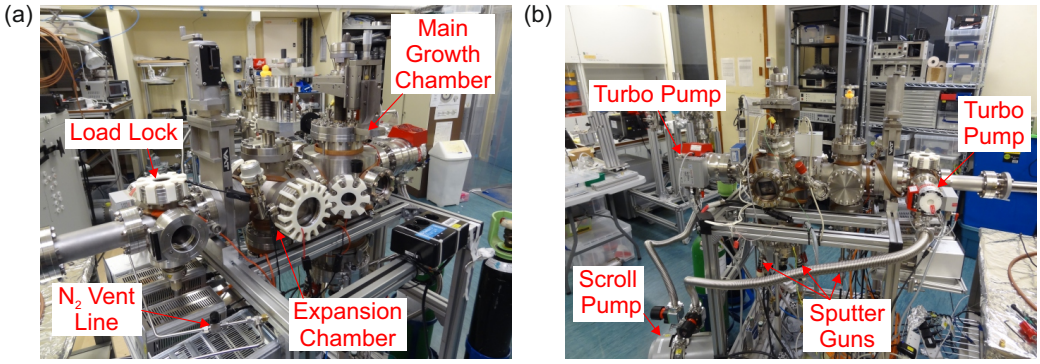


Figure 2.2: Images of the M3 sputter system in the Clarendon Laboratory (a) Shows the three different chambers and the N_2 venting line used to bring the load lock to atmospheric pressure. (b) Photograph from the other side of the sputter system, where the sputter guns and pumps are more visible.

The load lock was pumped from atmosphere via a Varian SH-110 scroll pump backing a Pfeiffer Vacuum HiPace80 turbomolecular pump. This backing pump was shared with the main chamber, with valves attached between each turbomolecular pump and the scroll pump, allowing the chambers to be isolated from one another if they were at significantly different pressures, shown in Fig. 2.2. This was done to prevent issues with back pressure passing through the turbomolecular pumps via their exhaust lines, which fed into the scroll pump for backing, as this could cause venting of the chamber and damage to the pumps.

This configuration allowed the main chamber to reach pressures of $\sim 2\times10^{-8}$ Torr using a Pfeiffer Vacuum HiPace300 turbomolecular pump. The growth chamber had two configurations during the project, starting as a three sputter gun chamber using MeiVac 2" sputter guns with a single manipulator used to mount the sample holder, shown in Fig. 2.3. The manipulator also mounted the heating element required for growth

at the elevated substrate temperatures necessary to produce nanocrystalline films. A Prevac HEAT2-PS heating power supply provided current for the heater, and the guns were powered by two ENI RPG-50 DC plasma generators. The growth chamber was later expanded with an additional 6-way cross, which allowed the installation of a 4^{th} sputter gun; this required the installation of a second manipulator, which was machined as a bespoke part out of Al. This manipulator did not have the same heater as the primary manipulator; however, this was not needed, as this gun was only used for the deposition of capping and spacer layers, freeing up space among the other guns for more complex projects. To maintain simplicity, the expansion was not separated from the growth chamber with a gate valve, leaving both sections pumped by the turbomolecular pump for the main chamber. This resulted in a base pressure of between $\sim 7\times10^{-9}$ and 2×10^{-8} Torr, with the variance due to the particular sputter targets loaded at any time. It should be noted that there was no noticeable difference in the quality of the films produced in this range of base pressures.

Before growth can be undertaken in the chamber, it must first be loaded with 2" sputter targets. Depending on the storage and air sensitivity of the targets, they may be sanded and cleaned to reduce any oxide/impurity build-up on the surface. Alongside this, the shutters that cover the guns when not in use are also treated similarly to ensure there is no contamination, as a build-up of material on the inside of the shutter will naturally happen through regular operation of the chamber. This also prevents flakes of material from falling into the guns and causing shorts between the anode and cathode, which need time consuming repairs that require exposing the chamber to atmosphere, delaying project timelines.

Once these tasks are complete for each gun, the chamber can be closed and pumped

down to base pressure over the course of several days. During this period, an inert gas will be introduced into the chamber, and each gun ignited for several minutes with the shutter closed to 'precondition' the target, sputtering off any oxide or impurities on the target surface. While the chamber reaches base pressure, a blank sample holder is placed in the manipulator to ensure no material deposits on the heater or thermocouple during this process. Additionally, the sputtering of oxygen-reactive materials can also aid in chamber pressure by absorbing and trapping oxygen and other impurities where this material settles, such as the shutters or the chamber walls. Once this process is complete and base pressure is reached, a substrate is prepared and mounted on the holder, shown in Fig. 2.3.

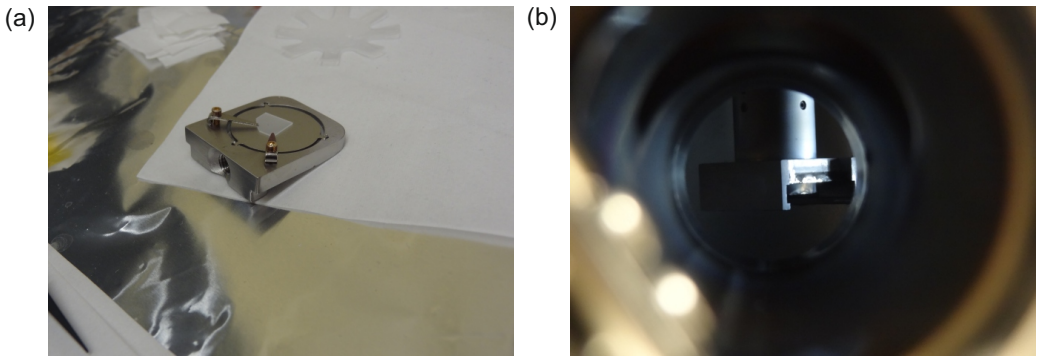


Figure 2.3: (a) Photograph of the sample with a Sapphire substrate mounted via two clips tightened by screws. (b) Photograph of the manipulator in the main growth chamber of the sputter system.

The holder is then mounted onto the transfer arm within the load lock, which is then pumped and transferred to the main chamber. The substrate can then be heated to the required temperature, and a growth performed. The primary growth parameters for tuning the growth mode and film properties were: the growth pressure, adjusted using an MKS Instruments Type 647B gas flow controller; the power applied to the sputter

gun; the substrate temperature; and the growth time.

2.1.2 RF Magnetron Sputtering

While DC sputtering was the primary method used during the research, it is not always the optimum choice for sputtering. This has two possible causes. Firstly, the build-up of positive charge on the surface of the target, repelling the Ar ions in the plasma and reducing sputter yield, or leading to a reduction in voltage to below what is needed for a stable plasma [58]. In this case, the RF allows for these charges to neutralise, enabling continuous plasma discharge. Secondly, if the target is an insulating material, an RF voltage will couple capacitively to the target and the plasma [59]. The introduction of an RF power source means the introduction of an impedance matching network is required for effective RF transmission to the gun. During the work described in this thesis, it was found that Si and Te both required the RF source to maintain a stable plasma, owing to the high resistance of these targets. This was achieved using RF power, supplied to the gun via a Cesar RF power supply, which was fed into a Kurt J. Leskar AT3 matching network connected to an MC2 automatic matching network controller, providing for low-loss transmission of RF power to the sputter gun.

2.2 Structural Characterization Techniques

2.2.1 X-ray Diffraction

X-ray diffraction (XRD) is a commonly used technique in crystallography that uses a monochromatic X-ray beam incident on the sample surface. The crystal lattice serves as a diffraction grating, with X-rays diffracting off atomic planes and constructively interfering at certain incidence angles. The Bragg equation dictates these angles, dependent on the wavelength λ of X-rays incident on a crystalline material with interplanar separation

d, at an angle between the incident and diffracted beam θ, and n being the order of diffraction. This equation is shown in Equ. 2.1.

$$n\lambda = 2d\sin(\theta) \tag{2.1}$$

Measuring these diffraction peaks and comparing them to crystal structures in existing literature and analysis of the peaks allows for the calculation of lattice parameters. The chalcogenide TIs used in the research have the rhombohedral symmetry group $R\bar{3}m$. The interplanar separation d in Equation 2.1 is related to the lattice parameters $|a| = |b|$ and c for this symmetry group through the equation:

$$\frac{1}{d^2} = \frac{4}{3}\left(\frac{h^2 + hk + k^2}{a^2}\right) + \frac{l^2}{c^2} \tag{2.2}$$

Where h, k, and l are the Miller indices of the specific diffraction peak.

During the course of the research, several different measurement geometries were used, all of which were performed in the Clarendon Laboratory on a Rigaku SmartLab at a wavelength of 1.5405980 Å. All of these geometries were based on parallel beam optics, shown in Fig. 2.4(a). These different geometries involved scans across multiple rotational planes, with all the angles used shown in Fig. 2.4(b). The first geometry was out-of-plane XRD, which allowed the identification of peaks in the $(00l)$ plane.

The particular setup utilised a stationary sample with a moving source and detector. In this geometry, $2\theta - \omega$ scans are used to identify diffraction planes parallel to the sample surface, i.e. $(00l)$ peaks. Measuring peaks this way leads to Equation 2.2 simplifying into:

$$\frac{1}{d^2} = \frac{l^2}{c^2} \tag{2.3}$$

Combining Equations 2.1 and 2.3 allows the c-axis parameter to be calculated thusly:

$$c = \frac{n\lambda}{s\sin\theta}l \tag{2.4}$$

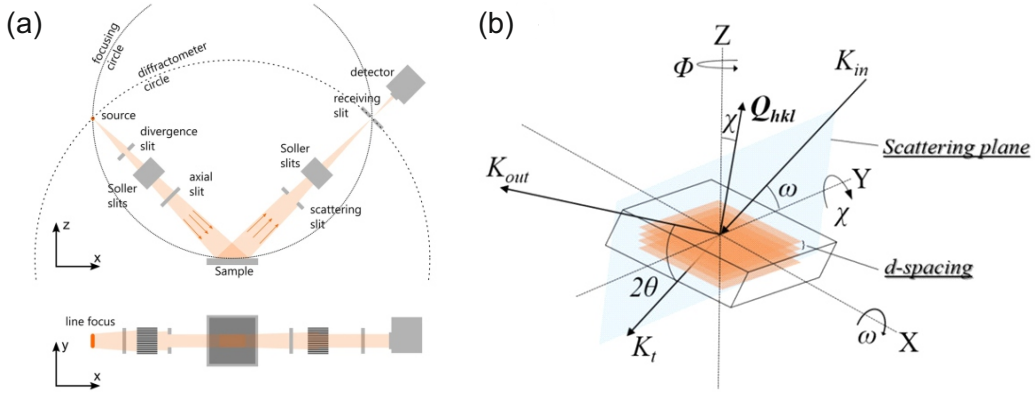


Figure 2.4: (a) Diagram of an XRD system using parallel beam optics. Figure taken from Ref. [60]. (b) Diagram illustrating the different axes and rotational degrees of freedom of a thin film XRD system. Figure taken from Ref. [61].

Owing to the broad nature of the peaks due to the nanocrystallinity of the films, fitting the XRD yielded unreliable results. However, due to the high angular resolution of the measurements, calculating lattice parameters from the local maxima in the raw data yielded errors of less than 0.1 Å.

Out-of-plane XRD was conducted using the following optics to best confine the beam, balancing count rate with effects due to a larger beam profile, such as peak broadening. The optics between the source and the sample typically consisted of a 2.5 ° Soller slit, a 5 mm horizontal slit and a 1 mm vertical slit. Between the sample and the detector, the beam was passed through a K-β filter before reaching the detector 300 mm from the sample [62].

However, due to complications in growth, it sometimes became necessary to examine diffraction peaks outside the (00l) plane, requiring different measurement geometries. Firstly, grazing incidence XRD (GI-XRD) allows peaks growing canted to the plane to be observed. This is achieved using the same optics as out-of-plane XRD, but with the

incidence angle fixed at 4° and the detector angle 2θ swept.

Secondly, reciprocal space mapping (RSM) was employed to further investigate the diffraction peaks. Symmetric RSM was performed using the same optical set-up detailed above, except the K-β filter was removed to improve the counts reaching the detector, but with a sweep in ω and $2\theta/\omega$ around a specific diffraction peak, this enables the imaging of peaks in two dimensions in reciprocal space, providing a means of determining how differences in growth condition cause effects like peak broadening, often an indicator for grain size within a film.

Finally, asymmetric RSM was performed to explore off-axis peaks, as this may better highlight any secondary phases within the film. This technique employs a distinct optical setup from previous methods, utilising the 2D detector mounted on the SmartLab II. This required removing the optics in front of the source to allow the detector to operate in 2D mode; however, the optics between the source and the sample were left the same as the symmetric RSM. Multiple sweeps of 2θ were performed at fixed χ, with the 2D detector allowing the observation of peaks from all (hkl) diffraction planes.

2.2.2 X-Ray Reflectivity

X-ray reflectivity (XRR) is a technique that uses interference to allow the calculation of structural properties, including film thickness, roughness and interfacial boundaries. Snell's law governs the behaviour of light as it moves from one transparent medium to another.

$$n_1 \sin\theta_1 = n_2 \sin\theta_2 \tag{2.5}$$

Where n_1 and n_2 are the refractive indices of the two media, and θ_1 and θ_2 are the angles that a ray of light makes with the plane of the sample surface upon incidence and refraction, respectively. The refractive index of a medium is dependent on the frequency

of the incident light; in the case of X-rays, this value is slightly smaller than unity [63]. As a result, when an X-ray is incident on a sample surface, total internal reflection is possible below a critical angle, dependent on the density of the interface.

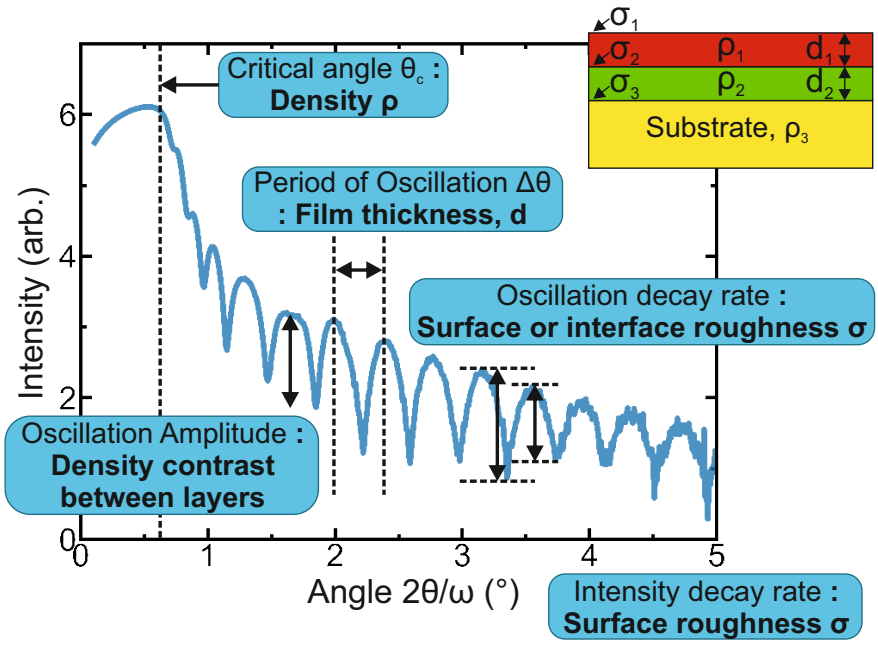


Figure 2.5: A typical XRR measurement, with the features of the reflectivity curve labelled by their associated material properties. Figure adapted from Ref. [64].

Beyond the critical angle, X-rays are reflected from a perfectly sharp and flat interface as governed by the Fresnel equations. However, as the wavelength of the X-rays used are in the order of 1-2 Å and interfaces are rarely sharper than this length scale, deviations from the reflections predicted by the Fresnel equation can be modelled to determine structural information from these reflections. In addition to this, the Fresnel equations for a homogeneous layer of material of finite thickness with a smooth surface will show intensity oscillations as the source and detector are swept through the $\theta/2\theta$ axis known as Kiessig fringes. These arise as the result of interference between the reflections from

the top and bottom interface of the layer [63]. The period of these oscillations is inversely proportional to the film thickness z_{tot} via the following equation:

$$z_{tot} = \frac{2\pi}{\Delta q} \tag{2.6}$$

where q is the momentum transfer vector of the reflected X-rays. These effects combine to give a result with features typical of the diagram shown in Fig. 2.5.

XRR measurements were taken on the same Rigaku SmartLab as the XRD measurements detailed in the previous section, using an identical optical setup (without the K-β filter) for plane XRD.

2.2.3 Atomic Force Microscopy

Atomic Force Microscopy (AFM) is a technique that uses an ultra-sharp cantilever, which is designed to deflect due to interatomic forces between the tip and the sample. As this deflection is dependent on the proximity of the tip to the sample, it can be used to produce a profile of the surface as the tip is scanned laterally across the sample. This allows direct mapping of the sample surface and direct imaging of surface roughness, grain size and anisotropy. AFM measurements for this thesis were taken using a Veeco Instruments Multimode V AFM, shown in Fig. 2.6. Due to the soft nature of TIs, a product of the relatively low strength of Van der Waals forces between quintuple layers, tapping mode AFM was used. Tapping mode AFM uses a cantilever tip oscillaing in the 100s of kHz range above the sample surface, limiting contact between the tip and the film. This was chosen over contact mode as the soft film can be 'pushed' by the moving tip, leading to both damage to the film as well as a potential build-up of material attached to the tip, reducing resolution. However, as non-contact mode relies on very weak forces as the tip never touches the film, making precise measurements more difficult.

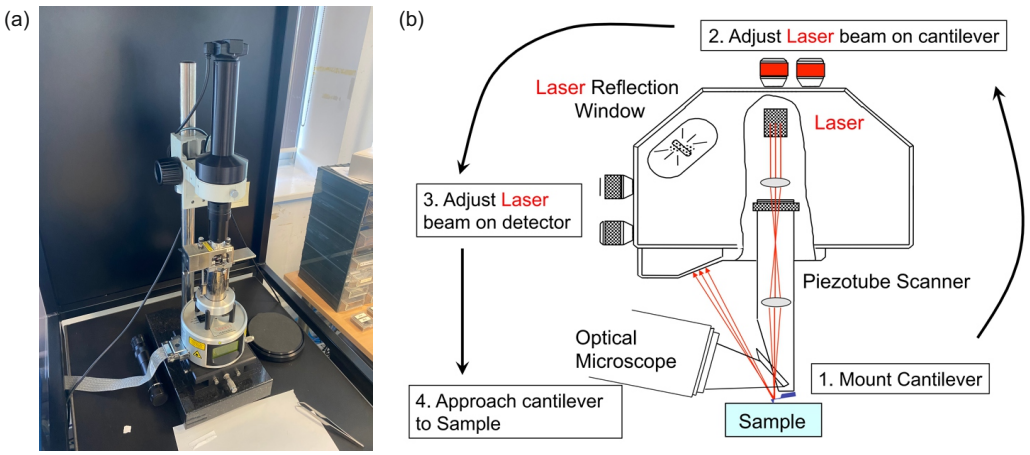


Figure 2.6: (a) Image of the Veeco Multimode V AFM used in this thesis. (b) Schematic of the AFM. Annotations detail how to align the laser on the back of the cantilever. The deflection of the cantilever will move the laser across the detector, allowing a signal to be detected. Figure taken from Veeco Instruments Inc.

Therefore, the intermittent contact and oscillatory motion of the cantilever in tapping mode limits the destruction of the film, as well as the vertical motion of the cantilever (often held at a resonance of around 300 kHz for tapping mode specific cantilevers), which can mechanically remove any material that may build up on the tip.

2.2.4 Scanning Electron Microscopy and Energy Dispersive X-ray Spectroscopy

While X-ray diffraction and reflectivity measurements combined with AFM provide a detailed picture of both the surface morphology and crystallographic phase, it is not possible to determine the exact stoichiometry of the film. During transition metal doping studies, it is crucial to determine the exact concentration of elements within a film. While a more detailed explanation of the growth methodology will be provided in the chapters specific to transition metal doping of TIs, this doping is achieved by sputtering a TI

target simultaneously with the transition metal, with the power used to generate the plasma tuned to control the relative deposition rates of the two sources. If this is done and growth rate, as a function of sputter power, has been determined by fitting XRR fringes of films grown at different powers, then a estimated concentration for the dopant can be calculated. This approach relies on a few assumptions, including:

1. The growth rate from each source is the same whether it is used in isolation or co-sputtered with another source.

2. The growth rate is constant with time.

3. The doping mechanism is purely substitutional.

While these assumptions likely do not hold exactly, they allow for estimation of the dopant concentration before growth and, therefore, allow a repeatable and systematic growth series to be planned. After growth actual sample stoichiometry was determined by energy-dispersive X-ray spectroscopy (EDS)[1] built into a scanning electron microscope. The EDS system used was an Oxford Instruments Xmax^n 80T attached to a JSM-6610LV scanning electron microscope (SEM), with the data processed and analysed using the Oxford Instruments EDS software, Aztec. This equipment was located at the Research Complex at Harwell.

SEM uses a focused beam of electrons accelerated to a fixed energy incident on the sample, and then detects the electrons scattered off the sample surface to form an image. These electrons either come from backscattering or secondary electrons produced due to inelastic collisions with the sample surface.

Owing to the shallow depth at which secondary electrons are produced in a sample, these were used in an attempt to image the sample's topography; however, this proved

[1]EDS and EDX are both conventionally used; this text will use EDS from this point forward

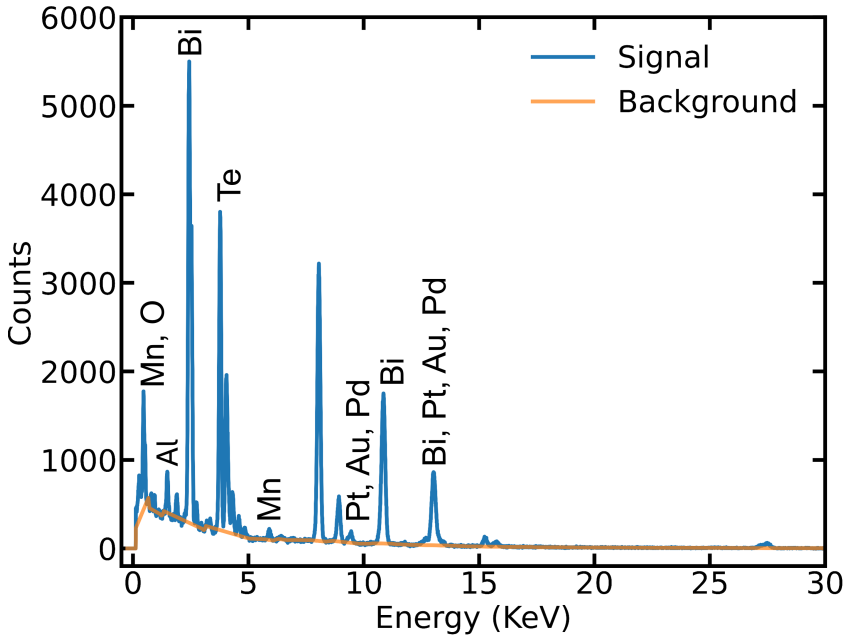


Figure 2.7: Plot showing a typical EDS spectrum for a TI, with the background shown alongside the signal. In this instance, the spectra were obtained in a TEM with an incident electron energy of 200 keV, whereas typical SEM spectra were measured at 20 keV. Element-specific peaks are visible, and analysis of their areas can provide insight into the relative abundances of different elements in the sample. Additional peaks from Pt, Au and Pd are visible due to the sample preparation performed for the TEM measurement, described in Subsection 2.2.5. It should be noted that the strongest peaks at low energy, caused by lighter elements, often overlap, making quantitative analysis difficult below 5 keV.

difficult owing to the small feature size of the nanocrystalline films. While the SEM used did not have the spatial resolution to image features on the film's surface, the electrons from the instrument can stimulate excitations of core-level electrons that will eject them from an otherwise full orbital. After this, an electron from an outer orbital will decay into the space left in the core orbital, resulting in a release of X-rays with an

energy characteristic of the electronic state of the atoms present. A typical spectrum observed during this project is shown in Fig. 2.7, which is automatically processed and analysed by the Aztec software to identify the elements present and determine the sample composition.

It should be noted that this method has an inherent limitation in its accuracy due to the film thickness. As the mean free path of electrons passing through the film is much greater than its thickness, only a fraction of the X-rays are produced by the film, with the rest coming from the substrate. This results in the signal being dominated by aluminium and oxygen, making lower energy peaks difficult to identify in this region. To resolve this, large numbers[2] of repeat scans were taken to provide large statistics for an accurate estimate. To increase measurement reliability, scans were taken at different magnifications in the SEM and at different locations on the sample. From this large dataset, an average was taken, increasing accuracy and allowing an approximate error to be determined.

2.2.5 Scanning Transmission Electron Microscopy

Scanning transmission electron microscopy (STEM) is an transmission microscopy technique, using a variety of detection methods with different imaging purposes. Cross-sectional STEM provides imaging of the film in profile, which, combined with the potentially sub-Angstrom resolution of STEM, allows for the imaging of the atomic structure of a sample. To achieve this, a small lamella of the larger film must be produced and placed onto a grid that allows the transmission of electrons. This is necessary because the sample and the substrate are too thick to allow electron transmission. The lamella is produced using focused ion beam (FIB) milling of the sample to cut out a piece of

[2]Around 20-60 repeat scans were taken per site on the sample.

the sample and lift it out of the film using a needle before placing it on the grid. A layer of C and Pt is deposited on the sample prior to FIB processing in order to protect the sample from damage due the beam and charging effects, as well as ensure that the sample is thick enough (in the axis perpendicular to the electron beam) to survive the lift-out process.

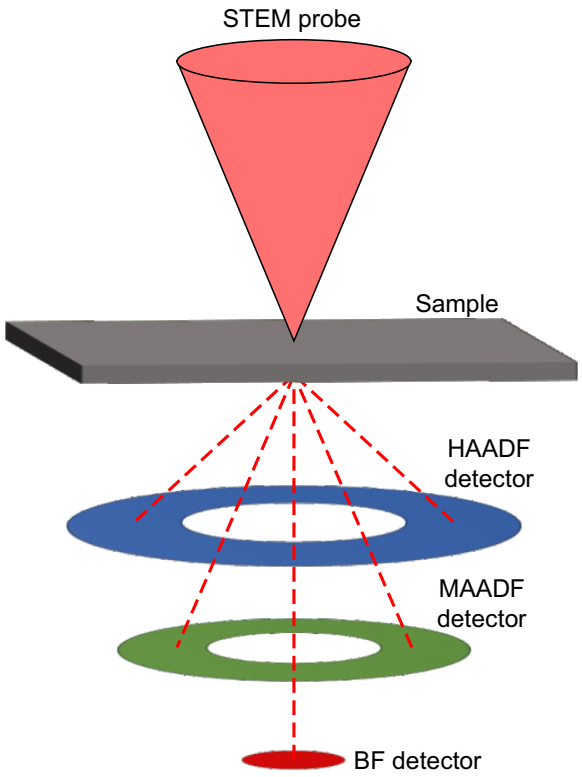


Figure 2.8: Diagram of the layout of annular and bright field detectors in a STEM.

Once the lamella is produced and placed on a grid, STEM can be performed. In this research, either bright field (BF) or high-angle annular dark field (HAADF) detectors were used to image the sample; the geometry of the detectors is shown in Fig. 2.8.

BF-STEM uses the unscattered beam, i.e. the beam that does not strongly interact with the lattice, leaving the areas where the beam passes through 'empty areas' in the sample bright and the atomic sites darker, providing high contrast images for films with lighter elements, as elements with a higher atomic number, Z, strongly scatter electrons. This is where HAADF-STEM becomes more applicable, as it detects only the electrons that have been scattered by the film, leading to a proportionality between Z and signal intensity. Elements such as Bi will have a strong signal, and combining this with the bright field image allows for a qualitative assessment of the sample's homogeneity. This proves particularly useful when assessing samples with substitutional dopants, as clustering of the dopant with Te leads to Bi-deficient areas in transition metal-doped Bi_2Te_3. These assessments can also be quantitatively analysed via two different methods, EDS, as detailed in Subsection 2.2.4, can be measured; however, rather than being a top-down measurement, EDS within a TEM gains the benefit of higher spatial resolution and cross-sectional imaging. The second method is electron energy loss spectroscopy (EELS), which measures the energy lost by electrons that are inelastically scattered by the sample, resulting in a distinctive spectrum that allows for the determination of the sample's elemental composition.

2.3 Magnetic Characterization Techniques

2.3.1 SQUID Vibrating Sample Magnetometry

SQUID-VSM (Superconducting Quantum Interference Device-Vibrating Sample Magnetometry) is a very sensitive technique that utilises Josephson junctions as a method to detect minimal changes in magnetic fields. A Josephson junction is a thin break of a non-superconducting material in a superconducting wire. Installing two breaks on opposite sides of a superconducting loop forms a device called a superconducting

quantum interference device. This device is an incredibly sensitive magnetometer when constantly biased with a DC voltage. When an external field is applied through the SQUID, this current will oscillate, meaning there is a periodic relationship between the flux passing through the loop and the measured voltage across the SQUID, with a single period representing a field of one flux quantum. An explanation of this was shown by Jaklevic *et al.* [65]. A SQUID-VSM utilises a SQUID to not directly detect the magnetic moment of the sample; instead, a magnetic sample is oscillated through superconducting pick-up coils. The current and the associated field induced in the pickup coils are then passed through a SQUID, with the voltage measured across the SQUID providing highly accurate detection of the induced current, which enables the calculation of the sample's moment. SQUID-VSM measurements were performed at the Diamond Light Source using a Quantum Design MPMS 3. An image of both the instrument and measurement circuit is shown in Fig. 2.9.

This instrument was capable of applying a constant field of 5T parallel to the axis of oscillation and could cool a sample down to 4 K. Depending on the required sample alignment, two different methods were employed to secure the film. To mount the film surface in plane to the field, GE varnish was used to attach the sample to a quartz rod, which can then be inserted into the chamber containing the pick-up coils. For an out-of-plane alignment, a straw is used, where a slit in the straw is cut and the film inserted and secured with GE varnish. This technique was used for two primary measurements: magnetic hysteresis loops (moment against applied field) and moment against temperature to estimate T_{C}. Determining the ferromagnetic transition temperature of a film can be complicated, as a single domain state is required. This typically requires the application of an external magnetic field, which can affect the T_{C}. These issues are combined with

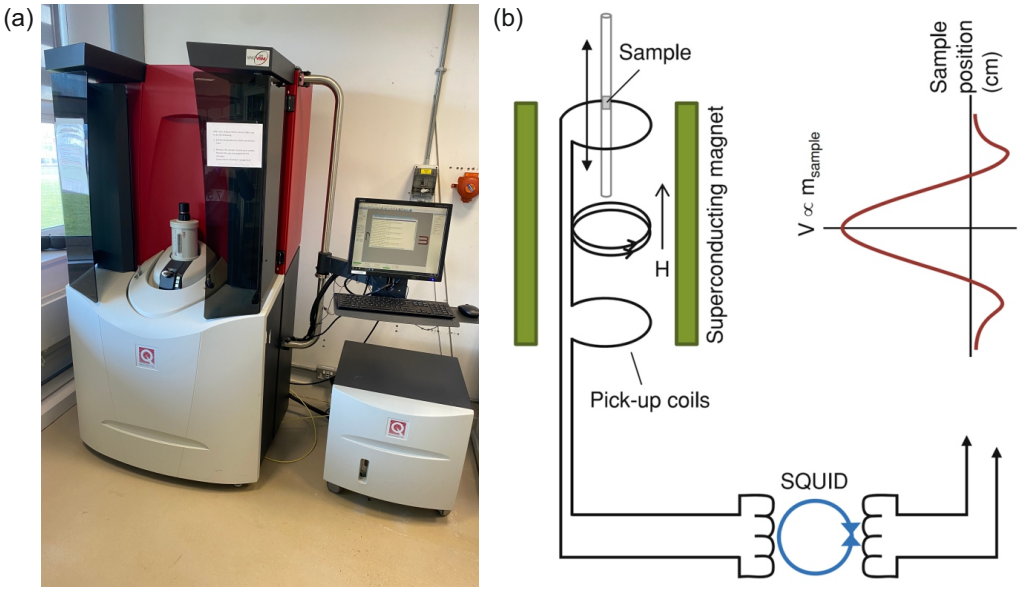


Figure 2.9: (a) Image of the MPMS 3 SQUID VSM used for this research. (b) Diagram of a SQUID VSM measurement circuit demonstrating the use of the SQUID to detect the induced current in the superconducting pick-up coils. The graph on the right of the diagram shows a typical response of the measured voltage as a sample is passed through the pick-up coils. To achieve an accurate signal, the sample must be aligned such that the centre of oscillation is on the central peak of this response. Figure (b) taken from Ref. [66].

the small coercive field typical of the films measured in this thesis, making determining T_C via taking magnetic hysteresis loops at different temperatures difficult.

2.3.2 X-ray Magnetic Spectroscopy

During this project, synchrotron-based X-ray absorption spectroscopy was used to determine magnetic properties of the film, including orbital magnetic moment and the T_C of any element within the material. Two techniques, X-ray magnetic circular dichroism (XMCD) and X-ray magnetic linear dichroism (XMLD), both rely on a difference in X-ray absorption (XAS) between opposing polarisations of X-ray light. This difference can be

measured across a range of photon energies, producing a spectrum that is characteristic of the element being measured, allowing element specificity, as well as a quantitative analysis providing estimations of orbital and total moment per magnetic ion for each magnetic element within the film. Additionally, as this technique is element-specific owing to the monochromation of the X-rays used, element-specific transition temperatures can be determined using techniques such as Arrott plots.

Circular Dichroism

In XMCD, X-rays, circularly polarised in different directions, interact with core electrons, with the strength of the interaction depending on the light's helicity. Due to the target material's magnetic properties, there will be a difference in the intensity of the energy-dependent absorption spectra taken with left μ^- and right μ^+ handed polarisations. Taking the difference of these two, the resultant spectrum shows the dichroism between the two polarisations.

The features of this resultant spectrum can be explained with a brief discussion of the preferred excitations of the $2p$ core orbital of a $3d$ metal, as illustrated in Fig. 2.10(a). The XAS absorption peaks shown in Fig. 2.10(b) represent electrons excited out of the spin-split $2p$ core state, with $j = 3/2$ (spin and orbit in parallel coupling) corresponding to the L_3 edge and the $j = 1/2$ (spin and orbit in antiparallel coupling) to the L_2 edge. This absorption process occurs in two steps: first, an X-ray photon with a helicity vector parallel to the $2p$ orbital moment preferentially excites spin-up electrons, while an antiparallel photon preferentially excites spin-down electrons. Secondly, upon excitation, electrons must locate an unoccupied hole in the valence band. If there are fewer spin-up than spin-down holes available due to the material's magnetisation, the parallel/antiparallel coupling of spin and orbit in the $2p$ core shell will cause the XMCD

spectrum to display a net negative peak on the L_3 edge and a positive peak on the L_2 edge. A full discussion of XMCD, including how multiplet effects can shape the fine structure of the spectra, can be found in Ref. [67].

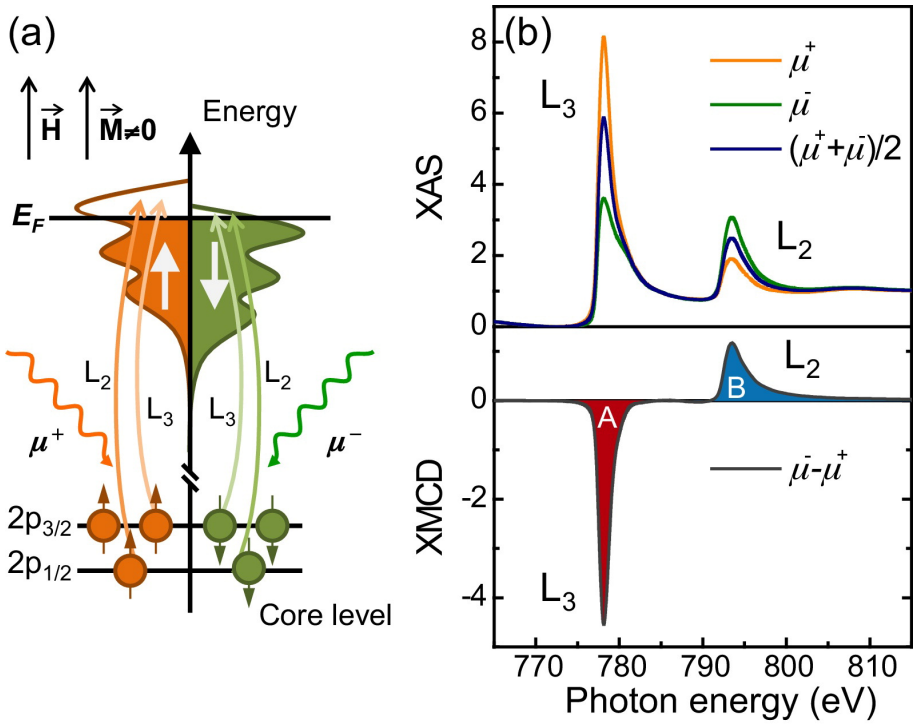


Figure 2.10: (a) Diagram showing the two-step process for XMCD in a magnetic material. Initially, a circularly polarised photon excites an electron in the $2p$ orbital. In the second step, the excited spin-polarised electrons find unoccupied states in the $3d$ band, resulting in a difference in absorption if the density of states is not equal for spin-up and spin-down electrons due to magnetic order. (b) An illustrative example showing XAS and XMCD spectra for Co at its $L_{2,3}$ absorption edges. Figure taken from Ref. [67].

Linear Dichroism

While XMCD can measure samples with a net magnetic moment, A-type antiferromagnets such as $MnBi_2Te_4$, discussed in Chapter 4, have no net moment. This means that

there is no difference in available spin-up and spin-down holes after the initial excitation of a $2p$ electron and therefore no dichroism. However, the use of linearly polarised light allows a different approach that measures magnetic anisotropy [68], achieved by taking two spectra with light polarised at right angles. Moments will now couple to the electric field perpendicular to the axis of polarisation, regardless of their direction within this axis, meaning that the square of the moment can be measured, i.e. $\langle M^2 \rangle$ [68–70]. Therefore, in isotropic magnetic systems, the measured absorption will be equal in all polarisations, resulting in no dichroism. However, if the sample exhibits magnetic anisotropy, as in A-type antiferromagnets, the spectrum will have an intensity that depends on the exact alignment with the spin polarisation, with the intensity peaking when one polarisation vector is aligned with the Néel vector and the other is perpendicular to it. Therefore, XMLD can be used as a tool to not only detect antiferromagnetism, but can also be used find the Néel vector by taking multiple pairs of 'vertical' and 'horizontal' polarised measurements subject to different rotational offsets, either of the sample or polarisation angle, and finding the angle of peak XMLD intensity.

Sum Rules

Analysis of the XMCD spectra using sum rules [71, 72] can be used to determine the spin and orbital magnetic moment per magnetic ion in the lattice. This is due to the fact that the X-ray interacts with the orbital part of the wave function, allowing an analysis of XMCD spectra to separate the spin and orbital contributions to the overall magnetic moment. This is achieved by relating the integrated intensities of the XMCD absorption edges to the magnetic ground state. In the case of $3d$ metals, these calculations use the $L_{2,3}$ absorption edges, giving the following equations:

$$m_L = -\frac{4\int_{L_3+L_2}(\mu^+ - \mu^-)d\omega}{3\int_{L_3+L_2}(\mu^+ + \mu^-)d\omega}(10 - n_{3d}) \tag{2.7}$$

$$m_S = -\frac{6\int_{L_3}(\mu^+ - \mu^-)d\omega - 4\int_{L_3+L_2}(\mu^+ - \mu^-)d\omega}{\int_{L_3+L_2}(\mu^+ + \mu^-)d\omega}(10 - n_{3d})(C - \langle T_z \rangle) \tag{2.8}$$

Where m_L is the orbital moment and m_S is the spin moment, μ^+ is the absorption spectrum when the photon angular energy is parallel to the applied magnetic field $\vec{B}$, μ^- is the absorption spectrum for the anti-parallel case, ω is the photon energy, n_{3d} is the occupation number for the $3d$ orbital, C is the correction factor for jj mixing, and $\langle T_z \rangle$ is the expectation value of the magnetic dipole operator [72, 73]. The correction factor is due to the $2p - 3d$ Coulomb interaction leads to the mixing of the $j = 3/2$ and $j = 1/2$ manifolds and is determined via multiplet calculations [74]. In order to apply sum rules, the signal must be isolated from other electronic transitions, which practically means a background subtraction to ensure there is no absorbed intensity outside the $L_{2,3}$ edges, as this would otherwise skew the results of the integrals.

Experimental Setup

Multiple synchrotron beamlines were used for X-ray magnetic spectroscopy, beamlines I06 and I10 at Diamond Light Source in Harwell, Oxfordshire, UK; beamline 29 BOREAS at ALBA in Barcelona, Spain and ID32 at the European Synchrotron Radiation Facility (ESRF) in Grenoble, France. All of these are soft X-ray beamlines with a maximum energy of approximately 1.5 keV and use superconducting magnets to provide external magnetic fields parallel to the beam direction, which is the standard direction, as circularly polarised X-rays will couple to the component of the magnetic moment parallel to their travel, meaning polarising the sample in this direction enhances the signal. These magnets vary in maximum field, but typically can achieve ∼6 T (except I10 at the Diamond Light

Source which can reach 14 T), and directionality, with some magnets able to provide smaller fields in the other two axes. X-rays are generated using a synchrotron particle accelerator, with electrons accelerated close to the speed of light before being injected into a storage ring, made up of a series of straight and curved sections, where they are held at constant velocity and directed via magnetic fields. Once the electrons in the ring are accelerated, X-rays are released through two mechanisms, both relying on Bremsstrahlung. The first mechanism occurs when electrons reach a curved section of the storage ring and release X-rays as they are accelerated around the curve. The second method uses an insertion device which uses an array of magnets to oscillate the electron beam in a straight section of the ring. The period of this oscillation can be adjusted to produce X-rays of a specific wavelength, which then travel towards the beamlines, passing through a series of focusing mirrors to tune the beam's size and focus to suit the specific demands of the beamline.

As explained in the previous sections, the X-rays incident on the sample will be absorbed. Detecting this absorption was performed using three methods, total electron yield (TEY), fluorescence yield (FY) and luminescence yield (LY), though all three could not be used simultaneously. The most widely used measurement technique is TEY, which works by making an electrical contact to the sample surface using conductive paste; this is also used to adhere the sample to the holder. This paste allows the drain current, caused by the photoelectrons released during X-ray absorption, to be measured via the sample holder. TEY is a surface-sensitive technique as the photoelectrons produced below a depth of approximately 5 nm are unlikely to escape the film before being reabsorbed. Analysis of the drain current can be performed using sum rules analysis, allowing the determination of the orbital and spin moments of ions in the film.

Fluorescence works by using a photodiode to detect emissions from Auger electrons, where electrons drop down from outer orbitals into holes in core orbitals left by X-ray absorption. This technique allows for probing through the full thickness of the film, with its penetration limits much larger than the thickness of the films used in this research. Owing to various effects such as reabsorption and secondary photons, FY measurements are not reliable for a quantitative analysis of the XMCD spectra; however, it can be used to help determine any differences between the sample surface and bulk.

For LY measurements, a photodiode is once again used; however, for this method, the photodiode is placed behind the sample, with the X-rays passing through the sample and substrate before reaching the diode. As the X-rays reach the substrate, they are absorbed and produce an exciton, which then recombines causing an optical emission from the substrate. Because the intensity of this emission is dependent on the intensity of X-rays incident upon it, and this intensity is dependent on the absorption of the film above, the XAS and XMCD spectra are therefore encoded into the visible emission, allowing measurement through the entire thickness of the film.

2.4 Growth of Topological Insulators

While this thesis primarily deals with magnetic TIs, a base undoped growth recipe for Bi_2Te_3 and Sb_2Te_3 must be established first. This section will detail the more common aspects of TI growth, such as substrate selection and sputter power, allowing for the more complicated challenges of introducing magnetism into the films to be dealt with from a more ideal foundation.

2.4.1 Bismuth Telluride and Antimony Telluride

Bismuth and Antimony chalcogenides, specifically Bi_2Te_3 and Sb_2Te_3 share very similar structures, with quintuple layer sections held together via Van der Waals forces. Every layer within each block is made up of a single element, with the crystallographic cell possessing rhombohedral symmetry, specifically the space group $R\bar{3}m$ [75]. These cells have lattice constants of a,b = 4.395 Å, and c = 30.440 Å for Bi_2Te_3 [76] and a,b = 4.264 Å, and c = 30.458 Å for Sb_2Te_3 [77]. It should also be noted that both of these materials are narrow band-gap semiconductors, with Bi_2Te_3 being a p-type and Sb_2Te_3 a strong n-type. These materials were chosen because they are the simplest 3D TIs, as their surface states consist of only one Dirac cone, as discussed in Subsection 1.2.4, making them advantageous for study. Additionally, these systems have been extensively studied and doped with a range of magnetic ions, including Mn [14–23, 78], Cr [25–30], Fe [24, 30–33], and V [26, 29, 34]. This gives this thesis a substantial amount of literature to compare results with, despite the different growth methods used in this research.

2.4.2 Substrate Selection and Preparation

A substrate was selected via several criteria. First and most important of these criteria is minimising the mismatch between the in-plane lattice parameters of the substrate and the TI, as this can induce defects of the film by causing strain in the film. Other important parameters include being transparent to allow for techniques that rely on transmission of light through the sample, such as luminescence yield in X-ray spectroscopy; and cost, as several hundred samples were required to be created throughout the project.

Taking these requirements into consideration, along with film quality as discussed in Subsection 2.4.3, c-plane sapphire, i.e. (0001) Al_2O_3 was selected. Sapphire has a lattice parameter of a = 4.785 Å giving a mismatch of 8.9% and 12.2% for Bi_2Te_3

and Sb_2Te_3 respectively. It also satisfies all the above criteria, with its widespread use in the semiconductor industry making acquisition straightforward. Substrates were purchased from Crystec, with single-side polished, 0.43 mm thick 2-inch wafers cleaved into $10 \times 10\,mm^2$ pieces. Pieces of this size were chosen as they are large enough for the clips on the holder to not significantly affect the film, as the metal contact can lead to uneven heating of the substrate in the immediate area around the clip. Equally, substrates of this size allow for two samples to fit onto the holder simultaneously, providing a backup sample to be kept clean for surface-sensitive techniques while the other can be cleaved or otherwise processed for magnetic or transport measurements.

Substrates were prepared by removing their protective polymer coating for shipping using organic solvents, deionised water and sonication, with full details of the method listed in Appendix B. The substrates were then dried using a Nitrogen gun and clipped either singly or in pairs onto the sample holder shown in Fig. 2.3(a).

2.4.3 Establishment of a Growth Recipe for Bi_2Te_3 and Sb_2Te_3

Before exploration of the parameter space to optimise for grain size without compromising crystalline structure, a basic recipe for growing a crystalline TI needed to be established.

The first parameter to be tested was substrate temperature. This was deemed most important to optimise first due to the role of temperature in both crystalline formation and grain size. It has been observed in MBE growth of chalcogenide films [79, 80] that if the substrate is not heated during deposition, the resulting film will be amorphous. However, unlike MBE, temperature cannot simply be optimised for ideal crystallinity, as this work also aims to minimise grain size to increase the contribution of surface states to the overall conductivity as discussed previously in Section 1.1. This objective ties

directly to substrate temperature due to the effect known as Ostwald ripening. Ostwald ripening, often referred to as coarsening, is an effect that extends beyond the field of thin films and covers any two phase mixture, which, as it is cooled into a single phase, will reduce its total energy by increasing the radius of particles present in the mixture [81]. In the case of thin films, when a nanocrystalline film is held at a high enough temperature to allow the atoms some mobility during growth, the energy held within the high curvature surface of the smaller grains will be reduced by favouring larger grains with a lower interfacial curvature [82]. Therefore, leaving the temperature too high can result in larger grain sizes, even without a prolonged annealing process, by increasing the mobility of ions within the film during growth. As a result of these competing effects, an exploration of an optimal growth temperature must be detailed, using XRD and AFM to determine crystallinity and grain size, respectively. Grain size was determined through a combination of watershed flooding, where local minima are 'filled' to a certain depth and measuring the remaining islands, and the distance between peaks on profiles extracted randomly across the image used to check the result. The results of such a study on Bi_2Te_3 films grown on (001) thermally oxidised Si (and one on Al_2O_3) can be seen in Table 2.1, where a clear minima at 150°C of 35 nm, and a second lowest point at 250° of 50 nm can be observed. This complex relationship could be due to a number of factors, such as the 'sticking coefficient' of incident atoms with the substrate, nucleation, and Te desorption at higher temperatures. It is important to note that at 250°C, substrate choice did not effect grain size.

While it would seem that 150°C would be the ideal choice, crystallinity is also an important factor, with Fig. 2.11 showing XRD measurements of films grown on different substrates at varying temperatures. Here is can be seen that Bi_2Te_3 only grew

#	Substrate Temperature (°C)	Average Grain Diameter (nm)	Film Thickness (nm)
238	120	61±4	10±2
234	150	35±3	14±1
232	180	58±4	15±1
235	250	50±3	3±2
361 (on Al_2O_3)	250	52±2	14±1

Table 2.1: Table showing the relationship between substrate temperature and grain diameter for Bi_2Te_3 films deposited on thermally grown SiO_2 (with a single film on Al_2O_3 for comparison). A non-linear relationship between the two can be seen, with a clear minima in grain size at 150°C, and that substrate choice did not substantially effect grain size.

amorphously on SiO_2, however on Al_2O_3 weak *c*-axis ordering can be seen at 180°C with strong order at 250°C. This is thought to be due to Al_2O_3 having a reduced lattice parameter mismatch with Bi_2Te_3 compared to thermally oxidised Si. However, the weak nature of the ordering, combined with the additional peak at ∼21°, most likely caused by misaligned Bi_2Te_3 layers, shifting the (101) peak, clearly shows the need for improved crystallinity. Order was further enhanced by the addition of a nucleation layer at a lower temperature before growing the main layer, also shown in Fig. 2.11. This helps ease the strain on the film caused by lattice mismatch with the substrate and allows for the main layer to deposit onto a layer of Bi_2Te_3. In this instance, a 1-2 nm layer was deposited at 200°C, leading to the conclusion that films grown at a temperature of 250°C with this layer present would provide the optimal film when balancing grain size and crystalline order. It should be noted that in Fig. 2.11 a sharp peak can been seen around 20°. This is likely a substrate peak that although usually forbidden for Al_2O_3, is likely caused by multiple reflections within the lattice, resulting in a visible peak at this angle.

The second key parameter to optimise is deposition/growth rate. This is primarily

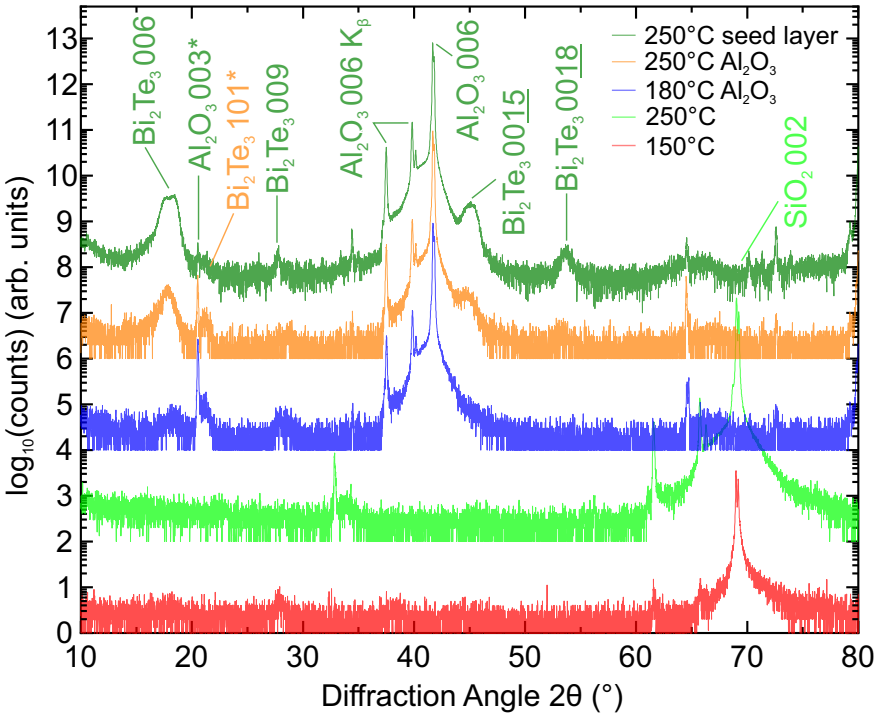


Figure 2.11: XRD of Bi_2Te_3 thin films differentiated by growth temperature and substrate, vertically offset for clarity. The films labelled 150°C and 250°C were grown on (001) SiO_2 and display no *c*-axis crystalline order. The remaining films, grown on (0001) Al_2O_3 show strengthening crystalline order with increasing substrate temperature, with the best result achieved at 250°C with a 1-2 nm 'seed' or nucleation layer deposited first at 200°C to encourage crystal growth by reducing lattice mismatch with the substrate.

affected by sputter power, while also being affected by factors such as substrate material and growth temperature. While growth rate can affect the growth modes for materials, a full exploration of this parameter was limited by the requirements of co-sputtering for doping. This is because to keep the transition metal concentrations within the low doping limit (estimated to be $\approx 10\%$), the growth rates of TI and metal targets needed to be kept in a ratio of between 10-100:1 to allow for multiple doping concentrations

to be produced. Deposition rates were determined by growing films at multiple powers for a fixed time and measuring their thickness, and then fitting the Kiessig fringes in XRR using the open-source software GenX 3. These thicknesses are then converted into growth rates and fitted under the assumption that the growth rate is linear with sputter power. From this data, two methods were attempted to obtain an accurate estimate of the growth rate. First, a linear fit of thickness against sputter power[3] was taken to obtain growth rate. However, owing to errors in growth time and the time required to grow enough films to get an accurate fit, an alternative method of taking films' thicknesses and calculating an average growth rate expressed in $\mathrm{nm\,s^{-1}\,W^{-1}}$ was used. This method was found to be more accurate and allowed a growth rate at any power to be estimated and a predictable film thickness with less than 1 nm of error. This process needed to be repeated often as growth rates were variable over the course of the project. The deposition rate of each target is sensitive to other factors such as target thickness, which reduces very gradually as the target is used, and chamber conditions, which change every time the chamber is exposed to atmosphere. As such, growth rates will be discussed when relevant in each chapter, but in general, the high growth rates of TIs, when compared to transition metals, combined with the target stoichiometry leads to a TI sputter power of 30 W being used as a standard throughout this thesis. This power is shown to result in high-quality, epitaxial growth of layers within the film with the desired defect density, while being deposited at a high enough rate ($\approx$0.3-0.6 $\mathrm{nm\,s^{-1}}$) to allow for fine control over the concentration of any dopants introduced.

In summary, this section has discussed the optimisation of a growth recipe for Bi_2Te_3 using crystallinity, assessed by XRD measurements, and grain size, determined by watershed flooding of AFM images, as the main factors for determining film quality. AFM

[3]This relation is expected to be linear up until high powers.

was also used to determine the film roughness via an RMS roughness calculation, yielding a grain diameter of 50 nm and a surface roughness of 1-2 nm. Additional parameters of film thickness and composition were determined by fitting XRR curves and SEM-EDS spectra, respectively. Typical films in this thesis ranged from 12-28 nm thick with a composition of (42±1)% Bi and (58±1)% Te, with the slight deficiency in Te likely caused by desorption as the film cooled after growth. The specifics of the samples discussed in the following chapters were based on this growth methodology and were characterised using the methods detailed in this section and the rest of Chapter 2, with any deviations or alternative methods noted as they become relevant.

2.5 UV Photolithography

When electronic and spin transport measurements were required, nanofabrication of Hall bar devices using UV photolithography was performed. This was performed in collaboration with Dr. Angadjit Singh, who led and conducted most the cleanroom work presented in this thesis. The author's contributions were primarily testing and optimization, particularly with regards to the etching recipe and electrical contact deposition. UV photolithography is a common technique used for fabricating devices with spatial features in the order of hundreds of nanometers. This is achieved by using spin-coated resists, which are polymers with chemical bonds that either break down or harden under exposure to UV light, and therefore are more or less soluble in a developing chemical. These two types are known as positive and negative photoresists, respectively. The method described in this section only uses positive resists, where the resist is developed in such a way to protect the desired area from processes that either add or remove material from the rest of the film, allowing the patterning of devices. These areas are defined by the use of lithography masks, where precisely shaped metallic films

are patterned on glass plates and placed between the sample and a UV lamp, shielding certain areas of the resist-coated sample from light and therefore preserving the resist in these areas. This technique is limited in its spatial resolution by the wavelength of UV light, as diffraction through narrow gaps in the mask becomes a limiting factor. However, this technique is much faster and more cost-effective than electron beam lithography, where a fine beam of electrons is used to develop the resist. This section will detail the preparation of a cross-pattern hall bar used in Chapter 5, from spin coating resists to etching unwanted material, and finally, the deposition of contact pads for electrical measurement.

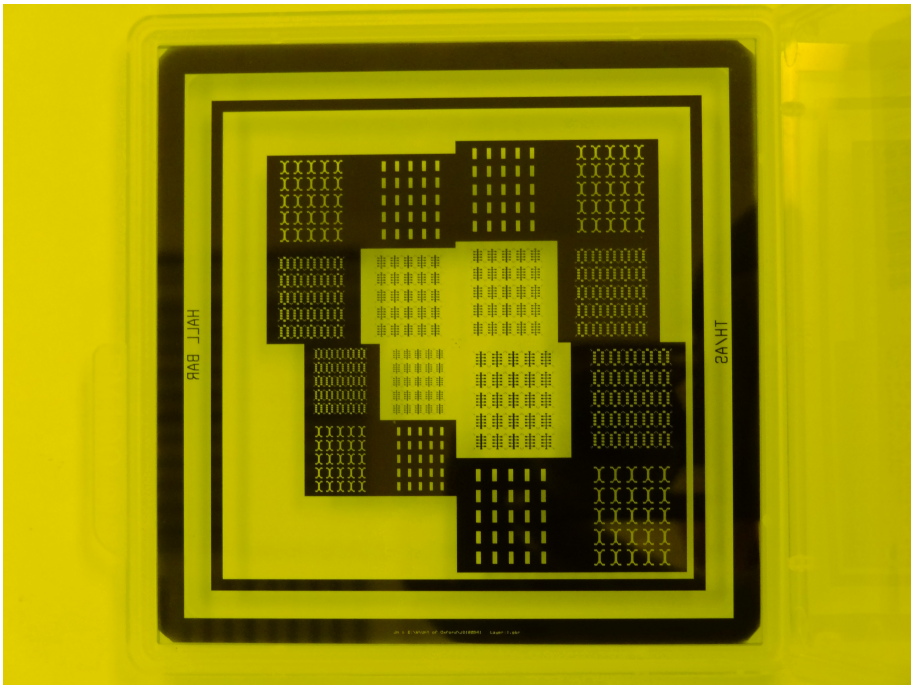


Figure 2.12: Image of a UV photolithography mask used to pattern Hall bars. The first stage masks can be seen in the centre and the second stage mask for the electrical contacts around the outside.

The first step of this process was the spin coating of 1813 photoresist using a two-stage spin process of an initial stage of 10 seconds at 500 rpm followed by a minute at 4500 rpm. This was followed by a 2-minute bake at 90 °C before the sample was placed under a photolithography mask and exposed for 7 seconds with no wavelength filters. The lack of a filter was decided to ensure a rapid and complete development of the resist, and due to the feature size, a higher spatial resolution was not required. The film was then removed from the mask aligner and developed in MF319 for 21 seconds to remove the excess resist before a 6-minute exposure in the reactive ion etcher. Reactive ion etching (RIE) is essentially a sputter chamber where the sample serves as the target, with ions bombarding it to remove material. This means the areas unprotected by photoresist, i.e the areas exposed to UV, are etched away while the desired structure is protected under the resist. The etching process can be tuned with many of the same parameters as sputtering, including pressure, the gases used, and the power used to generate the plasma. These parameters adjust the rate of etching as well as the rate of lateral etching, where material is removed from the side of any structures, which must be managed to ensure the desired features are not etched via an undercut of the resist. However, a small amount of lateral etching is helpful during the next step of lift-off. Using test samples, optimal parameters were found to be a 6-minute etch using an Ar flow rate of 25 SSCM at 115 W.

Once the undesired film has been etched away, the sample is placed in 1165 lift-off chemical to remove the photoresist. This process is often accompanied by sonication to provide agitation to remove the resist; however, owing to the weak interlayer van der Waals bonding in the TIs used, a disposable pipette was used to provide a milder agitation to prevent the film from being damaged. Following the completion of the lift-off,

the films were then immersed in acetone, isopropanol and deionised water, and were subjected to the same gentle agitation at each stage.

While the first stage forms the devices into the shape of the mask, in this case a cross pattern hall bar, a second stage of lithography is required to deposit a Cr/Au electrical contact pad for wire bonding the hall bars into chip carriers for measurement. This stage requires the deposition of two layers of photoresist to generate an undercut, providing for a clean lift-off at the end of the process. The first layer of resist was PMGI spun for 10 seconds at 500 rpm, then 60 seconds at 3000 rpm, and baked at 190 °C for two minutes. The second layer was the same 1165 resist layer as the first stage; however, with a slightly hotter bake at 110 °C to ensure the resist fully bakes with the extra thermal mass of the additional layer of resist.

The film is then placed in the mask aligner, with extra care taken to align the patches with the existing structures from the previous stage, exposed to UV for 7 seconds, and developed in MF319 for 40 seconds. To develop the undercut, the film was etched once again in a much lower power system, so that the PMGI resist is etched away to form the undercut.

Once this process was completed, the sample was then ready for the deposition of the contact patch, with the resist protecting the areas of the sample outside of these desired areas. Deposition was performed using a thermal evaporation chamber, where small amounts of material are heated to cause sublimation, allowing the free atoms in the chamber to travel and recondense on the sample. First, a thin Cr layer of 5 nm was deposited to assist in adhesion for the Au layer, which is much thicker at around $\sim$80 nm. This relatively high thickness was required for the layer to mechanically and thermally survive the wire bonding phase. With a layer of Cr/Au now deposited at the ends of

the ‘arms’ of the Hall bar, the same lift-off process is performed as in stage 1. The finished devices are cleaved and then wire-bonded onto chip carriers for measurement. The devices were mounted on the chip carriers using GE varnish and wire-bonded using a ball bonder, a device that uses a high-voltage pulse to melt a thin Au wire into a free-air ball. This ball is then bonded to the chip holder using pressure, heat, and ultrasonic vibration. The wire is then moved to the next contact point, and a second bond is formed using the same combination of pressure, heat and vibration. Then the wire is clamped and broken, leaving a connection between the two points. The chip carrier can then be placed upon the probe and inserted into the magnet for SOT measurements, which are detailed in Section 5.3.

Chapter 3

Transition Metal Doping of Topological Insulators

3.1 Motivation

Substitionally doping TIs with $3d$ transition metals is an established method to break time-reversal symmetry and explore emergent effects such as the QAHE. While these materials and dopants are established, synthesising these films in specifically nanocrystalline forms has not been explored. Sputtering, tuned explicitly for nanocrystalline growth, could result in differences in clustering, preferred dopant sites, or secondary phases. As such, this chapter will focus on the growth and characterisation of two different doped TIs, Mn:Bi_2Te_3 and Cr:Sb_2Te_3, focusing on both structural and magnetic studies, specifically examining how the structural properties of the film influence the magnetic ground state.

The substitutionally doped TI Mn:Bi_2Te_3 was one of the earliest TIs to be shown to break time reversal symmetry by Hor *et al.* in single crystal form [14], with ferromagnetic order exhibited at Mn concentrations of $x = 0.04$ and above at a T_C of ∼9-13 K. The introduction of magnetic ions was also experimentally shown to result in a band gap opening at the Dirac point via angle-resolved photoemission spectroscopy (ARPES) in thin films grown via MBE [83], with a reported T_C of 45 K.

However, work on these materials has primarily been focused on single crystals and MBE-grown thin films [14–23, 78], leaving the exploration of doping via magnetron sputtering as a potential avenue of research. As such, this chapter will detail efforts to introduce Mn into the Bi_2Te_3 lattice, substituting Mn for Bi and measuring its magnetic properties. Equally, if other doping mechanisms are present, measurements must be undertaken to determine how they affect the film's magnetic order, as these 'undesired' growth modes may reveal interesting properties.

To achieve this, a detailed growth methodology is described, involving a series of samples grown at varying doping concentrations using different methods. These samples were then studied via extensive X-ray diffraction and electron microscopy to determine the film's stoichiometry and crystallographic structure. Following a determination of the quantity and distribution of the Mn within the lattice, SQUID and XMCD studies determined the magnetic ordering, T_C and orbital moment of the Mn atoms within the lattice. Finally, a conclusion draws links between structural and magnetic measurements, with an emphasis on how doping concentration affects the films' properties.

Following the presentation of the Mn-doped results, Cr:Sb_2Te_3 thin films are explored. Cr- and V-doped Sb_2Te_3 are well established magnetic TIs [21, 26], with T_C in excess of 100 K [84, 85]. However, exotic effects such as the QAHE are still only observed at temperatures of $\lesssim 2$ K [84, 85], with the disparity attributed to magnetic disorder and inhomogeneity. This can be caused by the clustering of magnetic ions, phase segregation, and Dirac-mass disorder [85].

These existing results on MBE-grown thin films could be further advanced through the use of magnetron sputtering, with existing results showing nanocrystalline TIs exhibiting different morphologies [37, 86, 87]. This difference in crystallinity and local disorder

could affect dopant solubility and magnetic exchange pathways when compared to MBE films.

In order to explore this, a study similar to the one presented for Mn:Bi_2Te_3 was carried out, using X-ray diffraction, electron microscopy, magnetometry, and magnetic spectroscopy to understand the growth-structure-magnetism relationship in sputtered Cr:Sb_2Te_3 films. Once these results were obtained, a discussion and comparison with existing results for MBE films was undertaken, placing the sputtered films in the broader context of MTIs.

3.2 Mn-doped Nanocrystalline Bi_2Te_3 Thin Films

3.2.1 Growth of Mn:Bi_2Te_3 Thin Films

Mn-doping was achieved by using the substrate preparation and two-stage growth technique on *c*-plane Al_2O_3 detailed in Section 2.4. First a $\sim$1.5 nm nucleation layer of undoped Bi_2Te_3 was deposited at 30 W with a growth rate of approximately 0.32 nm s^{-1} at a pressure of 1.2×10^{-2} mbar. Following this, the substrate was heated to 250 °C and a $\sim$25 nm main layer was deposited under the same growth conditions. To dope this main layer, Bi_2Te_3 and Mn were co-sputtered, i.e. simultaneously deposited from separate targets at a range of Mn sputter powers (between 1-10 W).

To give a broader range of doping concentrations, two methods of co-sputtering were used to control the effective Mn deposition rate: continuous and pulsed co-sputtering. This is due to the ratios between the Mn and Bi_2Te_3 growth rates (5.7:10.5 $\times 10^{-3}$ nm s^{-1} W^{-1}), meaning that achieving low dopant levels at a growth power of 30 W for Bi_2Te_3 required growth powers below 1 W for Mn, which was not possible for the power supplies used. As such, a pulsed co-sputtering approach was employed, where the Mn shutter was opened and closed throughout the growth process. While this could lead to a layered sample

with alternating layers of high and low Mn density, it was expected that the growth temperature of 250 °C would allow for a sufficiently high Mn mobility to effectively 'anneal' the sample, resulting in an even distribution of Mn throughout the film. The mobility granted by the growth temperature was also expected to allow Mn to travel into the nucleation layer, effectively removing the distinction between the nucleation and main layers. To protect these samples from oxidation, the sample was cooled to room temperature and a 3-4 nm layer of Al was deposited at a power of 10 W at a deposition rate of $0.0373\,\mathrm{nm\,s^{-1}}$. This layer was expected to oxidise into AlO_x nearly completely.

While the ratio of the growth rates allows for an estimate of the doping concentration, it is unlikely that all the Mn would incorporate with the Bi_2Te_3 as the predominantly TI film would reduce the sticking coefficient of the Mn. To determine an accurate value for the Mn content within the film, SEM-EDS was used to determine the film's composition. While SEM-EDS can be unreliable at low doping concentrations, alongside the reduced count rate due to the presence of the capping layer, several measurements were made on each sample at different sites and magnifications to minimise potential errors. The results of these measurements on an Mn:Bi_2Te_3 doping series, alongside the Mn sputter power, estimated Mn concentration derived from growth rates, and if pulsed sputtering was used, are shown in Table 3.1.

Once the growth of TIs had been completed, structural characterisation was undertaken using a range of XRD techniques, including thin film XRD, GI-XRD and RSM. In addition to XRD, electron microscopy was used to accurately assess sample composition and image the film's structure using both SEM and cross-sectional TEM. Surface morphology and grain size were determined using AFM in tapping mode. Magnetic characterisation of the film was performed using SQUID magnetometry to take both

Mn sputter power (W)	Nominal Mn Concentration (at. %)	Measured Mn Concentration (at. %)	Measured Bi Concentration (at. %)	Measured Te Concentration (at. %)
1 - pulsed	0.8	0.8 ± 0.1	38.7 ± 0.4	58.8 ± 0.5
2 - pulsed	1.7	1.6 ± 0.1	40.1 ± 0.4	58.3 ± 0.5
2	3.5	3.5 ± 0.4	39.5 ± 0.2	57.0 ± 0.3
4 - pulsed	3.5	3.8 ± 0.3	38.4 ± 0.1	56.8 ± 0.1
4	7.0	6.0 ± 0.5	38.0 ± 0.5	56.0 ± 0.5
6	10.6	8.5 ± 0.1	38.2 ± 1.0	53.4 ± 1.0
10	17.7	11.7 ± 0.1	36.7 ± 0.1	51.6 ± 0.1

Table 3.1: Table showing EDS analysis of a series of Mn-doped Bi_2Te_3 thin films. Nominal Mn concentration describes the expected value based on growth rates. It can be seen that Mn fully incorporates into the film at nominal concentrations below ∼5%; however, beyond this, the correlation between sputter power and measured Mn concentration breaks down. It should also be noted that the two samples with a 3.5% nominal Mn concentration were produced to ensure the pulsed and continuous methods yield similar results. Table adapted from Ref. [62].

$M(H)$ and $M(T)$ measurements. In addition to this, element-specific XMCD on the I10 beamline at Diamond Light Source was used to determine information about the magnetic ground state at a range of conditions, including a 14 T applied field within the superconducting magnet.

3.2.2 Structural Analysis of Mn:Bi_2Te_3 Thin Films

XRD measurements on a series of Mn-doped samples, conducted at room temperature, shown in Fig. 3.1(a), show peaks characteristic of Bi_2Te_3 with the $R\bar{3}m$ space group. Note the films have been labelled with their measured Mn concentration from the SEM-EDS data shown in Table 3.1. For the undoped film, the calculated c-lattice parameter is (31.4±0.1) Å. The c-lattice parameter decreases slightly when doping is at low levels, as

Mn substituting for Bi will reduce the lattice parameters owing to its relatively smaller atomic radius. This results in a reduction down to (31.1±0.1) Å and (30.6±0.1) Å at 0.8% and 6.0% Mn, respectively. However, beyond 6% Mn concentration this behaviour shifts and the c-lattice parameter increases, reaching (31.9±0.1) Å and (32.3±0.1) Å at 8.5% and 11.7% Mn, respectively. This change in trend suggests that there is a critical level that, if exceeded, the mechanism by which the Mn incorporates into the lattice shifts away from the desired substitution at Bi sites.

There are numerous possibilities for Mn sites within the lattice, including Mn occupying sites in the van der Waals gap between quintuple layers, forming a structure akin to $MnBi_2Te_4$ where a MnTe bilayer sits in between Bi_2Te_3 quintuple layers. This could explain the expansion of the c parameter, as $MnBi_2Te_4$ has a larger unit cell composed of repeating septuple layers compared to the quintuple layers of Bi_2Te_3. Alternatively, the Mn could sit outside of the Bi_2Te_3 unit cell, clustering either by itself or forming $MnTe_x$. This is supported by the additional peaks observed in Fig. 3.1, which increase with Mn concentration. These peaks are consistent with $MnTe_x$, suggesting that the formation of clusters is likely.

As XRD in symmetric $\theta - 2\theta$ geometry only probes in the c-plane, and the presence of secondary phases had been observed, GI-XRD was used to investigate any structures that had formed off-axis. GI-XRD utilises a fixed incidence angle, in this case 4°, and sweeps 2θ, the breaking of this $\theta/2\theta$ symmetry allows the measurement of off-axis diffraction peaks.

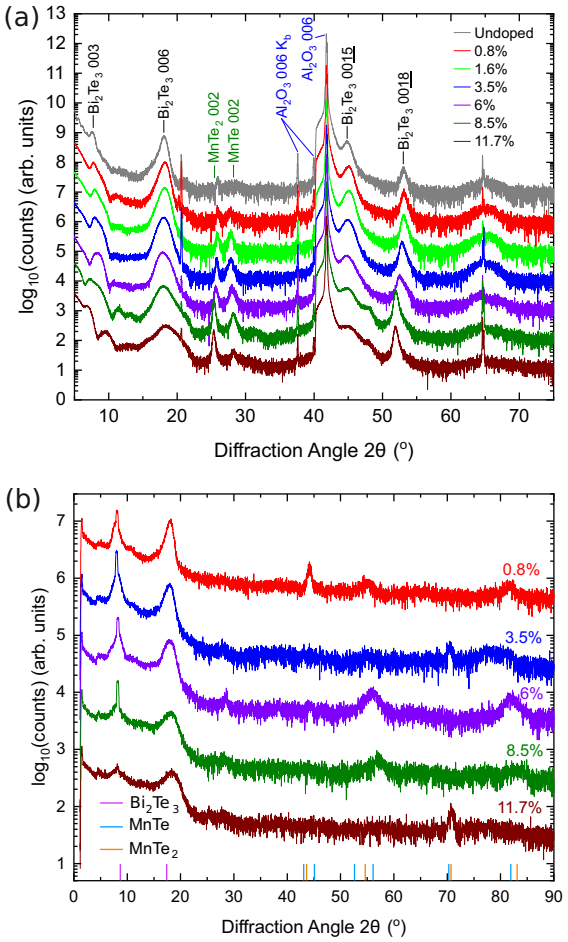


Figure 3.1: (a) XRD diffraction patterns of a series of Mn:Bi_2Te_3 thin films. The films are ordered in increasing Mn concentration (from top to bottom, offset for clarity). The primary Bi_2Te_3 peaks are clear; however, peaks resulting from secondary phases, likely from $MnTe_x$ c-plane reflections, are also visible. It is challenging to identify the secondary peaks as they overlap with multiple compounds and minor peak shifts due to strain caused by lattice mismatch with the substrate. However, it can be seen that their intensities relative to the Bi_2Te_3 $(003\underline{l})$ peaks increase with Mn concentration. (b) GI-XRD patterns for the same doping series, diffraction peaks corresponding to Bi_2Te_3 MnTe, and $MnTe_2$ are all visible and are labelled above the x-axis. As the peaks are not consistent across all films, it can be suggested that $MnTe_x$ has grown with varying preferred orientations in each film. Figure taken from Ref. [62].

Results of these measurements can be seen in Fig. 3.1(b) and show inconsistent results between samples. However, all of the peaks either correspond to Bi_2Te_3 or $MnTe_x$, with the inconsistency due to the random orientation of $MnTe_x$ grains within each film. This randomness is unsurprising, given the granular growth expected of a magnetron-sputtered thin film, especially when two different phases with distinct space groups are growing alongside each other.

To obtain a more complete picture of the secondary phases and the effect of Mn doping on Bi_2Te_3 crystal structure, RSMs were acquired by sweeping χ and 2θ through ranges from -5° to 65° and 0° to 100°, respectively. The resulting RSM plots are displayed in Fig. 3.2. Analysing the plots in Fig. 3.2 confirms secondary peaks at high doping concentration, consistent with $MnTe_x$. In addition, it can be seen that the structure, while looking similar in the *c*-plane, is significantly different at the highest doping concentration. Several Bi_2Te_3 peaks cannot be seen out of the *c*-plane, and in their place, some peaks for $MnBi_2Te_4$ can be observed. This illustrates, in addition to the data shown in Fig. 3.1, that beyond a certain threshold, the dopant behaves differently within the film, incorporating interstitially instead of substitutionally.

Reciprocal space mapping in the Q_x-Q_z plane was performed by scanning through ω and $2\theta/\omega$, and the resulting plots are shown in Fig. 3.3. The FWHM maximum of the peaks was analysed using the Scherrer equation, which allows for a comparison between peak width and grain size [88]. This analysis reveals a broadening in both axes, predominantly along the Q_z axis, with the 0.8% sample exhibiting a 22% increase in width and the 6% sample displaying a substantial 104% increase compared to the undoped sample. It can also be seen that at some point above 6% doping, the amplitude of the peak decreases significantly, falling by a factor of ∼3 by 11.7%, and the broadening continues to

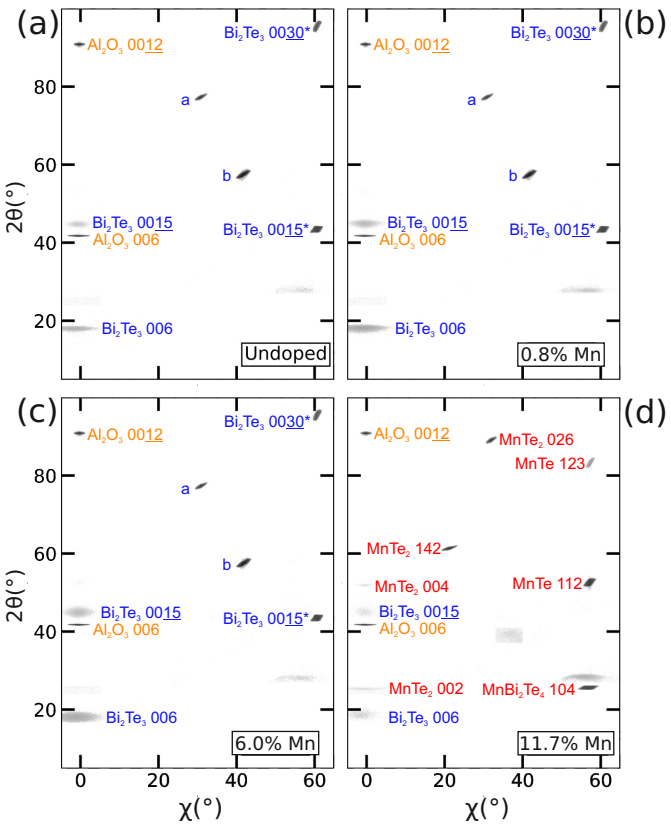


Figure 3.2: Asymmetric RSMs for a selection of the Mn:Bi_2Te_3 series: (a) undoped, (b) 0.8%, (c) 6.0%, and (d) 11.7%. The undoped sample shows only Bi_2Te_3 and Al_2O_3 peaks. In (b,c), despite the presence of secondary phases seen in Fig. 3.1, the intensities of these peaks are below the detection threshold for the RSM geometry, which has more noise due to the removal of the receiving optics to enable the use of the 2D detector. The broadening of the peaks in (b, c) suggests an increase in grain size when compared to the undoped sample. In (d), the Bi_2Te_3 peak intensities significantly decrease, with the $MnTe_x$ and $MnBi_2Te_4$ peaks becoming visible; the presence of the latter suggests that the doping mechanism has changed at higher Mn concentrations. The peaks labelled a and b can be indexed with Bi_2Te_3 peaks $(\bar{1}\bar{1}\underline{20})$ or $(\bar{2}\underline{120})$ and $(\bar{1}\bar{1}\underline{13})$ or $(\bar{1}\underline{213})$, respectively. Peaks marked with an asterisk are attributed to their associated c-axis orientated columnar domains (at a matching 2θ) with a $\sim$60° rotation from the surface normal. Figure adapted from Ref. [62].

become more pronounced. This change in character emphasises the structural breakdown of the Bi_2Te_3 phase at higher dopant concentrations, with an increasing amount of $MnTe_x$ and $MnBi_2Te_4$ within the film.

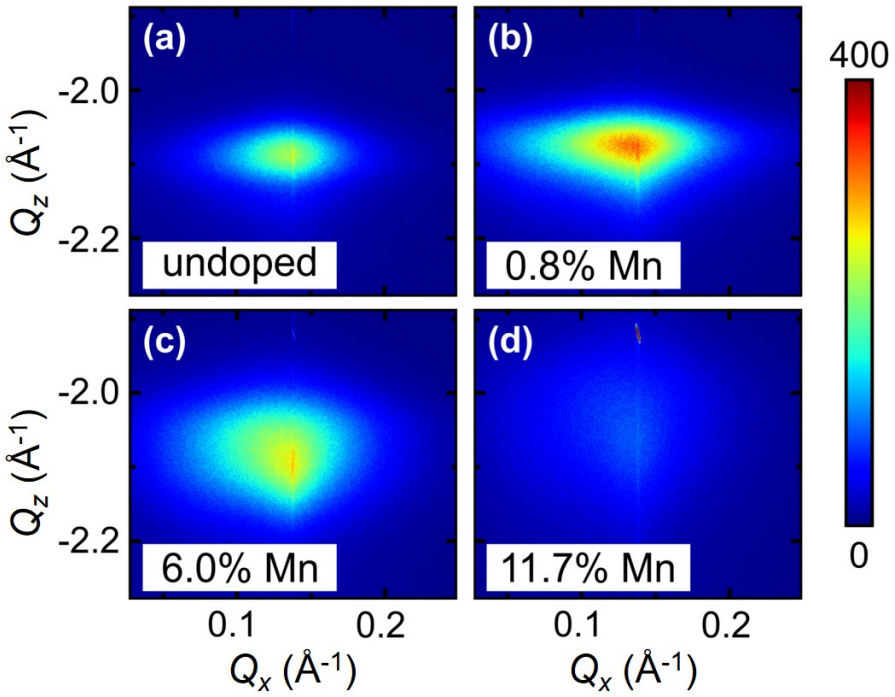


Figure 3.3: RSMs of the (006) peak for a selection of the Mn:Bi_2Te_3 series: (a) undoped, (b) 0.8%, (c) 6.0%, and (d) 11.7%. Peak broadening in the Q_z and Q_x directions can be seen in (b, c) when compared to the undoped sample, suggesting that doping caused structural changes such as increased lattice distortion and reduced crystalline coherence. In (d), a significant loss in intensity can be observed, which, when combined with the observations in Fig. 3.2, suggests that a transition from substitutional doping to a structure more akin to $MnBi_2Te_4$. Figure taken from Ref. [62].

To understand the effects of doping on grain size and surface morphology beyond what can be gleaned from reciprocal space maps, AFM was performed. Images representative of an undoped and 3.5% Mn are shown in Fig. 3.4(a) and (b), respectively. The

nanocrystalline nature of the film is apparent, with no visible anisotropy regarding grain orientation in either sample. Grain sizes were analysed by setting a threshold depth of 5 nm and analysing the top layer of grains. Two distinct grain sizes were identified in the doped sample, with grains measuring 60-70 nm and 110-120 nm in diameter. Both of these grain classifications are clearly larger than the undoped sample, highlighting the presence of multiple growth modes in the film, with the size potentially being a function of Mn concentration. The increased grain size, when compared to the undoped sample, suggests that Mn alters the growth mode, even at a low level, by promoting grain coalescence and clustering. While it fell outside the purview of this project to explore how strain and disorder caused by grain boundaries affect the magnetic properties of the film, the grain size of magnetic samples with the same doping concentration could be tuned to investigate the connection between these properties.

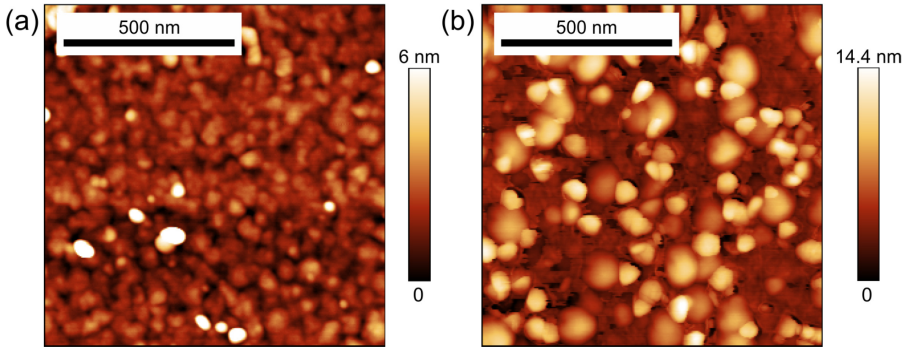


Figure 3.4: AFM images of (a) an undoped Bi_2Te_3 sample and (b) a 3.5% Mn:Bi_2Te_3 film. It can be observed that the dopant causes significant changes to the surface morphology, with increased grain sizes and higher roughness being visible in the doped sample. Setting the threshold to 5 nm, the grain size distribution can be analysed, with (b) having two dominant grain sizes of 60-70 and 110-120 nm. These distinct grain sizes suggest that multiple growth modes are present within the film. Figure taken from Ref. [62].

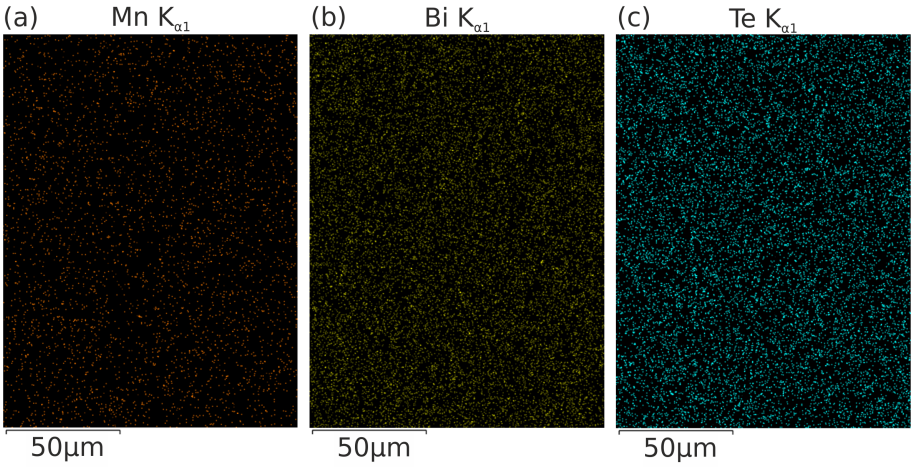


Figure 3.5: EDS element maps of a 1.6% Mn sample at a single site, showing small variations in the concentration of all three elements across the sample. However, statistics are somewhat limited by the presence of the AlO_x cap on the films, which reduces the count rate for the bulk of the film underneath. Unlike the AFM, there is little evidence of clustering over the larger length scale of the EDS scans. This allows us to assume that the AFM and TEM measurements are representative of the entire sample.

SEM-EDS data, shown in Fig. 3.5, shows an even distribution of Bi and Te, with minimal spatial variation in composition on the measured length scales. Therefore, to understand both the defects between grains and better image inhomogeneity in dopant concentration, STEM was used, with data taken by B. Achinuq and S. J. Haigh at the University of Manchester. STEM-EDS elemental mapping was used to investigate the incorporation and spatial distribution of Mn dopants in the films. In contrast, BF and HAADF STEM were used to image the film's structure. It should be noted that the imaging of Mn may be difficult in HAADF due to the low atomic number (Z) of Mn (25) when compared to Bi (83) and Te (52), combined with the low concentration of Mn within the film. Bright-field STEM images, shown in Figs. 3.6 and 3.7, illustrate the films' c-plane-oriented granular structure. A high degree of order can be seen in

the grains, with the characteristic quintuple layers of Bi_2Te_3, indicating a successful integration of Mn into the Bi_2Te_3 lattice without compromising the layered structure.

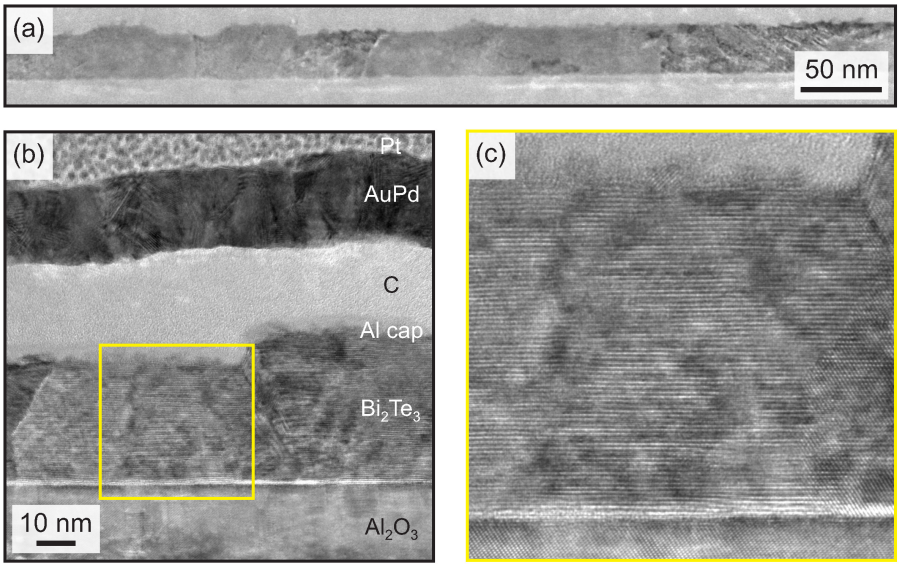


Figure 3.6: Bright field TEM images of a Bi_2Te_3 film doped 1.6% Mn. (a) A cross-sectional view shows the film to be ∼25 nm thick, showing the surface roughness. (b) Image of the whole stack, including the protective layers of C, AuPd, and Pt used in sample preparation. The *c*-plane aligned layers can be observed, and discontinuities within these layers are also visible, particularly to the right of the highlighted area. (c) Magnified view of the highlighted area in (b) reveals individual Bi_2Te_3 quintuple layers, showing the film is c-axis orientated. However, off-axis growth can be observed on the right side, suggesting the formation of a secondary phase. Figure taken from Ref. [62] with data collected by B. Achinuq at the University of Manchester.

However, discontinuities and off-axis growth are present within the film, potentially serving as the locus of the secondary phases or clustering, as evidenced by the XRD and AFM results. To test this assertion, HAADF STEM images were collected alongside EDS maps for the two samples imaged in Fig. 3.6 and 3.7. Once again, the quintuple layers of Bi_2Te_3 can be observed, and no clear variation in the distribution of Bi and Mn

is visible in the EDS maps. However, there is a variance in intensity across the HAADF images, which, taking into consideration the Z dependence of the HAADF signal, could correspond to compositional variation.

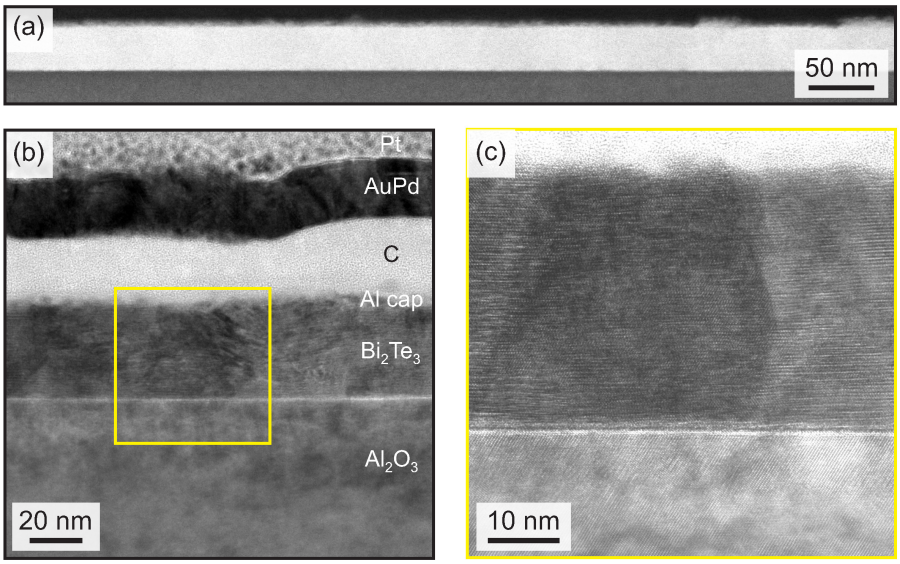


Figure 3.7: Bright field TEM images of a Bi_2Te_3 film doped 3.8% Mn. (a) A cross-sectional view showing that the film has reduced roughness compared to the film shown in Fig. 3.6. (b) Image of the whole stack, including the protective layers of C, AuPd, and Pt used in sample preparation. The *c*-plane aligned layers are visible, and discontinuities within these layers can also be observed. (c) Magnified view of the highlighted area in (b) reveals individual Bi_2Te_3 quintuple layers, with a significant area of off-axis growth visible with a different structure than the 'normal' Bi_2Te_3. Figure taken from Ref. [62] with data collected by B. Achinuq at the University of Manchester.

To test this, EDS spectra were collected in both light and dark regions for the HAADF image of a 1.6% shown in Fig. 3.8. The Mn peak at 5.9 keV was integrated and normalised by the total spectral integral, accounting for any potential co-dependencies of the different peaks. This analysis yields the conclusion that the Mn content in the bright regions is ∼35% higher than in the dark areas, confirming that composition variation

can be observed and measured across the sample. To analyse the extent of these areas, the HAADF images were thresholded to distinguish light and dark regions, and then their areas were calculated to determine the proportion of the film that comprised each area. By performing this technique at varying magnifications across multiple sites per sample, it was determined that ∼68% of the film consists of Mn-rich regions. Combining the STEM analysis and XRD data, it is reasonable to assert that the Mn-rich regions contain a mix of substitutionally doped Bi_2Te_3 and $MnTe_x$ phases, with the relatively even distribution of Bi and Te content on the EDS maps suggesting that Bi_2Te_3 remains the dominant phase throughout the film.

3.2.3 Magnetic Characterization of Mn:Bi_2Te_3 Thin Films

Magnetic characterisation prior to measurement on a synchrotron beamline was undertaken by SQUID vibrating source magnetometry. Measurements as a function of both temperature and applied magnetic field (up to 5 T) were performed. The resulting magnetic hysteresis loop for a film with an Mn concentration of 3.8% is displayed in Fig. 3.9(a), exhibiting a soft ferromagnetic behaviour with a coercive field of ∼36 mT at 5 K. The moment of these films is very small, and is dominated by the much larger volume of diamagnetic sapphire at high fields; as such, the loops shown are plotted with a linear subtraction based on a calibration measurement performed on a bare substrate. After this subtraction was performed, a strong paramagnetic-like contribution, which does not fully saturate within the instrumental limit of 5 T, necessitated higher fields to be used for further measurements. This behaviour matches previous studies on MBE-grown $Mn_xBi_{2-x}Se_3$, with the low coercivity and paramagnetic-like behaviour attributed to the continuous reorientation of magnetic domains within the applied field [89, 90].

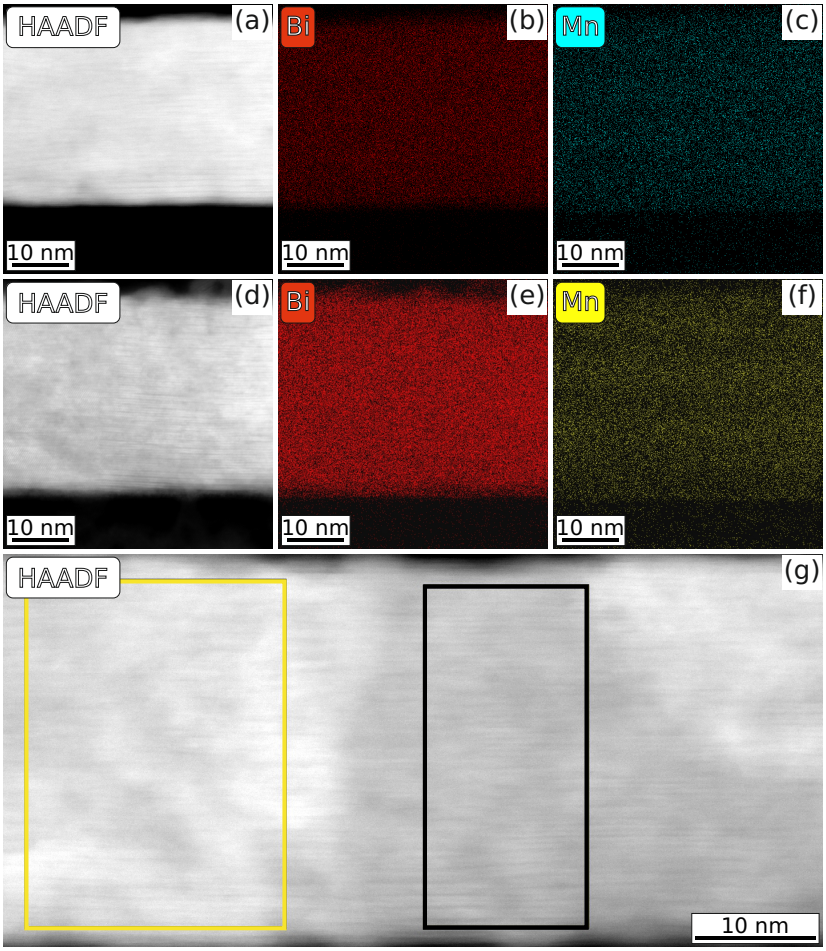


Figure 3.8: (a) HAADF-STEM image of a Bi_2Te_3 thin film doped with 1.6% Mn. Throughout the *c*-axis oriented layers, light and dark regions can be observed. As signal intensity is dependent on atomic number, this indicates compositional variation. (b,c) STEM EDS maps for Bi and Mn, respectively, from the same area as the HAADF image. (d) HAADF-STEM image of a Bi_2Te_3 thin film doped with 3.8% Mn. (e,f) EDS maps for the 3.8% Mn-doped sample for Bi and Mn, respectively. (g) HAADF image of a different area. While the EDS suggests that Bi and Mn are evenly distributed, a statistical analysis of the Mn peak intensities, normalised by the total spectral integral, shows that the lighter region, highlighted in yellow, contains 35% more Mn than the darker region (black rectangle). Figure adapted from Ref. [62] with data collected by B. Achinuq at the University of Manchester.

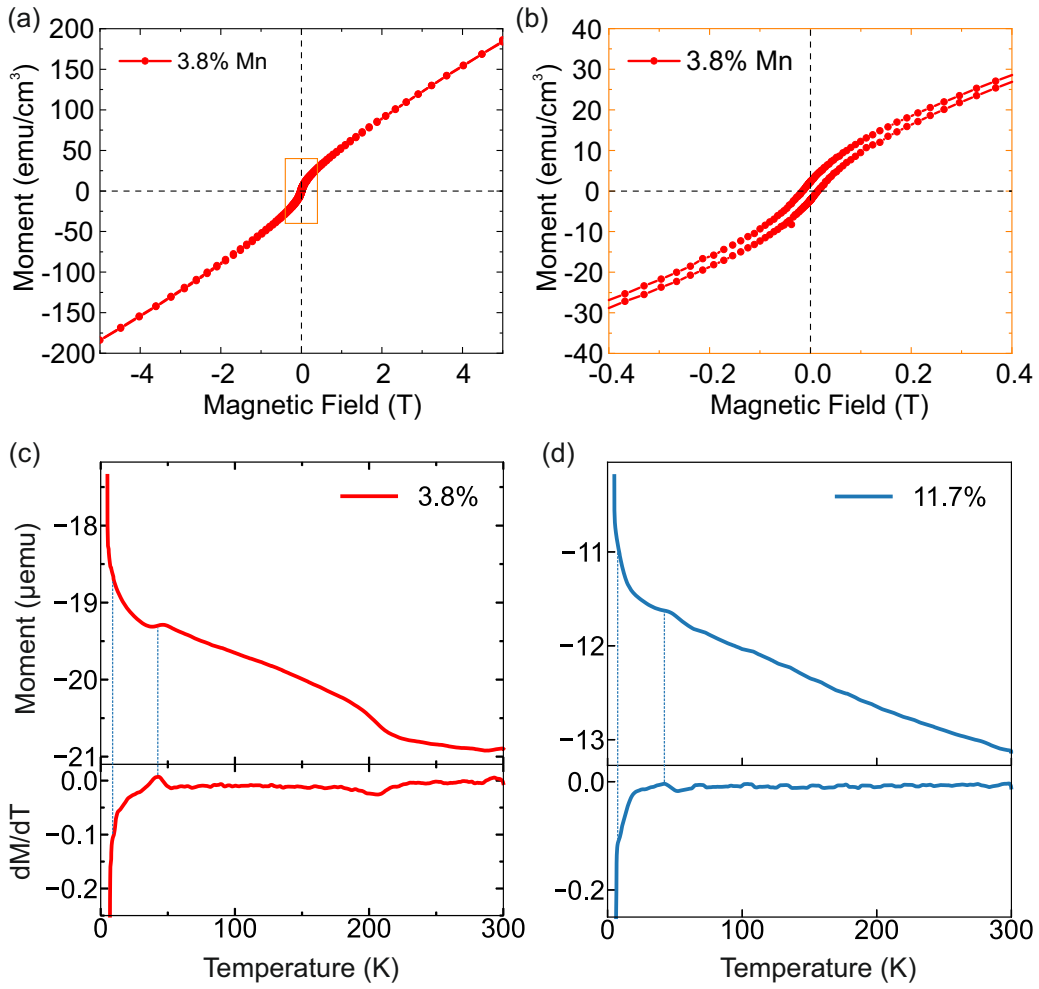


Figure 3.9: Magnetic characterisation of Mn:Bi_2Te_3 thin films, all films were cooled under zero field. (a) Magnetisation versus magnetic field of a sample with 3.8% Mn measured at 5 K. (b) Magnified view of the region in (a) highlighted in orange, showing low-field behaviour. The film shows a small coercivity and magnetic remanence of ∼36 mT and ∼2 emu/cm^3, respectively. (c,d) Temperature-dependent magnetisation for films with 3.8% and 11.7% Mn doping, respectively, with the derivative dM/dT shown below each plot. Transitions can be observed at 10 K and 43 K in the dM/dT (labelled for clarity), suggesting two magnetic phases are present in the films. This result is consistent with the structural analysis, with $MnTe_x$ contributing to the total magnetism of the film. Figure adapted from Ref. [62].

To determine the T_C of the films at different doping concentrations, $M(T)$ curves between 5 to 300 K were measured for two films with Mn concentrations between 3.8% and 11.7% and are shown in Fig. 3.9(c,d), respectively. First-order derivatives of these curves (plotted below the initial curves) reveal two magnetic transitions at ∼10 K and 43.3 K. When combined with the evidence of $MnTe_x$ phases shown in the XRD data, these transitions can be linked to Mn contributing to the overall magnetism of the film while being present in different environments within the film. The most likely scenario is that the lower temperature transition is the ferromagnetism in the substitutionally doped Mn in Bi_2Te_3 as this more closely mirrors the transition temperatures seen in previous work on MBE grown thin films [89, 90] and the higher temperature transition corresponds to the $MnTe_x$ phase [91].

Synchrotron-based XMCD was utilised to investigate the magnetic ground state of the series of doped Mn:Bi_2Te_3 films. The element specificity of XMCD can be used to isolate the contributions of Mn from the much larger diamagnetism of the substrate. Measurements were performed on the high-field magnet on the BLADE branch-line of I10 at the Diamond Light Source. Samples were measured at a base temperature of ∼2.5 K in magnetic fields up to 14 T, with the intention of allowing the sample to fully saturate. The films were oriented normal to the beam, therefore probing the out-of-plane, relative to the film's surface, component of the magnetic moments.

Figure 3.10(a) shows the XAS and XMCD spectra for a film with a 3.8% Mn concentration on the $L_{2,3}$ absorption edges. Pronounced dichroism can be observed, and Fig. 3.10(b) shows XMCD for multiple doping concentrations, all of which have similar dichroism spectra. However, it can be observed that as Mn concentration increases, the XMCD peak intensity decreases, indicating that not all the Mn ions are contributing

to ferromagnetic order. These ions will still contribute to the overall XAS intensity, resulting in a relative decrease in XMCD intensity.

This reduction in intensity was quantified by analysing peak asymmetry on the L_3 edge. Peak asymmetry is defined as the difference between XAS spectra divided by the sum at an absorption peak, and is proportional to the spin magnetic moment of Mn within the film [67, 72].

The asymmetry was calculated for five samples and plotted against Mn concentration in Fig. 3.10(d), showing a linear reduction in asymmetry with increasing Mn doping, with the asymmetry trending towards zero at higher doping concentrations. This graph can be fitted linearly in the form $A(x) = -0.163 + 0.0116x$, where x is the Mn concentration. Owing to the linearity between moment and asymmetry, the magnetic moment M per Mn atom normalised to equal 1 at $x = 0$ can be expressed as $M(x) = 1 - 0.0712x$.

Due to a photon energy-dependent background as well as L_3-L_2 peak overlap, using sum rule analysis to extract values for spin and orbital moments proved unreliable. This means that the proportionality between asymmetry and moment is the only means of estimating the average moment per Mn atom within the film. This was achieved by a comparison between real data and a calculated spectrum generated via multiplet calculations (details in [89]). The spectra for a hybridised ground state of a mixed d^4, d^5 and d^6 character yielding a moment of $4.75\,\mu_\mathrm{B}$/Mn at full saturation. This spectrum was scaled to be plotted alongside real data for a sample with a Mn concentration of 6% measured at 11 T and is shown in Fig. 3.10(e). It should be noted that the multiplet calculations are for Mn-doped Bi_2Se_3 films, with the difference in the 3rd peak of the L_3 edge being due to higher d^6 character in the Bi_2Te_3 films.

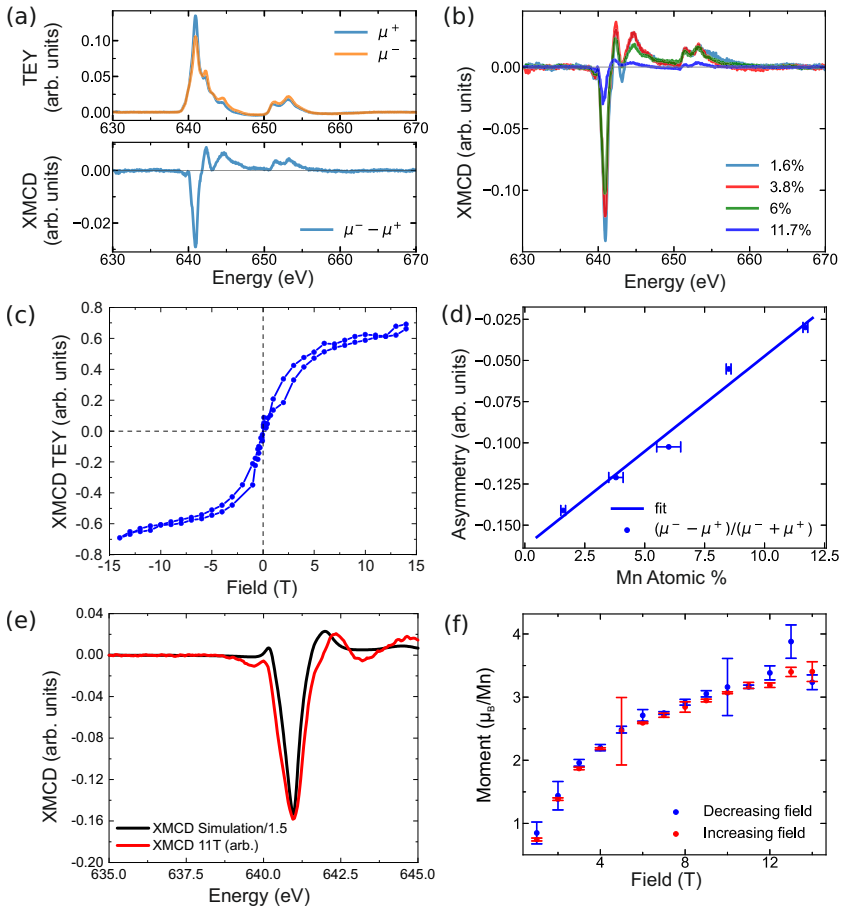


Figure 3.10: X-ray magnetic circular dichroism (XMCD) analysis of Mn:Bi_2Te_3 thin films. (a) XAS (top) and XMCD (bottom) spectra at the $L_{2,3}$ edges for a 3.8% doped sample at normal incidence under a 1 T field applied parallel to the beam, showing clear dichroism. (b) XMCD spectra for a series of doped samples, normalised by the maxima of the sum of the XAS spectra at the L_3 edge. (c) XMCD hysteresis curve for a Bi_2Te_3 doped with 6% Mn. (d) Plot of peak asymmetry versus atomic-% Mn, showing the reduction of moment with increasing Mn concentration as observed in (b). (e) XMCD spectrum at the L_3 edge under a 11 T field to ensure saturation. This is plotted alongside a simulated spectrum for $Mn_xBi_2Se_3$. (f) Magnetic moment per Mn atom as a function of applied field. These were calculated using the hysteresis data shown in (c) and scaled using the simulated spectra shown in (e). At saturation the moment is $(3.48\pm0.25)\,\mu_B$/Mn at a Mn concentration of 3.8%. Figure adapted from Ref. [62].

Scaling this model against the real data allows an estimate of the moment in the real data to be made. To complete this analysis, the field at which the film saturates had to be estimated. Figure 3.10(c) shows a hysteresis loop for a film containing 6% Mn. Upon first glance, it appears the film has not saturated; however, as TEY is dependent on the drain current off the holder, some field-dependent effects could be affecting the signal. Converting these values into asymmetry and later moment values via the scaling with the simulated data accounts for changes in XAS intensity and is shown in Fig. 3.10(f). It can be seen that the film saturates between 12 and 13 T, with a small plateau visible for at the two highest fields in the plot, enabling the analysis considered above to be conducted. Therefore, scaling against the simulated data, which by nature is for a saturated film, was performed using 13 and 14 T measurements from the upward and downward sweep of the hysteresis loop. Completing this analysis leads to a value of $(3.48 \pm 0.25)\,\mu_B$/Mn.

3.2.4 Discussion

The behaviour shown in the asymmetry data displayed in Fig. 3.10(d) with $M(x)$ reducing linearly with Mn concentration is unusual. Typically, $M(x)$ would remain constant until a critical level where all available Bi sites, linked to ferromagnetic behaviour, have been populated within the film. After this point, the moment per Mn atom will decrease as Mn begins to occupy energetically sub-optimal sites that associate with paramagnetic or even antiferromagnetic behaviour [15, 89, 90]. This implies that Mn exhibits a different behaviour.

There are several interdependent mechanisms to explain the decrease in $M(x)$, including substitutional doping, Mn clustering and secondary phase formation. At low concentrations, substitutional doping dominates, resulting in an increased ferromagnetic moment [14]. However, as x increases, Mn occupies other points in the lattice, such as

interstitial sites and van der Waals gaps, which is congruent with structural data such as the XRD and STEM discussed above (Figs 3.1 and 3.8). Mn atoms at these sites could couple antiferromagnetically with the substitutionally doped Mn, reducing the net moment. This behaviour is supported by theoretical predictions of coupling between Mn atoms in TIs [20]. In addition, as the Mn concentration increases, the increasing density of Mn ions enhances superexchange interactions, which could result in frustration effects, suppressing long-range magnetic ordering [31, 92].

Furthermore, as Mn concentrations go even higher, the increasing prevalence of secondary phases further complicates magnetic behaviour. Mn dopants may cluster or form secondary phases due to low mobility during growth, as observed in the STEM-HAADF and XRD data. Both Mn clustering and $MnTe_x$ can result in localised areas of antiferromagnetic or weak magnetic order that do not contribute to the overall ferromagnetic ordering.

Finally, strain-induced effects could play a role. Increasing Mn content could introduce local strain and disorder into the lattice, as indicated by the broadening of peaks in the RSM data in Fig. 3.3. Strain could alter the local magnetic exchange between ions and weaken ferromagnetic coupling within the lattice [90]. Additionally, Mn doping introduces charge carriers, probably holes, that can mediate the exchange interaction between Mn spins. Higher Mn concentrations, carrier-mediated interaction could transition to favour antiferromagnetic or spin-glass behaviour, once again suppressing ferromagnetic order [93].

As the lowest Mn content sample in Fig. 3.10(d) already aligns with the linear trend at higher concentrations, it suggests that substitutional doping may have saturated even at this low concentration. If available substitutional sites have been saturated at these

low concentrations, additional Mn atoms entering the lattice will only serve to weaken long-range ordering. As there is little evidence of a coherent secondary magnetic phase, this results in a linear reduction in moment as increasing Mn concentration only further disrupts ferromagnetic ordering without replacing it with any coherent phase of its own, as would be the case if crystalline MnTe were present, for example.

While MBE-grown samples can reach higher doping concentrations, sputtering may only permit this lower value due to the nanocrystalline nature of the film grown, combined with mobility limitations. This means that the Mn is unable to incorporate into the Bi_2Te_3 lattice completely, and secondary phases can be observed in XRD and STEM at a concentration of 1.6%.

These mechanisms can all explain the linear trend in $M(x)$ and are consistent with the structural findings; however, additional investigations are required to determine site-specific magnetic ordering and structural effects. While these fell outside the purview of this thesis, techniques such as neutron diffraction and more extensive electron microscopy could provide insight into Mn site preferences and coupling interactions. Additionally, TEM and X-ray photoelectron spectroscopy can be used in conjunction with other films to establish a limit for the substitutional doping of Mn. Understanding this limit could allow further optimisation and the reliable fabrication of thin films with minimised secondary phases.

3.3 Cr-doping of Nanocrystalline Sb_2Te_3 Thin Films

3.3.1 Growth of Cr-doped Thin Films

Cr-doped films were grown using the same co-sputtering method used in the previous Subsection 3.2.1, with a similar nucleation layer deposited followed by a main layer at a deposition rate of approximately $0.025\,\mathrm{nm\,s^{-1}\,W^{-1}}$. However, in this instance, the growth temperatures were adjusted for 175 °C for the nucleation layer and 240 °C for the main layer. This was done as higher growth temperatures yielded weaker crystallinity for undoped Sb_2Te_3. Once again, films of thickness ∼26 nm a 3-4 nm Al capping layer was deposited to prevent oxidation after the sample had cooled to room temperature.

#	**Sputter power (W)**		**Concentration (at. %)**		
	$P_{Sb_2Te_3}$	P_{Cr}	**Sb**	**Te**	**Cr**
463	30	4	39.3±0.4	55.4±0.7	5.3±1.0
464	30	6	39.2±0.4	54.8±0.7	6.0±0.9
467	10	3	37.2±1.0	52.5±1.1	10.5±2.0
468	10	2	35.9±0.4	48.5±0.7	15.6±0.8

Table 3.2: Table showing SEM-EDS analysis of a series of Cr-doped Sb_2Te_3. No reliable correlation between sputter powers and concentrations, suggesting uneven dopant distribution or variance in the growth modes. Table adapted from Ref. [94].

Here, due to the high growth rates of Sb_2Te_3 and issues with running the Cr target at high power, the TI was varied on growth rate to allow for a wide range of doping concentrations. A list of samples, their sputter target powers, and elemental composition (determined by SEM-EDS) is shown in Table 3.2.

It can be seen from Table 3.2 that there is no simple relationship between the ratio of the sputter powers and composition. This can be attributed to particular ratios and growth rates encouraging specific growth modes or the uneven distribution of the dopant,

although the risk of this affecting the measurement is minimised by averaging the EDS results across multiple sites. Despite this, the results of the growth series are a set of films with varying doping concentrations, allowing the exploration of the dopant's effect on structural and magnetic order.

3.3.2 Structural Characterisation of Cr:Sb_2Te_3 Films

Structural properties of the doping series were characterised using XRD in three measurement geometries: symmetric $\theta - 2\theta$, asymmetric-RSM, and pole figures. Symmetric $\theta - 2\theta$ scans are shown in Fig. 3.11 with films labelled by their nominal Cr concentration determined by SEM-EDS. At low Cr concentrations, $(00\underline{3}\underline{l})$ diffraction peaks can be clearly seen at 8°, 18°, and 26°, showing c-axis orientated Sb_2Te_3. However, as Cr content increases, this structure begins to break down above approximately 10%, with the c-plane peaks disappearing and being replaced by a film with seemingly no preferred crystalline axis. In this state, weak features suggestive of Cr/Te-rich phases can be observed, indicating a shift in crystalline structure. The c-lattice parameters were extracted from the data using Bragg fits for the (003), (006), and (009) peaks, averaging across the peaks to reduce error. Starting from the value of $c = (31.4 \pm 0.1)$ Å for the undoped film, the c lattice parameter shifts to (30.6 ± 0.1) Å for 5.3% Cr and (30.9 ± 0.1) Å for 6.0% Cr. This reduction in lattice parameter over the undoped film is expected to be due to the smaller atomic radius of Cr. However, the small increase from 5.3% to 6.0% is unusual and could be caused by the additional dopant inducing more stacking faults or differences in Cr site distribution, which increase the lattice parameter. It should be noted that the calculated c value for the undoped film is not a match for bulk values in literature, with the cause probably due to the lattice mismatch between Al_2O_3 and Sb_2Te_3 [95].

To explore the X-ray diffraction from the film more completely, asymmetric RSMs

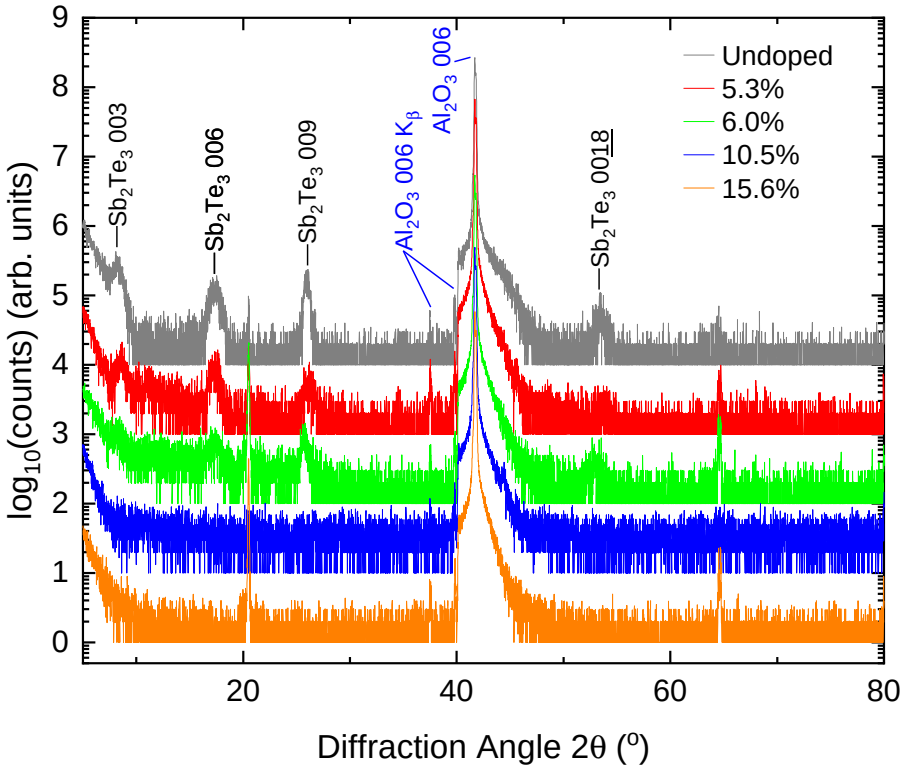


Figure 3.11: Out-of-plane XRD patterns measured in symmetric (θ-2θ) geometry of a series of Cr-doped Sb_2Te_3 films, plotted on a logarithmic intensity scale and vertically offset for clarity. Diffraction peaks for Sb_2Te_3 ($003\underline{l}$) for $l = 1, 2, 3, 6$ can be clearly seen for the undoped film up to a Cr concentration of 6%, indicative of c-axis growth. At 10% Cr, these peaks are no longer visible, suggesting a breakdown of defined out-of-plane crystallinity. Figure taken from Ref. [94].

were used to investigate off-axis growth and the weak features at high Cr concentrations. Asymmetric RSMs for the undoped, 5.3%, 10.6%, and 15.6% films are shown in Fig. 3.12. The undoped, 5.3% and 10.6% samples exhibit Sb_2Te_3 peaks, consistent with the c-axis domains seen in symmetric XRD. Conversely, the 15.6% sample only shows diffraction peaks from CrTe and Cr_2Te_3, showing secondary phase formation and a breakdown in the tetradymite host structure at high Cr concentrations. It should also be noted that

while Sb_2Te_3 peaks can be seen in the 10.6% peaks, there are no such peaks visible in the $\theta - 2\theta$ measurements. This is due to the relatively low intensity of the $(003\underline{l})$ peaks when compared to the off-axis diffraction peaks, in this instance allowing the RSM measurements to act as a more sensitive probe of crystalline order. Combining these two measurement techniques, we can infer a gradual breakdown of order with increasing Cr concentration, resulting in a complete breakdown above ∼10% and a switch to a $CrTe/Cr_2Te_3$ dominant phase.

To understand the structural changes as Cr concentration moves from the mid- to high-doping regime, HAADF-STEM measurements were taken by J. C. A. do Nascimento, C. Murrill, and V. K. Lazarov at the University of York. Figure 3.13(a,b) shows HAADF-STEM of a 5.3% Cr film, showing a nanocrystalline quality with near parallel lattice fringes, supporting the evidence of *c*-axis oriented quintuple layers from the XRD data. However, frequent tilts and stacking faults can be seen, showing significant disorder on a 5-10 nm length scale. At 10.5%, Fig. 3.14(c,d), displays a loss in long-range layered order with large amorphous regions, once again supporting the loss in order seen in the XRD pattern.

To try and gain insight into the mechanism behind this breakdown in order, STEM-EDS maps shown in Fig. 3.14 were taken. These results reveal significant spatial inhomogeneity in the dopant distribution. In the 5.3% film [Fig. 3.14(a,c,e,g,i)], a narrow Cr-enriched band is present ∼10 nm below the surface, which coincides with a local depletion of Sb. As Te remains comparatively uniform, it is highly likely that this region contains Cr_xTe_y phases. However, the 10.5% sample [Fig. 3.14(b,d,f,h,j)], does not have a Cr-rich band, instead containing more diffuse fluctuations in composition over the film's thickness, consistent with the amorphous HAADF data. A mild shift in the Sb:Te ratio

is observed near the surface, which, based on the HAADF data, appears likely to be due to surface chemistry and post-growth relaxation.

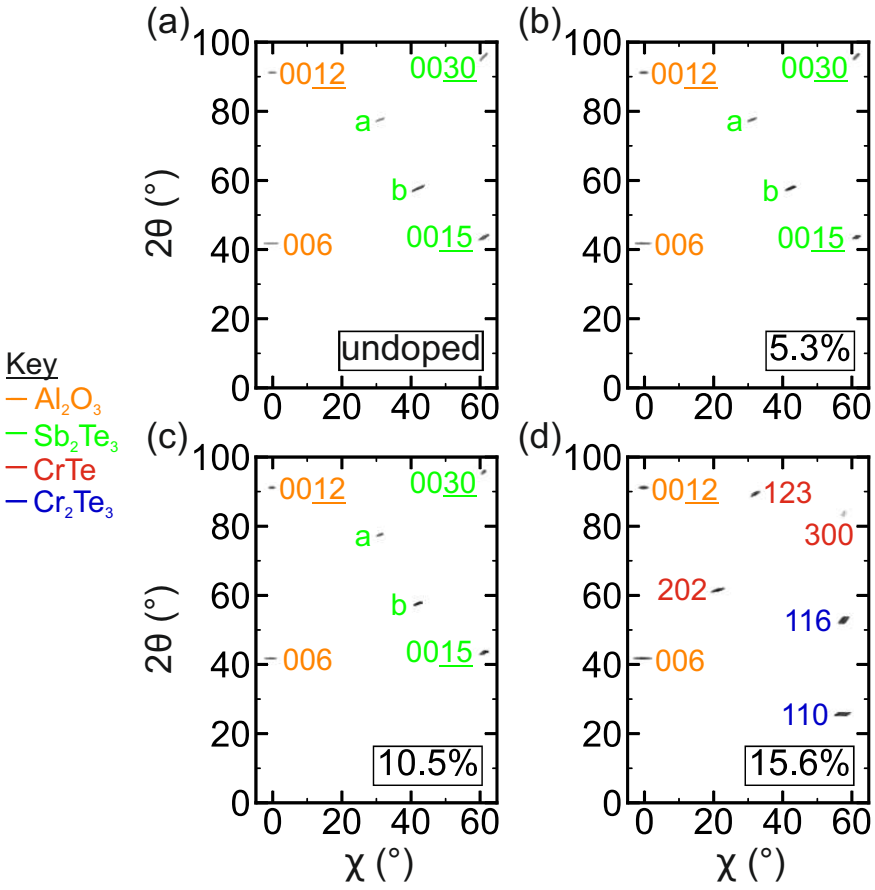


Figure 3.12: Asymmetric RSMs (2θ-χ) for selected samples from the Cr-doping series: (a) undoped, (b) 5.3%, (c) 10.5%, and (d) 15.6%. (a-c) Show Al_2O_3 and Sb_2Te_3 peaks, with the 15.6% film in (d) showing no Sb_2Te_3 peaks. Instead, the peaks shown in (d) are consistent with CrTe and Cr_2Te_3, implying the formation of a secondary phase that contributes to the structural breakdown of the Sb_2Te_3 phase. The peaks labelled a and b can be indexed with Sb_2Te_3 peaks $(\bar{1}\bar{1}\underline{2}0)$ or $(1\bar{2}\underline{2}0)$ and $(\bar{1}\bar{1}\underline{1}3)$ or $(1\bar{2}\underline{1}3)$, respectively. Peaks marked with an asterisk are attributed to their equivalent c-axis orientated columnar domains with a $\sim 60°$ rotation from the surface normal. Figure adapted from Ref. [94].

In summary, the STEM and XRD data suggest that at low-to-mid doping concentrations, a layered order is formed, but with local compositional discrepancies. Whereas high doping results in high structural disorder and the formation of secondary phases.

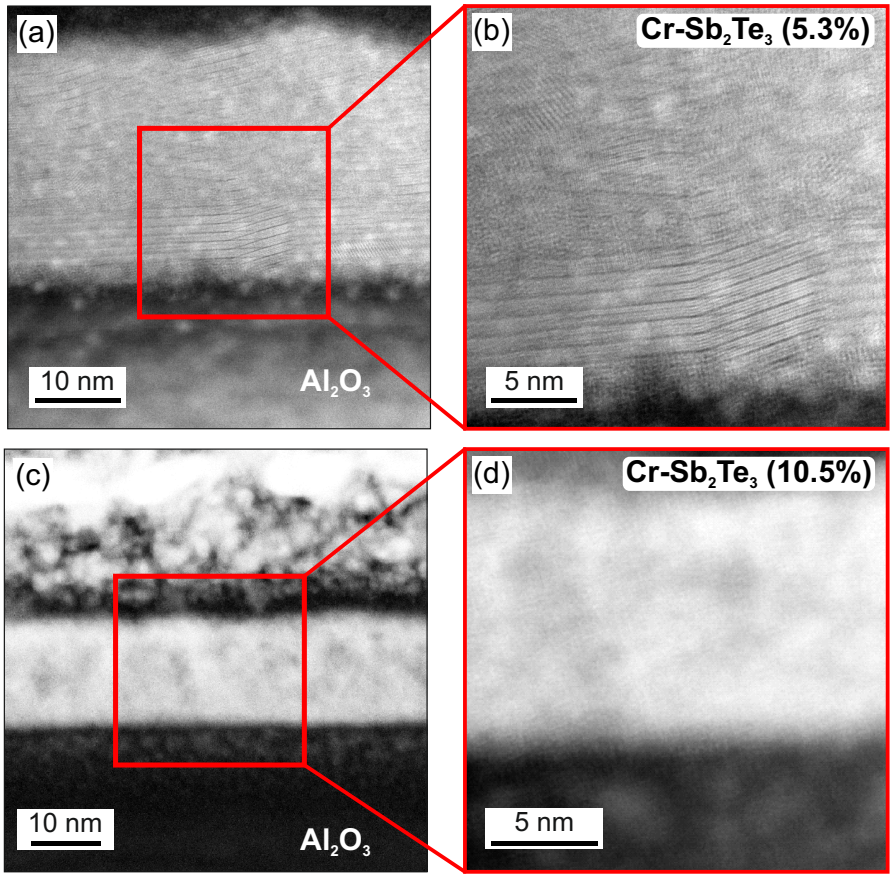


Figure 3.13: Cross-sectional HAADF-STEM of Cr-doped Sb_2Te_3 films. (a,b) Shows a film with 5.3% Cr concentration with parallel lattice fringes indicative of quintuple layers orientated with the *c*-axis. Local defects can also be observed, consistent with the presence of nanocrystalline domains. (c,d) The 10.5% Cr film shows no visible layering, suggesting a breakdown in the stacking that is visible at lower Cr concentrations. Figure adapted from Ref. [94].

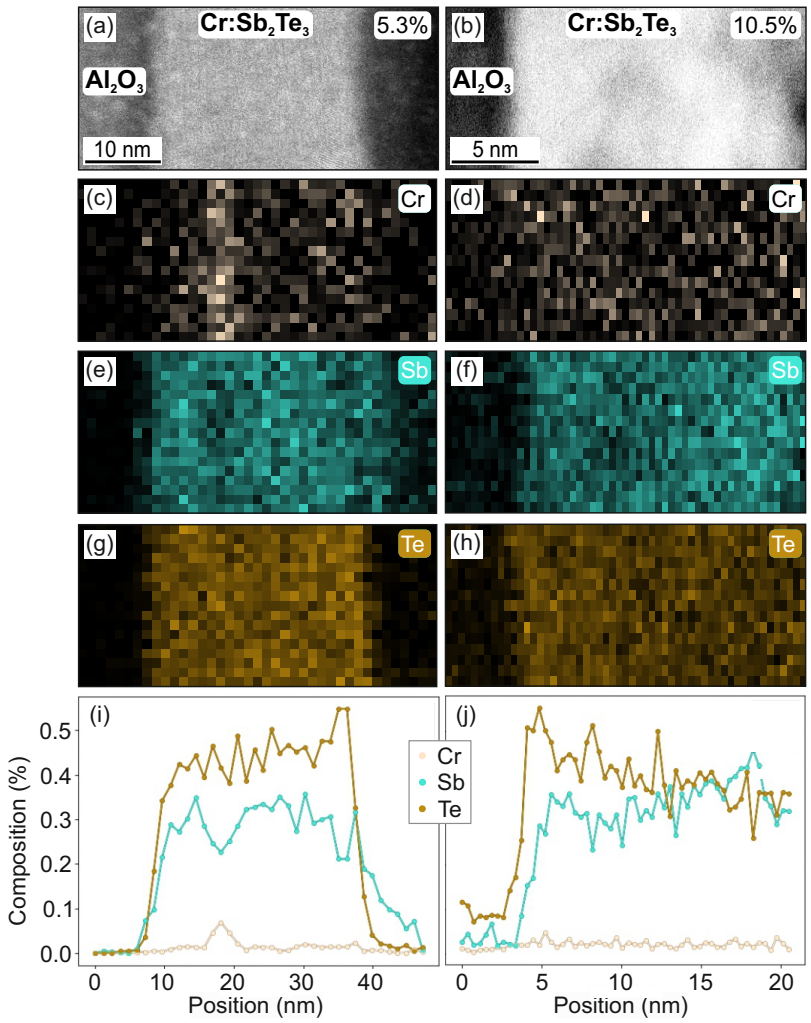


Figure 3.14: Cross-sectional STEM and STEM-EDS of the films shown in Fig. 3.13. (a,b) STEM images of the 5.3% and 10.5% films, respectively. (c,e,g) Elemental EDS maps of the 5.3% films showing Cr, Sb, and Te, respectively. A narrow region of increased Cr concentration is visible, accompanied by a coincident reduction in Sb and a relatively uniform distribution of Te. (d,f,h) Corresponding EDS maps for the 10.5% sample, showing a more uniform composition, matching the reduced layering seen in the HAADF images of the film. (i,j) Line profiles of the relative composition extracted across the mapped areas for the 5.3% and 10.5% films. Figure taken from Ref. [94].

Crystalline Orientation Variation in Sb_2Te_3 Film Deposition

While exploring the structural properties of the film, some structural abnormalities were observed in both doped and undoped films. The 6% Cr film, which displayed a 'normal' Sb_2Te_3 diffraction pattern in Fig. 3.11, displays different RSM peaks, shown in Fig. 3.15. This is not an effect due to the dopant, as another undoped Sb_2Te_3 film grown under the same conditions as the pure Sb_2Te_3 film shown in Fig. 3.12 also shows a matching pattern.

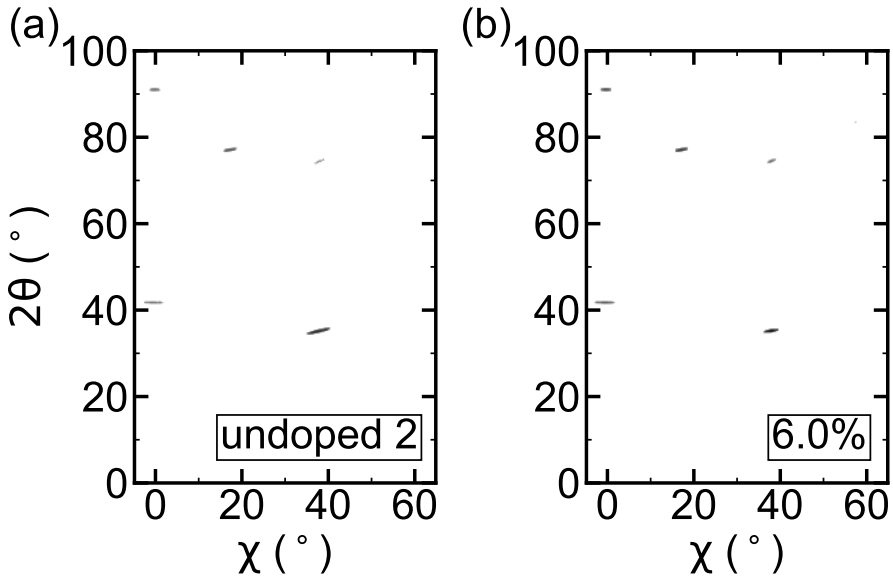


Figure 3.15: Asymmetric RSMs for two samples exhibiting structural abnormalities. (a) Shows an undoped sample, different to the film shown in Fig. 3.12. This indicates that the defect is not due to doping. (b) A 6% Cr sample displaying the same peaks as the undoped sample in (a) These irregular patterns are attributed to a rotation of the crystal structure during growth, and the peaks have been left unlabelled due to the unknown nature of this rotation.

This was further investigated by performing pole figures, i.e. rotational scans across a range of tilts perpendicular to the beam plane, around representative peaks in two

undoped samples, one displaying the anomalous RSM pattern and one with the usual pattern. These results are shown in Fig. 3.16 and show the 'normal' sample displaying a sixfold rotational symmetry originating at 0°. However, the abnormal sample is more complex, with one of the peaks displaying 6-fold symmetry, offset by 30° when compared to the standard sample, while the other peak shows threefold symmetry. The varying symmetry, combined with the unusual reciprocal space maps, and XRD results yielding expected outcomes, as seen in Fig. 3.11, suggest that the films displaying these characteristics have grown with a crystalline rotation or a unique stacking. As the films were grown under identical conditions, it is likely that the *c*-axis orientated growth mode is extremely sensitive to small variations in parameters such as substrate temperature or preparation.

To fully understand this anomaly and determine if it has any effect on the film's properties, an in-depth TEM study would be required. This fell outside the scope of this thesis due to the availability of facilities, so this conclusion will suffice for the remainder of the analysis in this chapter.

3.3.3 Magnetic Measurements of Cr:Sb_2Te_3 Thin Films

SQUID magnetometry of the 6% Cr film, shown in Fig. 3.17, shows soft ferromagnetism at 5 K with a small coercivity and an unsaturated loop up to 1 T. In addition, $M(T)$ and its associated dM/dT displayed in the figure show two weak anomalies at ∼38 K and 82 K, suggesting two magnetic transitions, potentially due to CrTe/Cr_2Te_3 secondary phases or dopants at multiple lattice sites exhibiting different magnetic behaviours. Previous studies of epitaxial films reported a T_C of ∼12.5 K, a coercive field of 10 mT, and effective moments of $\sim 2\mu_B$/Cr using bulk magnetometry [95].

Synchrotron X-ray magnetic spectroscopy at the Cr $L_{2,3}$ edges, shown in Fig. 3.18,

reveal depth-dependent dichroism. The detection methods used yield different results, with the surface-sensitive TEY, which has a penetration depth of ∼3-5 nm, differing from the bulk-sensitive FY. Two peaks at the L_3 edge in the TEY suggest two valencies for Cr,

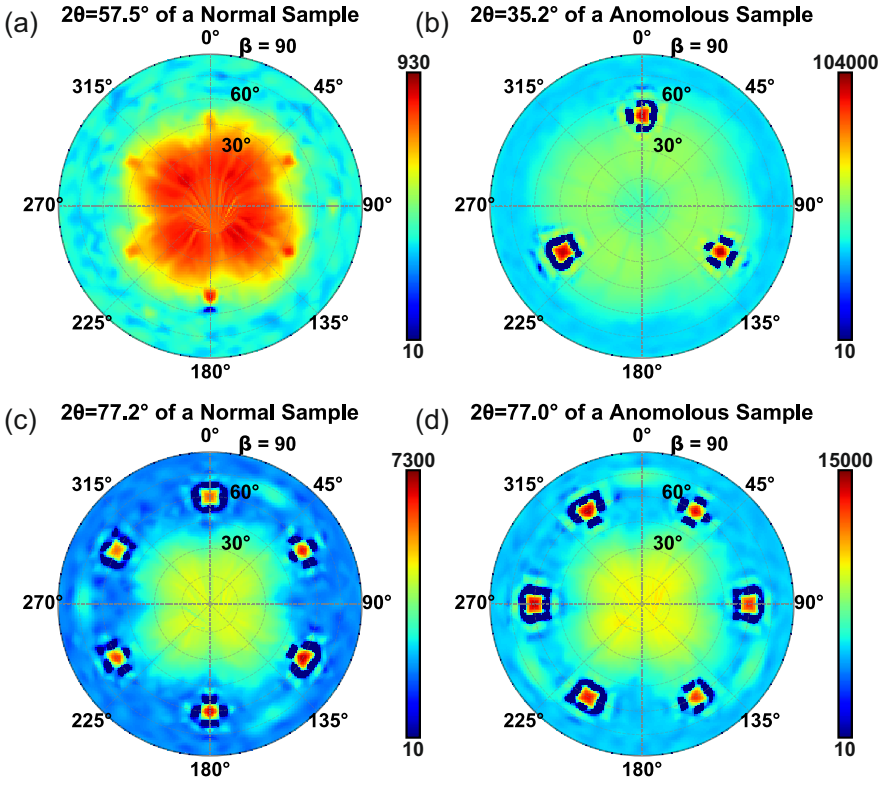


Figure 3.16: Pole figures around selected peaks for the normal and anomalous undoped Sb_2Te_3 films, with the peaks labelled by their 2θ values on the RSMs shown in Figs. 3.12 and 3.15. (a,c) Shows the sample with the normal orientation, with both peaks showing a sixfold rotational symmetry. (b,d) Peaks of the film with the anomalous RSM, showing a threefold symmetry for the $2\theta = 35.2°$ peak and sixfold symmetry for the $2\theta = 77.0°$ peak, highlighting the difference in the peaks and the assumed crystal orientation or stacking. It should be noted that the significant variation in plot intensities is due to both the structural differences between the films and the difficulty in aligning the 2D detector. Therefore, the plots were normalised separately to allow for a better comparison of the features.

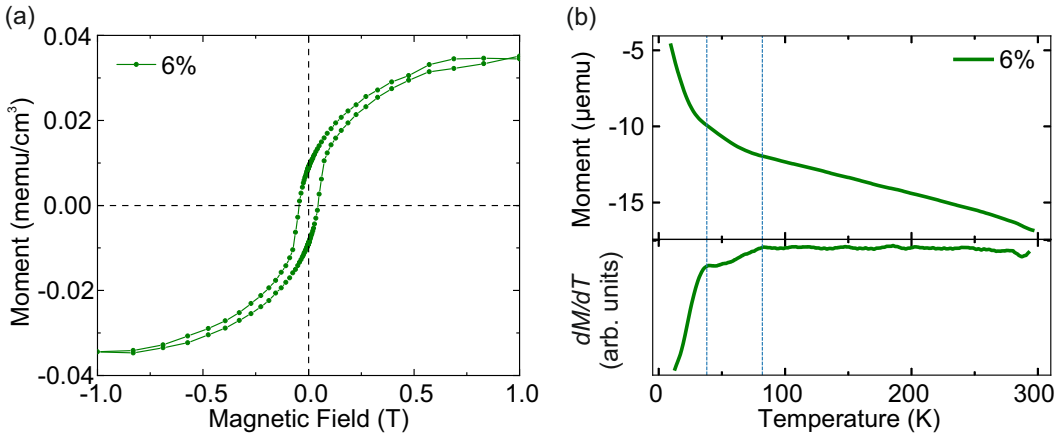


Figure 3.17: SQUID-VSM measurements of a film with a 6% Cr concentration. (a) $M(H)$ loop showing a narrow open loop at a temperature of 5 T, with the loop not completely saturating at 1 T. (b) Temperature-dependent plots of the same sample, with an additional panel showing the first derivative dM/dT. This makes the two discontinuities, marked using blue dotted lines, at 38 and 82 K, easier to identify, suggesting two magnetic phases are present within the film. Figure taken from Ref. [94].

Cr^{2+} and Cr^{3+}, whereas the FY shows lower-energy features suggestive of only a Cr^{2+} character. These labels can be assigned as more electropositive ions absorb at higher photon energy, so the lower-energy peak implies a weighting towards the divalent state in the bulk.

Applying sum rules to the TEY data (discussed in 2.3.2) using a *jj*-mixing correction of $C = 2.0 \pm 0.2$ [95], yields a orbital moment of $m_L = (0.20 \pm 0.04)\,\mu_B$/Cr and a spin moment of $m_S = (1.6 \pm 0.2)\,\mu_B$/Cr. This correction of $C = 2.0 \pm 0.2$ was taken from multiplet calculations performed by Figueroa *et al.* [95]. The spectra and integrals for sum rules are shown in Fig. 3.19. It is important to note that, as is common in Te-based TIs, the background from the Te $M_{4,5}$ edges complicates normalisation.

Additionally, as the applied field was limited to 3 T, below the ∼7 T required to saturate the TEY response in similar films (Cr-doped Bi_2Se_3) [95], these calculated

values, particularly m_S, will be underestimates of their full values. Figueroa *et al.*, reported values of $m_S = (2.90 \pm 0.30)\,\mu_B/\mathrm{Cr}$ and an extremely low orbital moment of $m_L = (0.04 \pm 0.10)\,\mu_B/\mathrm{Cr}$ [95]. They followed these measurements by decomposing the spectra into bulk and surface components using multiplet structure simulations [71], resulting in $m_S \approx 3.64\,\mu_B/\mathrm{Cr}$ for the bulk states and $\sim$1.91 μ_B/Cr for surface states (with a weighted average of $\sim$2.84 μ_B/Cr). This contrasts with the results presented here, which show a reduced spin moment and a larger orbital moment. Plausible causes of this include incomplete magnetic saturation, a higher weight of Cr^{3+}, which has a smaller m_S, or normalisation choices that bias the sum rules integrals. It should be noted that the *jj*-mixing correction has uncertainty, with a value of $C = 2.0 \pm 0.2$, which propagates into the uncertainty in m_S. Finally, reduced Cr-moments of $\sim 2\mu_B$ have been reported in bulk magnetometry on similar films [95], showing our results are not unprecedented in this family of materials.

The presence of both Cr^{3+} and Cr^{2+} components is consistent with the covalent bonding in chalcogenides, where mixed valence is driven by hybridisation and local bonding, without changing free-carrier density. X-ray dichroism measurements in previous work show hysteresis loops with moments only saturating at high fields, $\sim$7 T for TEY and $\sim$3 T for FY, highlighting the depth-dependent magnetism [95]. It should be noted that due to the self-absorption of emitted photons, quantitative analysis of the FY spectrum is not possible, preventing a more complex analysis of how the moment changes on the sample surface compared to the bulk.

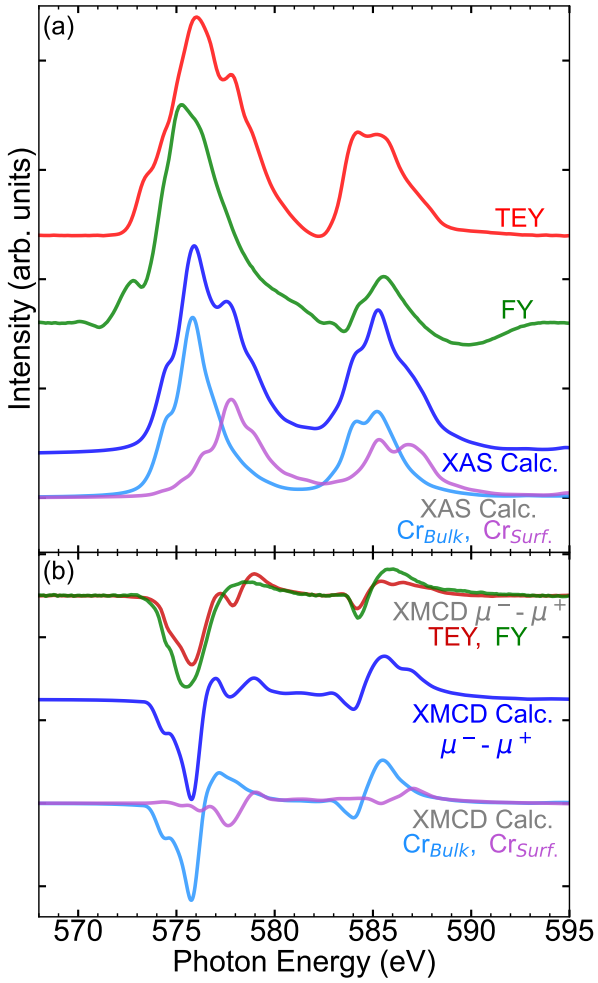


Figure 3.18: XAS and XMCD spectra for a sample with a nominal Cr concentration of 6% measured at 3 T at a temperature of 2.5 K. (a) XAS acquired by both surface-sensitive TEY (red) and bulk-sensitive FY (green), displayed alongside calculated bulk (light-blue) and surface-oxidised (purple) spectra. These calculated spectra were combined into a total calculated XAS (blue). (b) XMCD plots ($\mu^- - \mu^+$) of the same measured and calculated spectra utilising the same colour scheme as above. The TEY spectra have a second feature at ~2 eV higher energy than the main L_3 peak, consistent with surface oxidation, whereas the FY exhibits a more expected bulk response. Figure taken from Ref. [94].

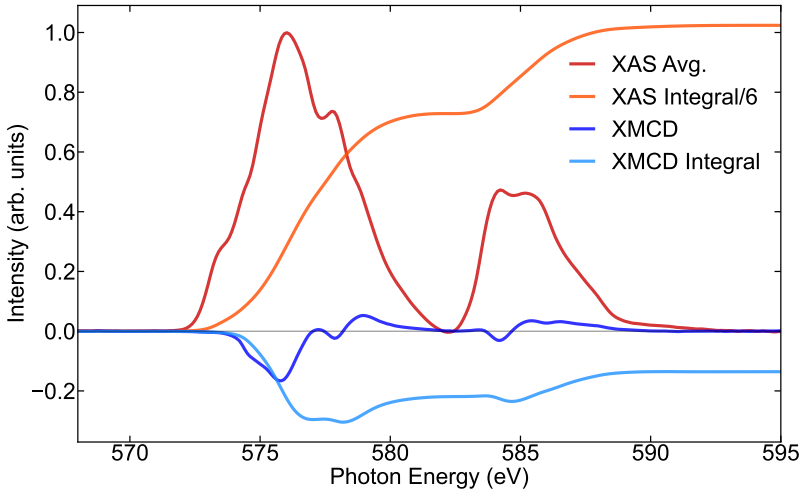


Figure 3.19: Cr $L_{2,3}$ TEY XAS/XMCD used for sum-rule analysis. The helicity-averaged XAS is displayed alongside its energy integral (which is scaled at 1/6 for visual clarity). This is plotted with the XMCD and its energy integral. These integrated areas define the three integrals (XAS over $L_{2,3}$, XMCD over $L_{2,3}$, and XMCD L_3) needed to obtained m_L and m_S via sum rules. For Cr, a jj-mixing correction factor of $C \approx 2.0$ needs to be applied when calculating m_S. It should be noted that due to self-absorption/saturation distorting the $L_{2/3}$ ratio, FY can only be used qualitatively; therefore, TEY is the only dataset available for this analysis. Figure adapted from Ref. [94].

The existence of two valencies with different magnetic properties, combined with the lack of secondary phases in the XRD and RSM data, suggests that the two transitions seen in Fig. 3.17(b) are not due to crystalline impurity. This is supported by existing literature, which found films of high structural quality without parasitic phases, attributed magnetic behaviour to Cr occupying octahedral substitutional sites holding a predominantly divalent character, with the surface containing more trivalent ions [95]. Combining these points supports the interpretation that the localised variations in bonding/valence of

Cr result in the presence of multiple magnetic components, accounting for both the broadened $M(H)$ and two transitions in $M(T)$.

3.3.4 Discussion

This section has demonstrated that, within a limited solubility range, Cr doping is feasible. Symmetric $\theta - 2\theta$ scans and asymmetric RSMs show that doping preserves the Sb_2Te_3 quintuple layer structure up to a Cr concentration of 10%, while higher concentrations lead to the emergence of CrTe and Cr_2Te_3 peaks. STEM measurements reveal layered morphology with a defect density consistent with nanocrystalline character at low Cr concentrations. This includes a narrow Cr-enriched band combined with localised Sb depletion. At higher Cr concentrations, a loss of this layered structure and a more diffuse composition is observed. Adding to the structural complexities, an orientation shift will occur during growth, seemingly unaffected by the presence of the dopant, seen in asymmetric RSM. The exact nature and mechanism of this growth mode are unknown, and an extensive TEM study is needed to understand the effect fully. Element-specific XAS/XMCD displays a depth-dependent magnetic response, with predominantly Cr^{3+} character at the surface and Cr^{2+} in the bulk. Sum rules analysis was performed, yielding finite orbital and reduced spin moments. These results are only partial moments, as the film is not fully saturated at the 3 T measurement field, which underestimates m_S in particular. Combining the structural and magnetic data, a growth window for sputter Cr-doped Sb_2Te_3 has been established, with the key challenges being the suppression of secondary phases, controlling the orientation of the base Sb_2Te_3 lattice, and managing localised composition variations.

Chapter 4

Growth and Characterisation of the Intrinsic Mangetic Topological Insulator $MnBi_2Te_4$

4.1 Motivation

The previous chapter found that when Bi_2Te_3 is doped with Mn in quantities above 10%, $MnBi_2Te_4$ begins to form. Building upon this observation, this chapter will explain the unique properties of this material, detail efforts to optimise its growth, and explore the magnetic properties of $MnBi_2Te_4$ thin films with different compositions.

The $MnBi_2Te_4$ (MBT), and associated family of materials, incorporates the transition metal dopant directly into the lattice, known as an intrinsic magnetic topological insulator [96–102]. $MnBi_2Te_4$ was the first of such materials to be realised [97, 103] and consists of septuple layers (SLs) with a Te-Bi-Te-Mn-Te-Bi-Te stacking structure. This SL structure has ferromagnetic ordering within each SL layer and antiferromagnetic coupling between SL layers, making MBT an A-type antiferromagnet. The magnetic ordering breaks time-reversal symmetry, but it exhibits more interesting topological phases depending on different stacking configurations and the number of SLs. Firstly, it has been shown that

the intercalation of additional magnetic layers, such as MnTe, into the lattice can alter the magnetic properties. The resulting $(MnBi_2Te_4)(MnTe)_m$ superlattices can exhibit a reduced antiferromagnetic phase due to the disruption of the exchange interactions between SLs [104]. The thickness of the film can also affect its properties. Owing to the alternating spin orientation of septuple layers, shown in Fig. 4.1, whether the film is fully compensated or has a single uncompensated magnetic layer depends on the number of SLs. An odd number of layers results in a net uncompensated magnetisation that supports the QAHE [105, 106], where an even number results in a zero Hall plateau characteristic of an axion insulator state [105, 107, 108]. Finally, MBT heterostructures have been linked to the observation of Majorana fermions through topological superconductivity [109].

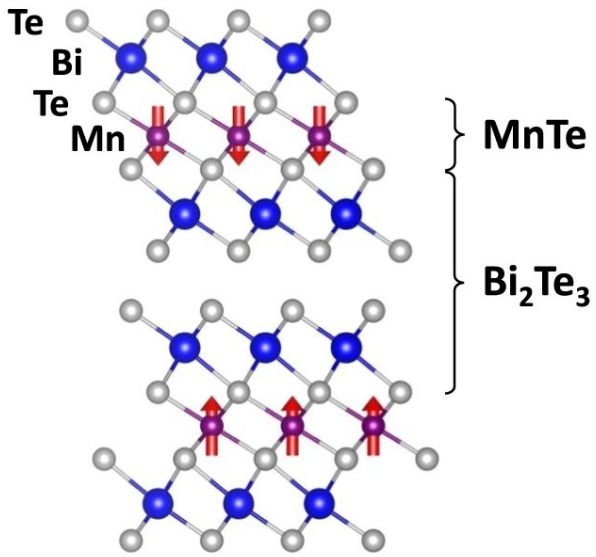


Figure 4.1: Diagram showing the lattice structure and A-type antiferromagnetism in $MnBi_2Te_4$. Figure taken from Ref. [110].

These topological states have driven interest in these films, and the results shown in Subsection 3.2.2 demonstrate that at higher Mn-doping levels, the spontaneous formation

of an MBT phase occurs. MBT thin films have primarily been produced using MBE, which enables the atomically precise control of layers to ensure the correct formation of the SL structure. However, despite the high purity of these growths, there have been difficulties in observing the key phenomena listed above, with no experiment at time of writing conclusively measuring the QAHE or axion insulator states in thin films, with the best results seen in single crystals. In addition to this, the surface roughness inherent to the step-flow morphology of MBE growth makes measuring antiferromagnetism using element-specific X-ray spectroscopy difficult, as the roughness leads to an uneven number of SLs across the X-ray spot size. The alternating odd-even septuple layer numbers result in alternating magnetic polarisations across the surface, leading to the averaging out of the signal, particularly in linear dichroism.

Magnetron sputtering offers an alternative approach, enabling smoother surface morphologies through the control of the kinetic energy of sputtered particles and post-growth annealing. This has recently been demonstrated, with indicators of antiferromagnetic order measured in sputtered $MnBi_2Te_4$ thin films [87]. While these results are positive, detailed phase analysis and element-specific spectroscopy are absent, leaving room for further study.

In an attempt to add these measurements to the literature for $MnBi_2Te_4$, structural and magnetic properties of films grown by magnetron sputtering are studied in the following chapter. The role of annealing temperature and sputter power ratios in determining phase purity is explored using a variety of X-ray diffraction, electron microscopy and AFM measurements. In addition, the effects of phase and stoichiometry on magnetic response are measured using VSM-SQUID magnetometry and XMCD/XMLD (at the $L_{2,3}$ edges).

4.2 Growth of $MnBi_2Te_4$ Thin Films

Thin films of $MnBi_2Te_4$ were synthesised by co-sputtering Bi_2Te_3, Mn and Te at room temperature; using sputter power to tune the fluxes from each target enabled the adjustment of stoichiometry. A post-growth anneal at 375 °C for 3 hours was then used to ensure crystallinity in the film. Unlike the rest of the thesis, optimising growth for nano-crystalline structures is not the priority in this chapter, due to the limited literature available for this material; the successful growth using sputtering is the main objective of this work.

After being left to cool to room temperature, the sample was transferred to the expansion chamber shown in Fig. 2.1 (Section 2.1) and a 3-4 nm layer of Al deposited to protect the film against oxidation. A series of samples with varying stoichiometry was produced using different ratios of sputtering powers between the three targets. To ensure the thickness dependent properties of the film remain constant while exploring the effects different compositions, most films grown have the same thickness of ∼12 nm. These films were then evaluated both structurally and compositionally to find the conditions that lead to near-stoichiometric MBT.

Table 4.1 shows the ratios of sputter powers and the resulting atomic compositions measured by SEM-EDS. For the remainder of this chapter, two representative samples will be compared: a near-stoichiometric $MnBi_2Te_4$ film—hereafter sMBT—and a Mn-rich sample named eMBT. These films are labelled in table 4.1, and were both produced using the co-sputtering and annealing method described above.

It can be seen that there is a clear nonlinearity between the Mn sputter power and concentration, with an apparent dependence on the Te flux. This shows that despite constant Mn sputter power, an increase in Te flux from 5 to 8 W results in an increase

#	Sputter power (W)			Concentration (at. %)		
	$P_{Bi_2Te_3}$	P_{Mn}	P_{Te}	Bi	Te	Mn
576 (eMBT)	20	10	5	18.7±2.4	49.2±2.0	32.2±1.0
584	20	10	5	29.2±0.5	46.1±1.9	25.0±2.4
586 (sMBT)	20	4	5	36.5±1.5	50.0±1.9	13.5±2.5
589	20	4	8	34.5±2.2	51.8±1.5	13.6±3.2
593	20	4	8	32.5±0.6	52.2±0.9	15.3±1.0

Table 4.1: Sputter powers and elemental composition of selected ∼12 nm-thick $MnBi_2Te_4$ films, measured by SEM-EDS. The samples, named eMBT (Mn-rich) and sMBT (stoichiometric), are the focus of the following sub-chapters. Non-linear dependence between Mn concentration and Mn sputter power is observed, with Te flux seemingly acting as a controlling variable. Table taken from Ref. [111].

in Mn concentration. This indicates that, similarly to the Mn-doped Bi_2Te_3 films in Chapter 3, excess Mn can cluster and form secondary phases rather than incorporate into the lattice uniformly [62], with excess chalcogen encouraging the growth of $MnTe_x$ clusters within the film.

The following section shows that films with Mn concentrations greater than 20 at.% (atomic-%) exhibit significantly different crystallographic structures compared to samples of relatively similar stoichiometry. This suggests that there is a threshold, above which the $MnBi_2Te_4$ phase becomes unstable and reverts to a structure more similar to Bi_2Te_3, where Mn may separate from the $MnBi_2Te_4$ structure, effectively leaching Mn away from the intrinsic magnetic TI.

4.3 Structural Analysis

To assess crystallinity, X-ray diffraction patterns were taken in several measurement geometries, with symmetric $\theta - 2\theta$ and φ scans shown in Fig. 4.2 and asymmetric RSM shown in Fig. 4.3. Symmetric scans show $(00\underline{3}\underline{l})$ peaks in both samples, demonstrating

c-axis-orientated growth. The primary diffraction peaks (009) occur around 20°, with c-lattice parameters calculated as (41.6±0.1) Å and (42.2±0.1) Å for eMBT and sMBT, respectively. These are both larger than the bulk value of 40.9 Å, which can be attributed to intercalation in the van der Waals gap between septuple layers and epitaxial strain from the Al_2O_3 substrate.

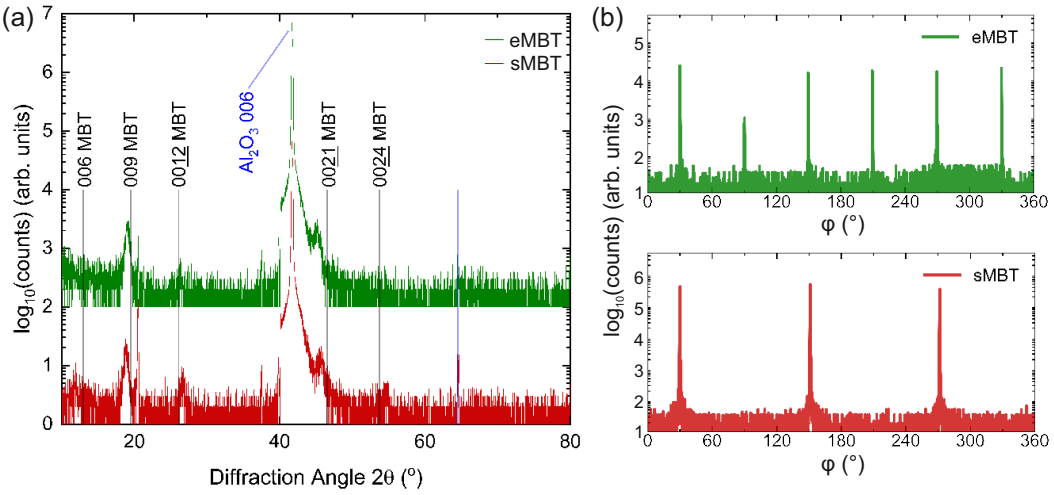


Figure 4.2: (a) X-ray diffraction patterns for both the eMBT and sMBT films. Both show (003$\underline{l}$) peaks consistent with the expected layered $MnBi_2Te_4$ structure. Small peak shifts can be observed and are attributed to lattice strain resulting from substrate mismatch. (b) Azimuthal scans for the (036) Bi_2Te_3 (for eMBT) and (02$\underline{2}\underline{5}$) $MnBi_2Te_4$ reflections (for sMBT). The eMBT shows sixfold rotational symmetry and threefold symmetry for the sMBT, with the former being consistent with a stacking fault (twinning). Figure taken from Ref. [111].

While the XRD data suggest that both films exhibit the $MnBi_2Te_4$ c-axis phase, the proximity of the (003$\underline{l}$) peaks for both Bi_2Te_3 and $MnBi_2Te_4$ makes it challenging to determine the exact phase in symmetric geometry. Figure 4.3 shows asymmetric RSM, providing additional insight into the phase of each film. The Mn-rich sample in Fig. 4.3(a) exhibits diffraction peaks consistent with Bi_2Te_3 films shown in Subsection 3.2.2,

while the stoichiometric sample shows a pattern indicative of $MnBi_2Te_4$. This suggests that excess Mn may prevent the formation of the SL MBT phase, potentially by forming $MnTe_x$ secondary phases or amorphous Mn clusters. This is in slight contradiction to the high Mn concentration causing the Bi_2Te_3 phase to break down in Subsection 3.2.2, but the difference in growth methodologies may mean the sputtering pathway allows non-MBT configurations that preserve a TI phase beyond the Mn-doping threshold. This also means that the estimation of the lattice spacing is incorrect for the eMBT sample, as the peak identified as $MnBi_2Te_4$ (009) is actually Bi_2Te_3 (006); therefore, the c-lattice parameter for eMBT is (27.8±0.1) Å.

To assess in-plane grain orientation, azimuthal (φ) scans were performed on selected reflections, shown in Fig. 4.2(b). The eMBT film shows a six-fold rotational symmetry, consistent with the presence of twinning. Twinning is a stacking defect caused by in-plane rotations of the unit cell. In a rhombohedral structure such as $MnBi_2Te_4$ this is a rotation of 60° and results in an apparent six-fold rotational symmetry compared to the expected threefold symmetry. This defect is common in van der Waals materials due to their weak interlayer bonding in the presence of a substrate symmetry mismatch [112], with the effect exacerbated during nucleation. The sMBT sample shows the expected threefold symmetry, suggesting that when the stoichiometry is correct, the annealing step drives ordered stacking and promotes domain coalescence.

Tapping-mode AFM, shown in Fig. 4.4, was used to characterise the morphology and grain structure of the film. The eMBT film exhibits a high roughness (5.6 nm) and large, rounded grains with an average diameter of 160 nm. This is a significantly different structure to the sMBT sample, which shows a much smoother surface with a roughness of 1.3 nm and reduced grain size and regularity. Owing to the film's smooth surface, a

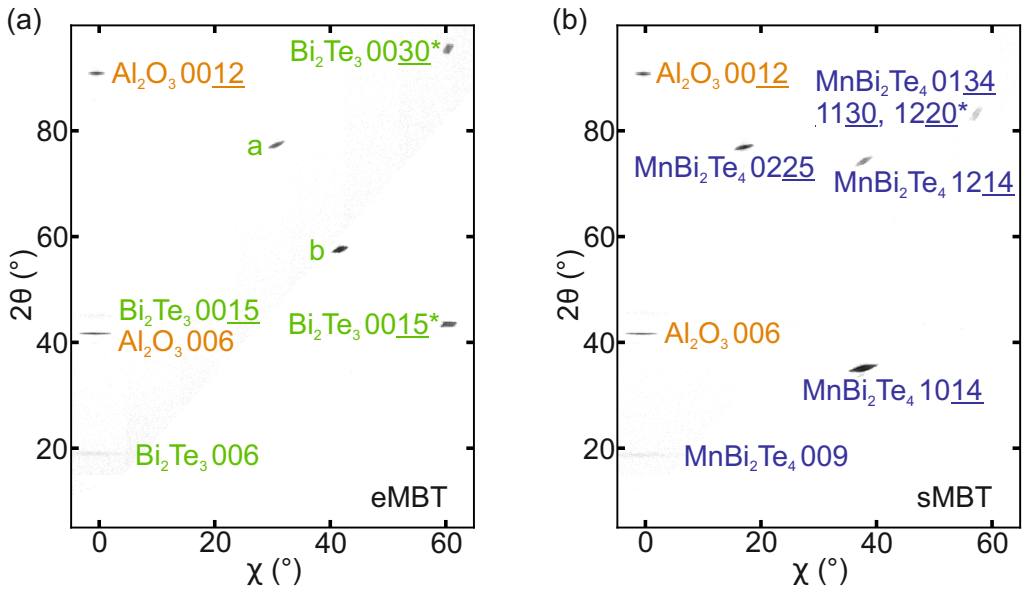


Figure 4.3: Asymmetric reciprocal space maps of the films displayed in Fig. 4.2. (a) Excess-Mn sample (eMBT) shows a pattern suggesting a Bi_2Te_3 phase, indicating the septuple-layer structure of $MnBi_2Te_4$ did not completely form. The peaks labelled a and b can be indexed with Bi_2Te_3 peaks $(\bar{1}\bar{1}20)$ or $(\bar{2}120)$ and $(\bar{1}\bar{1}13)$ or $(\bar{1}213)$, respectively. (b) The near-stoichiometric sample (sMBT) displays well-defined diffraction peaks showing an $MnBi_2Te_4$ phase, confirming the phase has correctly formed during annealing under correct compositional conditions. Peak labels including an asterisk (*) are best-effort estimates based on the expected symmetry and lattice parameters. Figure taken from Ref. [111].

watershed-based segregation of grains was not effective at estimating grain sizes, with a line profile analysis instead used to yield an estimate of ∼115 nm. The difference between the two samples is consistent with the higher crystallographic coherence and reduced twinning seen in the XRD of the sMBT sample.

The reduction in surface roughness is crucial for XMLD measurements, which are highly sensitive to magnetic anisotropies averaging across the beam footprint (approximately 150 μm). As such, the structure of the sMBT film makes it a more suitable

candidate for synchrotron-based linear dichroism to probe for evidence of antiferromagnetic order.

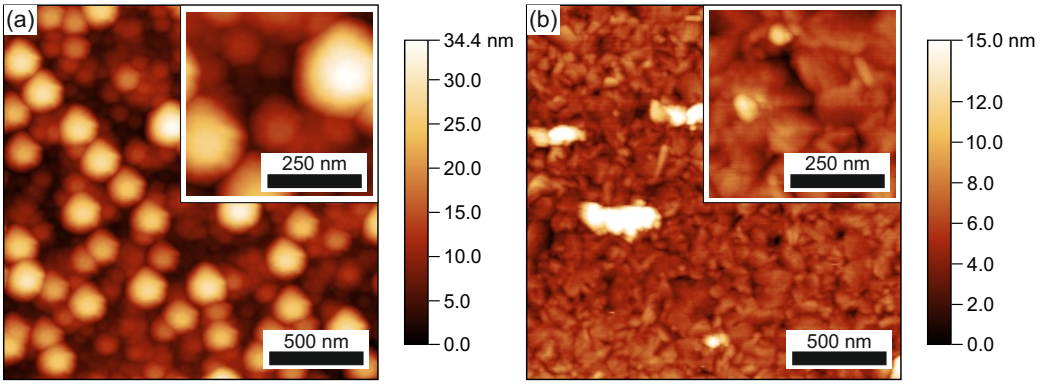


Figure 4.4: Tapping-mode AFM scans of the eMBT and sMBT films. (a) The eMBT film shows large, round grains of ∼160 nm in diameter and a high surface roughness of 5.6 nm. (b) The sMBT film shows a more irregular grain morphology but a much lower roughness of 1.3 nm. Figure taken from Ref. [111].

4.4 Magnetic Characterisation

Initial magnetic characterisation was assessed using SQUID-VSM in out-of-plane geometry, with both field-dependent and temperature-dependent measurements, with the results for both eMBT and sMBT shown in Fig. 4.5. $M(H)$ loops at 5 K, displayed in Figs. 4.5(a, b), show a very low coercivity and an unsaturated, near linear response at high field, suggesting weakly coupled or paramagnetic Mn moments. This behaviour matches the behaviour seen in Subsection 3.2.3, and can be attributed to the continuous reorientation of domains alongside the competing ferromagnetic and antiferromagnetic interactions [90, 113].

To obtain an estimate of the moment per Mn atom from the SQUID data, magnetisation was first normalised by Mn content as determined by SEM-EDS alongside

thicknesses obtained from XRR fits.

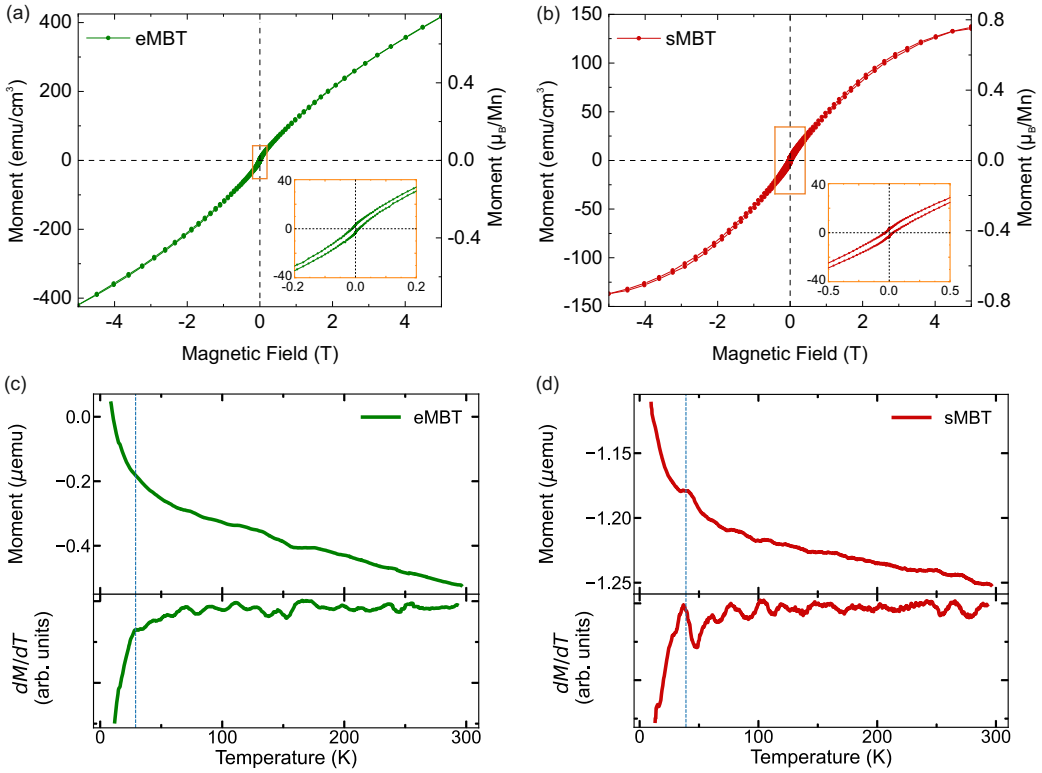


Figure 4.5: Field- and temperature-dependent SQUID-VSM data for both films in out-of-plane geometry, note magnetic moments are given in both emu/cm^3 and μ_B/Mn for (a,b). (a,b) $M(H)$ curves at 5 K show both low coercivity (23 mT for eMBT and 67 mT for sMBT) and high-field paramagnetic behaviour. The insets highlight the low-field response as indicated. The Mn-rich film in (a) shows a higher moment than the sMBT film in (b), which in turn shows signs of approaching saturation at 5 T. However, the films have similar remanence of 6emu/cm^3 and 7emu/cm^3 for eMBT and sMBT respectively. (c,d) $M(T)$ plots (top) measured at a field of 100 Oe, and their derivatives (bottom), showing both samples undergo a transition around 30 K, with an additional transition visible at ∼8 K for the sMBT film in (d). Both transitions are marked with dashed vertical lines. Figure taken from Ref. [111].

Due to the unsaturated paramagnetic response, the weak magnetic contribution of the film, disordered contributions from the film, and the competing diamagnetic substrate, background removal based on a reference substrate yielded non-physical results. To resolve this issue, the magnetic moments (right-hand side axis for Figs. 4.5(a, b)) were scaled to spin moments measured at 5 T as determined by sum rules analysis. This value itself was scaled down from the calculated value using an XMCD-based hysteresis loop shown in Fig. 4.9. The result of this shows that the sMBT approaches saturation in contrast to the eMBT film, suggesting a more uniform magnetic ordering, which may result in stronger interlayer coupling.

In-plane hysteresis loops at 5 K, processed using the same background subtraction method as the out-of-plane samples but scaled to the slightly reduced moments seen in these measurements, can be seen in Fig. 4.6. These loops yield very similar results to the out-of-plane data, not exhibiting a spin-flop transition as expected. This transition is a primary indicator of antiferromagnetic order, with an example of a weak transition in bulk $MnBi_2Te_4$ shown by Zeugner *et al.* [103]. The inability to observe such a transition suggests that there is no stable antiferromagnetic phase, potentially due to structural defects and interstitial Mn atoms disrupting the superexchange between Mn layers. This initial result will be further explored through $M(T)$ measurements and XMLD.

Temperature-dependent measurements (Fig. 4.5(c, d)) provide insight into the complex magnetic structure of these films. In both films, a broad feature appears between 30-40 K, but with notably different characteristics. The eMBT film shows a weak discontinuity near 30 K, suggesting the onset of partial magnetic ordering. In contrast, the sMBT film exhibits two features, with a shallow increase in moment around 35-40 K and a slight anomaly near 8 K. The higher temperature feature is likely linked to residual interlayer

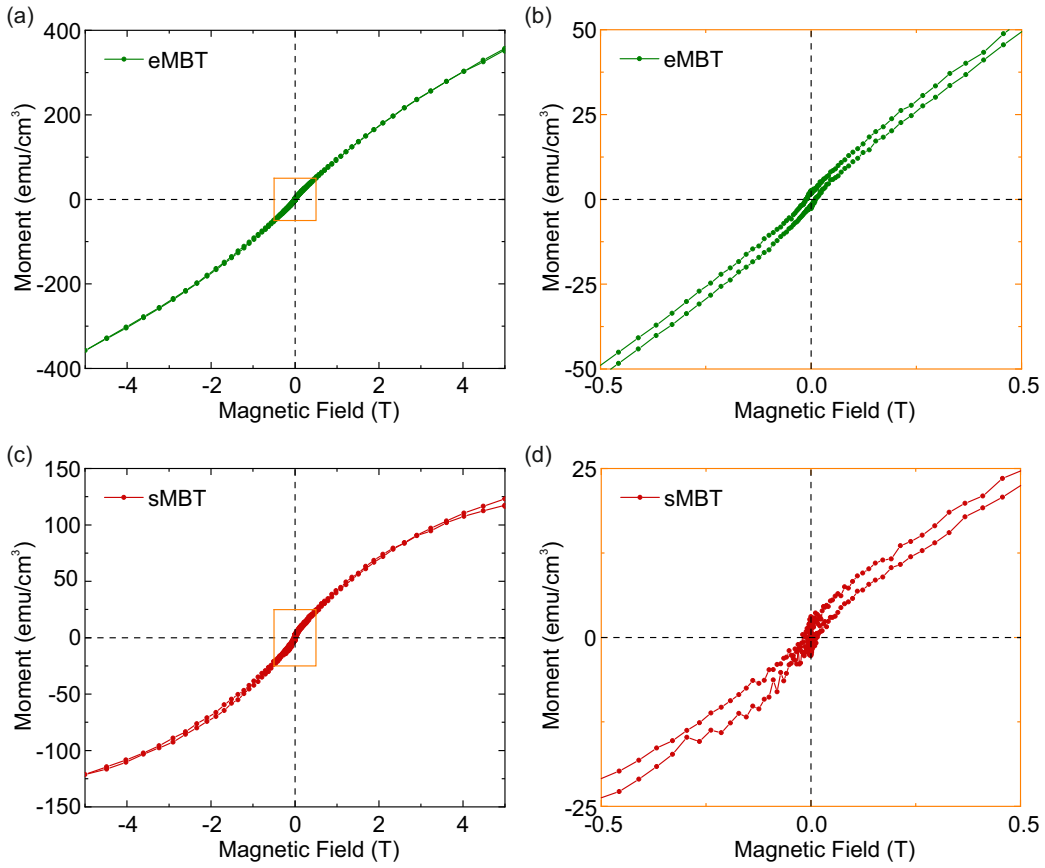


Figure 4.6: Field-dependent SQUID-VSM data at 5 K for both films in an in-plane geometry. (a,b) Curve for the eMBT sample, showing similar low coercivity and high field paramagnetic behaviour as the out-of-plane measurements. (c,d) $M(H)$ plots for the sMBT sample showing the film has a lower moment and appears to be closer to saturation than the eMBT film, as in the out-of-plane data. Neither sample exhibits evidence of a spin-flop transition, indicating that there is no bulk antiferromagnetic order.

coupling. In contrast, the lower temperature discontinuity provides evidence of a second distinct phase — such as an antiferromagnetic phase — but the data does not provide enough information to confirm its origin.

Overall, the SQUID data supports the existence of compositionally and/or structurally

driven magnetic disorder in the eMBT film, where the excess Mn may form weakly ferromagnetic regions, increasing the moment while weakening the overall coherent long-range magnetic order. Conversely, the sMBT film remains magnetically ambiguous, with the two transitions observed in the $M(T)$ plots suggesting two distinct magnetic phases; however, the absence of a spin flop transition implies that there is no robust antiferromagnetic order. Therefore, it can be concluded that, despite its improved structural properties, A-type antiferromagnetic order is suppressed by disorder and residual stacking defects.

In addition to the bulk magnetometry, the magnetic ground state of the Mn atoms was probed using synchrotron-based XMCD at the $L_{2,3}$ edges for both the eMBT and sMBT films, shown in Fig. 4.7. All measurements were performed using TEY detection at a temperature of $\sim$2 K in an applied field of 6 T parallel to the beam direction in normal incidence. Both spectra exhibit features consistent with Mn^{2+} in a chalcogenide environment, with no peak splitting suggestive of oxidation or Mn in a different, metallicity-bonded environment [103]. The XMCD spectra extracted from the XAS spectra show unique results for both samples; notably, the size of the XMCD signal is larger for the Mn-rich sample than the stoichiometric sample, consistent with the higher net magnetisation observed in the SQUID data.

Quantitative analysis of the spectra was performed using sum rule analysis based on the normalised spectra, as detailed in Subsection 2.3.2 and by Thole *et al.* [72]. The spin and orbital moments per Mn atom are $m_S = 0.870\,\mu_B$ and $m_L = 0.021\,\mu_B$ for eMBT, and $m_S = 0.840\,\mu_B$ and $m_L = 0.038\,\mu_B$ for sMBT. These values are in agreement with those reported for a 16.3 nm thick, MBE grown $MnBi_2Te_4$ film [114]. It should be noted that the values reported in Ref. [114] of $m_S = 1.64\,\mu_B$ and $m_L = 0.16\,\mu_B$, were measured at

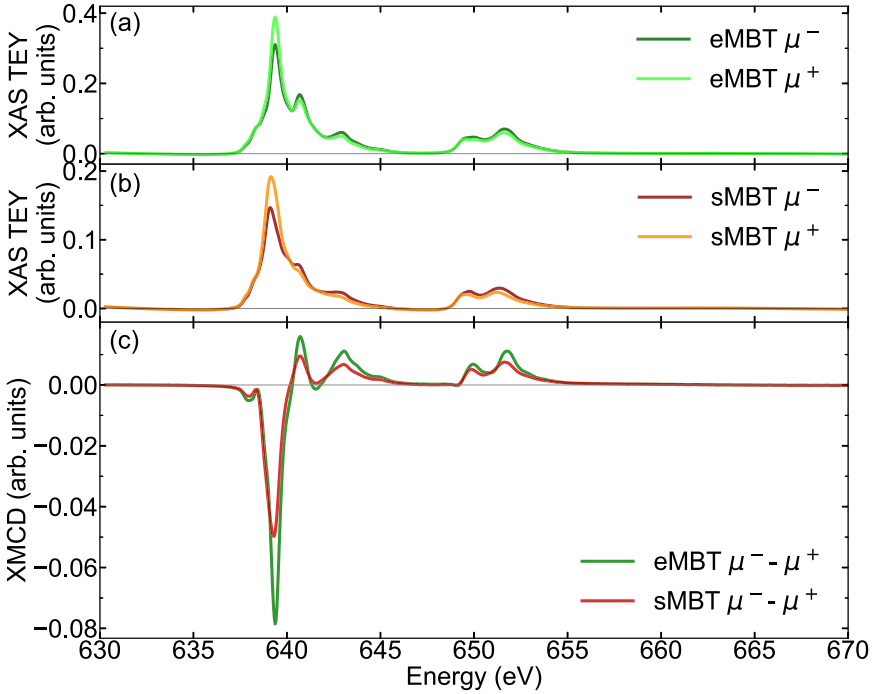


Figure 4.7: (a,b) XAS and (c) XMCD spectra measured using TEY under an applied out-of-plane field of 6 T at a temperature of 2 K on the $L_{2,3}$ edges on both eMBT and sMBT films. (a,b) XAS under positive and negative polarisation for eMBT and sMBT, respectively. Both display multiplet structures typical of Mn^{2+} in chalcogenide materials. (c) The larger XMCD signal of the eMBT film reflects its higher Mn moment per atom, while the structure of the spectra suggests comparable local environments in both samples. Figure taken from Ref. [111].

3 K at a field of 14 T. However, the field-dependent values show that at 5 T the magnetic moments are $\sim$0.75 and $< 0.1\,\mu_B$/Mn for the spin and orbital moments, respectively [114]. In addition, it is worth emphasising that the moments for thin films are much smaller than the ordered moment of $\sim 4\,\mu_B$/Mn reported for bulk $MnBi_2Te_4$ single crystals at 10 K [115], suggesting the presence of structural and/or secondary phases [116, 117].

The calculated values yield a m_L/m_S ratio of 0.024 for eMBT and 0.045 for sMBT, respectively. This means that the $3d$ orbital is slightly higher than half-filled (Mn^{2+}

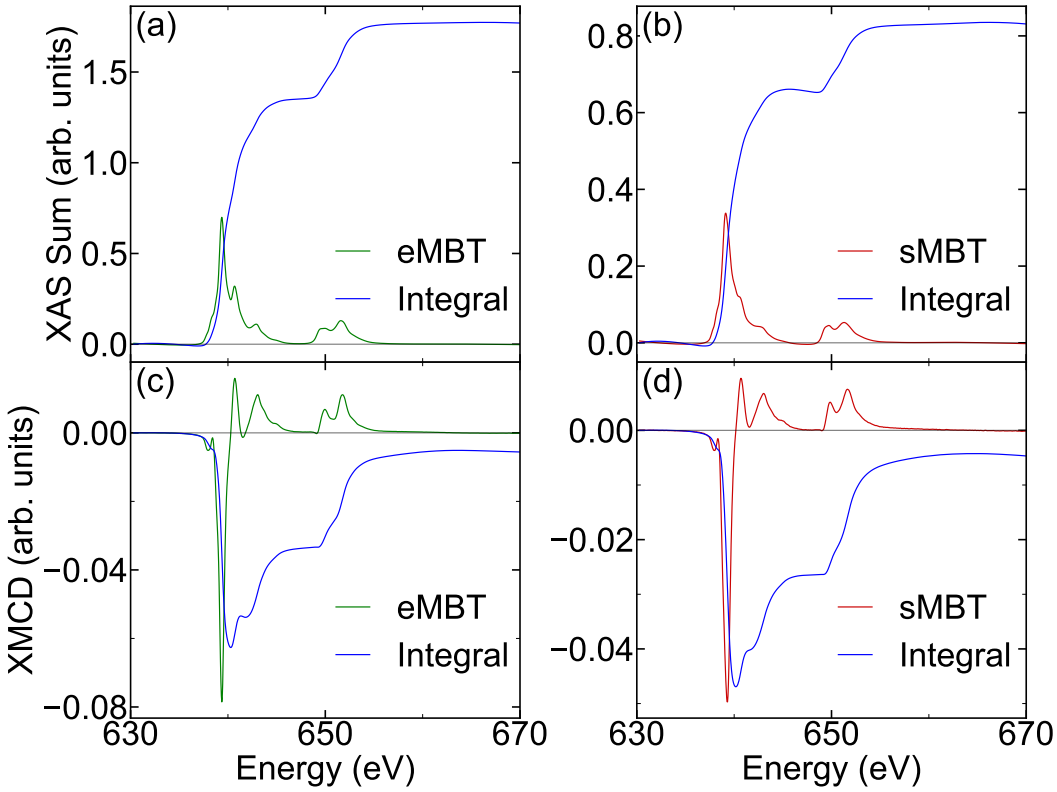


Figure 4.8: Graphs showing the integrals from the sum rules calculations. (a,b) Shows the sum of the XAS spectra and the cumulative integral for the eMBT and sMBT samples, respectively. (c,d) XMCD spectra and integral for the eMBT and SMBT samples. In addition to the whole spectrum, the integral was also assessed over just the L_3 edge for the sum rules calculations. Figure taken from Ref. [111].

$3d^5$), in accordance with Hund's third rule. This hints at hybridisation between the Mn $3d$ and Te $5p$ orbital. The latter conclusion is supported by the prepeak seen at 638.0 eV in Fig. 4.7(c) [118]. The higher orbital moment in the sMBT film, despite its lower net magnetisation, suggests some differences in crystal field symmetry or site occupation for the Mn atoms. However, interpreting these results is complicated due to the overlapping effects of structural disorder and magnetic inhomogeneity.

Attempts were made to measure antiferromagnetic order using XMLD in these films,

to confirm the presence of A-type antiferromagnetism via anisotropic absorption. Despite the low roughness and improved structural coherence of the sMBT sample, efforts to recover a reliable XMLD spectrum proved unsuccessful. This result is probably due to a combination of factors, including residual surface roughness, structural defects, and the potential of Mn atoms situated outside their expected lattice site to partially decouple the main Mn layers. All of these have the potential to suppress the XMLD response via the spatial averaging of the uniaxial anisotropies across the beam footprint.

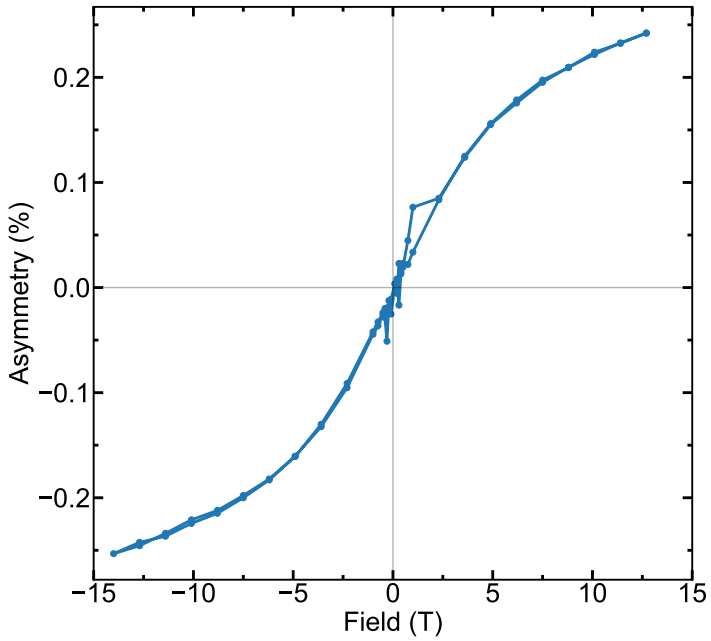


Figure 4.9: XMCD hysteresis loop for the Mn L_3 edge for sample 589, a sample compositionally similar to the sMBT. This sample was measured in TEY at 7.5 K. The XMCD asymmetry increases with applied field, not saturating even at 14 T, consistent with paramagnetic-like behaviour. The low-quality data around zero field is due to trapped current causing imperfect field control, as well as low applied field, making TEY detection less reliable. Figure taken from Ref. [111].

Figure 4.9 shows an XMCD hysteresis loop of a sample that is compositionally or structurally similar to sMBT (sample 589, see Table 4.1). The hysteresis loop was measured at the Mn L_3 edge and the peak asymmetry, defined as $(\mu^+ - \mu^-)/(\mu^+ + \mu^-)$ [119], increases steadily with applied field up to 14 T, with no sign of magnetic saturation, consistent with paramagnetic behaviour. This trend matches with the magnetisation response observed in the SQUID-VSM $M(H)$ data for the sMBT film in Fig. 4.5, where the moment also increases linearly without any indication of a saturation field. While the XMCD loop appears closed, the signal-to-noise ratio near zero field is not adequate to determine whether residual spin polarisation is present in the remanent state. This is due to the TEY signal degrading at low applied field, as the magnetic field assists in the flow of the drain current off the holder.

4.5 Discussion

Structural and magnetic measurements of sputtered MBT thin films reveal a non-linear dependence between sputter power and composition, alongside a strong coupling between Mn content, phase stability and magnetic ground state. While the $MnBi_2Te_4$ target phase can be stabilised at near-stoichiometric composition, excess Mn leads to the emergence of secondary phases, stacking defects, and suppressed magnetic order. As indicated by out-of-plane XRD and asymmetric-RSM, the Mn-rich film adopts features consistent with a Bi_2Te_3 like phase, rather than $MnBi_2Te_4$ septuple layer stacking. This result contrasts with the conclusions drawn in Section 3.2, where increasing Mn content destabilised the host Bi_2Te_3 phase. This could be due to differences in synthesis methodology, with the films in this chapter deposited at room temperature and then crystallised during a separate annealing stage. This approach, with the film exposed to higher temperatures for a longer time, enables greater mobility of adatoms during the

anneal, potentially promoting phase segregation and the expulsion of excess Mn beyond what can be accommodated substitutionally or interstitially. In addition to this change in annealing method, an independent Te flux was included during deposition, which may enable the formation of Te-rich phases, such as $MnTe_x$-type compounds. These regions may remain amorphous or nanocrystalline, and therefore may be difficult to detect via XRD; however, they can strongly influence the film's magnetic behaviour through the disruption of long-range magnetic ordering.

In addition to Te-based compounds creating secondary phases, MnBi can form a known ferromagnetic alloy [120–122]. This is in agreement with the EDS data, which shows a significant Bi excess and Te deficiency in the eMBT films. During annealing, Te may desorb from the film, resulting in a larger deviation from the ideal stoichiometry and an increased likelihood of MnBi formation. Secondary phases, MnBi in particular, could explain the increased moment and paramagnetic background observed in the eMBT sample, as well as the absence of a well-defined magnetic transition.

In contrast, the sMBT film shows reduced roughness, minimal twinning, and improved structural properties. However, the magnetic measurements show weak features at 8 K and 35-40 K, and an absence of reliable XMLD spectra suggests that these improvements are not adequate to permit coherent interlayer antiferromagnetism. Although XMCD calculated spin moments and high-field $M(H)$ values (when normalised by Mn content) are similar for both eMBT and sMBT samples, this does not imply equivalent ground states. In the Mn-rich sample, the excess Mn may form magnetically active clusters or locate interstitially that then contribute to the moment but don't coherently order over long ranges. This means they either order ferro- or paramagnetically, increasing the net moment of the sample while disrupting the A-type antiferromagnetism coupling across

long ranges.

The sMBT film, conversely, exhibits few signs of secondary phase formation, which should support better magnetic coherence but still shows no robust XMLD signal. Therefore, given the lack of A-type antiferromagnetism in both samples, we can conclude that the long-range coherence is more easily disrupted than the atomic-scale magnetism, which remains similar for both samples. This indicates that, despite improvements to the sample's composition and structure, there is still sufficient disruption to suppress long-range ordering. However, if the Mn atoms in sMBT were magnetically inactive, a lower moment per Mn atom could be expected, which contrasts with the XMCD and SQUID data. This implies that magnetic disorder is driven by subtle disruptions in the inter-layer exchange pathways, rather than a reduction in Mn content that directly contributes to the bulk magnetism.

Indeed, several contributing factors, such as nanoscale stacking faults, Mn intercalation into van der Waals gaps or non-stoichiometric substitution of Mn, could contribute to the disruption of A-type antiferromagnetic order in epitaxial $MnBi_2Te_4$ [96, 102, 123]. In addition, excess carriers from interstitial Mn or antisite defects may destabilise the antiferromagnetic ground state [83]. Therefore, while magnetron sputtering offers smoother surface morphology, stabilising the $MnBi_2Te_4$ phase in thin film form remains a challenge. Despite this, the improved crystallinity of the stoichiometric sputtered thin films, particularly the smoother surface and suppression of twinning, suggests that it is possible to refine the growth parameters to achieve a higher quality film. This could include a change in substrate choice and annealing conditions, such as slower temperature ramping or multistage annealing, which allows for improved structural properties, making XMLD measurements possible.

In summary, structural and magnetic properties of sputtered MBT thin films of various compositions were investigated. While this growth method offered numerous advantages, such as low roughness and high scalability, issues arose in realising the intrinsic antiferromagnetism required to observe exotic quantum phases, including QAHE and axion insulator states [97, 105, 108]. The results show that, despite films with the correct stoichiometry exhibiting enhanced structural characteristics, this does not translate to improved long-range magnetic order, with no reliable XMLD able to be extracted. These findings are consistent with previous reports highlighting the sensitivity of magnetism in MBT to structural disorder, Mn intercalation, and stoichiometric irregularity [97, 103, 123]. The absence of robust XMLD signals, even in smooth films, suggests that the odd-even layer effects, visible in exfoliated samples [108], are suppressed by localised inhomogeneity, incomplete septuple layer formation, and stacking faults. These effects could cause partial decoupling of Mn sublattices, disrupting the A-type antiferromagnetism.

Future expansion of this work should focus on a more detailed microscopic analysis of sputtered films using TEM and X-ray photoelectron spectroscopy to assess phase purity and local stoichiometry. In addition, refining the annealing process and exploring alternative substrates could reduce lattice strain and enhance crystallinity, thereby improving interlayer magnetic coupling. Furthermore, improved capping layers could prevent Te desorption during annealing, preventing a Te deficiency in the films post-anneal. These steps will determine if sputtering is a viable substitute for exfoliation-based methods for stabilising antiferromagnetic order in MBT.

Overall, while the project failed to realise the intrinsic magnetic topological behaviour in sputtered MBT, it provided insight into the relationship between growth conditions,

structural properties and magnetic response. This paves the way for future work with a more targeted experimental parameter space, enabling refinement of growth protocols in the search for scalable systems that can demonstrate the full range of quantum effects predicted for intrinsic magnetic topological insulators.

Chapter 5

Spin-Orbit Torque Measurements of a Nanocrystalline Topological Insulator-Ferromagnetic Bilayer

5.1 Motivation

Torques driven by the spin-orbit interaction are an emerging field of study due to their potential to efficiently drive the electronic control of the magnetisation direction for a ferromagnet. This has yielded a wide range of effects, from spin-transfer torque (STT) predicted by Slonczewski and Berger in 1996 [124, 125], in which spin current can be transferred from one material to another. Later, the Rashba and Edelstein effects, able to produce spin polarisation in the conduction band of semiconductors [126, 127], were identified as able to drive a spin-orbit torque [128–132]. This torque differs from STT, as rather than the transfer of spin angular momentum, orbital angular momentum is transferred between the SOC material and the FM layer [133]. This enables reversible switching of the FM layer by reversing the current direction, enabling easy control of memory devices, such as magnetic tunnel junctions.

The most studied of these structures are ferromagnetic-normal metal (FM/NM)

[134–138], these systems use a heavy metal with high spin orbit coupling, such as Pt, with the torque produced attributed to a range of mechanisms. These include the SHE [139], a field like torque due to the Rashba effect [133], and ferromagnetic resonance (FMR) in the case of RF current injection [140]. However, the push for higher spin-orbit torques has led to a variety of materials being explored, including graphene [10, 141], WTe_2 [142–145] and TIs [37, 146–150]. In particular, TI/FM devices offer advantages over NM/FM systems for generating high SOTs due to their unique band structure. In the case of a single Dirac cone TI, such as Bi_2Te_3 or Sb_2Te_3 the direct coupling of spin and momentum offers TIs an advantage over 2DEG systems, such as graphene, in the generation of spin currents [10]. This is due to spin-momentum locking in the surface state, causing efficient spin accumulation near the surface, and the spin polarisation being directly tied to the current direction [146].

However, the variability of the Fermi surface in TIs adds complications to its spin-orbit properties. The bulk properties of TIs determine this [146] and can lead to a more metallic-like state when the Fermi surface is situated above the inversion point. However, this can be tuned with the application of a gate voltage [151]. Combining this with the breaking of time-reversal symmetry, which forms a band gap, the Fermi energy can be placed within the band gap, resulting in the QAHE effect.

This chapter will focus on the study of TIs as room-temperature SOT devices, exploring how nanocrystalline sputtered TIs enhance SOT through the calculation of the Spin Hall angle, defined as the ratio of the measured spin current to the injected charge current through the TI. It is hoped that the confinement provided by the nanocrystalline nature of the sputtered films will enhance the SOT, expanding the work performed by Mahendra *et al.* [37]. This project was performed in collaboration with Dr. Angadjit

Singh, Dr. Safeer Chenattukuzhiyil, and Piotr Sawicki. To measure this parameter, TI/FM bilayers were grown by myself and patterned into hall bars (led by Dr. Singh, aided by myself and Piotr Sawicki), and measurements of the planar and anomalous Hall effect were made (led by Dr. Singh, aided by Dr. Chenattukuzhiyil and Piotr Sawicki)[151]. These measurements, combined with measured properties of single-layer reference samples of both FM and TI layers, enable the spin-Hall angle to be calculated (calculations performed by myself, assisted by Piotr Sawicki) via the Slonczewski equation [152], with the complete method detailed in Section 5.3.

5.2 Growth and Fabrication of Bilayer Devices

Topological insulator thin films were grown using the same two-step process described in Subsection 2.4.3, where a seed layer was deposited at 200°C before the main layer was deposited at 250°C. This gave an 8 nm layer of Bi_2Te_3 upon which a second layer of $Ni_{20}Fe_{80}$ of various thicknesses was deposited at room temperature. A diagram of the layers in the device can be seen in Fig. 5.4

Upon analysing these films using XRD, it was found that an additional peak was visible in a simple bi-layer structure, shown in Fig. 5.1. Investigating this further, it became apparent that the peak was caused by a secondary $NiTe_2/FeTe_2$ phase resulting from diffusion into the TI layer. This effect has been observed between calcogenide compounds and commonly used contact metals and ferromagnets [153], with NiFe noted as one of the most reactive compounds with Bi_2Se_3 [154].

This phase is problematic as it has the potential to disrupt the stability of the TI surface states, while also introducing another magnetic material into the heterostructure, which complicates any analysis of transport results and prevents a direct measurement of the spin-Hall angle. To resolve this issue, a spacer layer of Al was used. Al was chosen

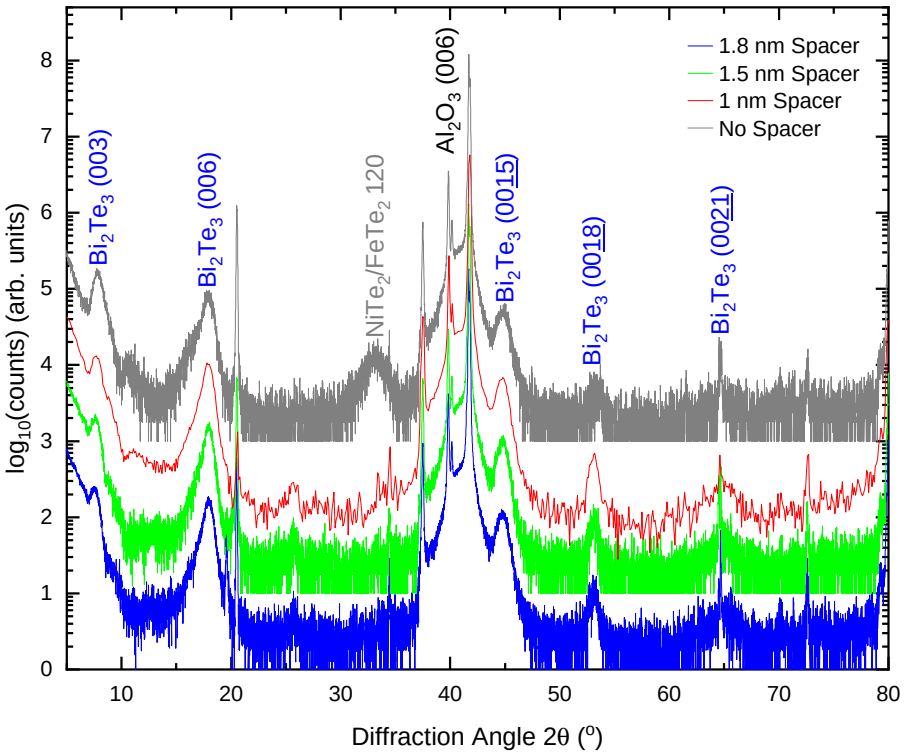


Figure 5.1: XRD measurements of multiple Bi_2Te_3-$Ni_{20}Fe_{80}$ bilayers with various thicknesses of Al spacer layer. It should be noted that the higher quality data for the 1 nm spacer sample was taken as there was uncertainty over the presence of the $NiTe_2/FeTe_2$ peak, which required improved signal-to-noise to determine clearly. This was not done for all of the films owning to the trade off between measurement time and signal-to-noise.

due to its low atomic number, resulting in a small spin-orbit coupling, ensuring it won't provide an additional torque in SOT measurements.

However, it was crucial to determine the minimum thickness of the spacer layer required to prevent diffusion, as this layer would increase the distance between the surface states and the ferromagnet, thereby reducing the coupling between them. Therefore, multiple thicknesses of Al layers were tested, as shown in Fig. 5.1, and the thinnest layer that removed the peak at approximately $\sim 33°$ was identified. It should be noted that

data with an improved signal-to-noise ratio was required for the 1 nm spacer layer due to uncertainty about the peak at ∼33° being still weakly visible. This showed no peak was present and therefore the 1 nm spacer was selected.

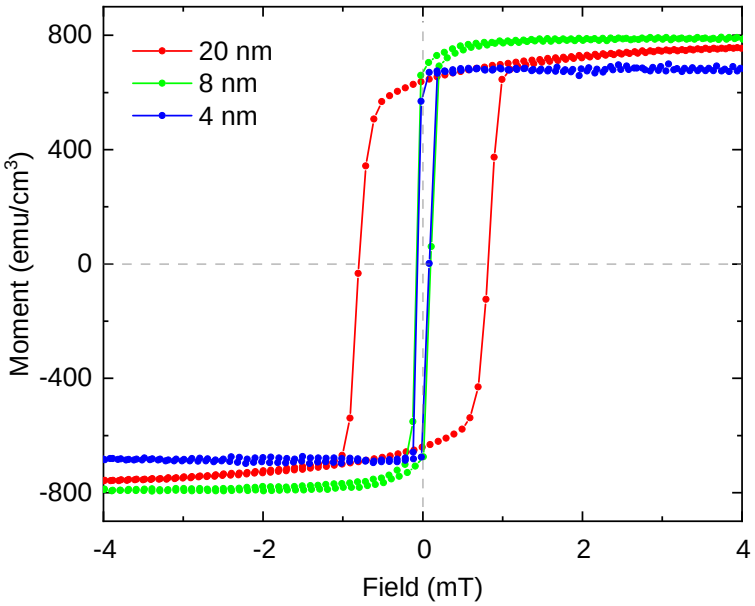


Figure 5.2: VSM $M(H)$ loops taken at room temperature for capped $Ni_{20}Fe_{80}$ layers, showing the effect of thickness on coercivity. A slight variance in saturation magnetisation can be seen, which can be attributed to subtle differences in growth parameters and alignment in the VSM.

The impact of the thickness of each layer on the magnitude of the SOT was also considered. Firstly, the dependence of the thickness of the TI was not explored; this is due to the study's focus on the SOT resulting from the surface states. Therefore, a thickness of 8 nm selected as this is the minimum thickness to limit the chance of hybridisation between the surface states at the top and bottom of the film, thereby reducing the bulk contributions to the SOT. With this thickness held constant, the thickness of the ferromagnet, t_{FM}, was varied to find an ideal thickness for measurement.

This forced a trade-off, as past studies show that SOT efficiency changes with a $1/t_{\mathrm{FM}}$-like relation [155–157]. However, as the experimental setup had limited resolution, a thicker magnetic layer allowed for easier control of the device. As a result, a range of $Ni_{20}Fe_{80}$ thicknesses were used in different multi-layers, with the hope of finding an ideal thickness for measuring the spin Hall angle, allowing future studies to explore the TI thickness dependence systematically. Hysteresis loops taken in a VSM at room temperature for a range of single-layer $Ni_{20}Fe_{80}$ films are shown in Fig. 5.2 and used as a reference for the bilayer growths.

These films were patterned into cross-shaped Hall bars using UV photolithography, as detailed in Section 2.5. The resulting devices have dimensions of $\sim 500 \times 50\,\mu\mathrm{m}^2$ for the vertical bar and $\sim 300 \times 50\,\mu\mathrm{m}^2$ for the horizontal bar, shown in Fig. 5.3(a). These films were then glued and wire-bonded onto sample holders, with an example shown in Fig. 5.3(b), then mounted on a probe for transport measurements.

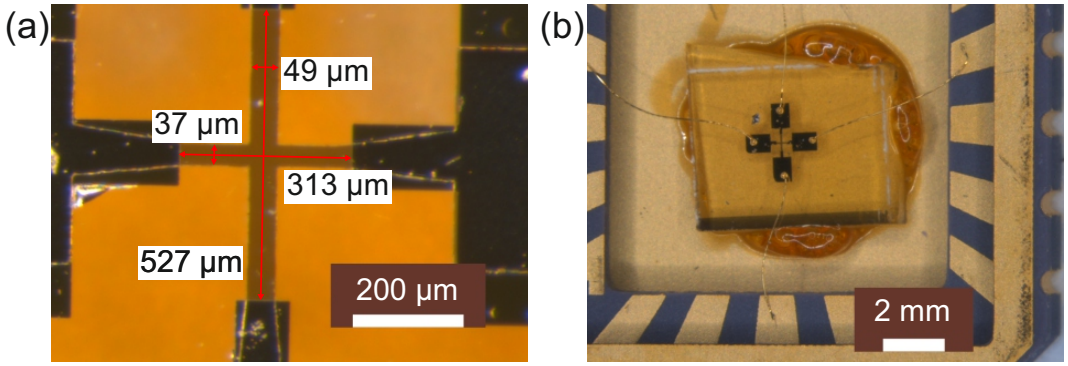


Figure 5.3: Images of Bi_2Te_3-$Ni_{20}Fe_{80}$ thin films patterned into cross-shaped devices. (a) Optical microscope image of a cross-patterned device with dimensions labelled on the sample. (b) Image of a Hall bar attached to a chip carrier and wire-bonded, ready for measurement.

5.3 Methodology for the Determination of Spin Hall Angle

After the bilayers had been patterned into the Hall-cross bars, spin-orbit torque was determined using anomalous and planar Hall effect (PHE) measurements. This method relies on the Slonczewski equation [152]:

$$\tau_{||} = \frac{\hbar}{2e}\frac{J_s}{M_s t_{\mathrm{FM}}}[\hat{m} \times (\hat{\sigma} \times \hat{m})] \tag{5.1}$$

where $\tau_{||}$ is the in-plane SOT, J_s is the spin-current density, M_s is the saturation magnetisation, t_{FM} is the thickness of the ferromagnetic layer, $\hat{m}$ is the magnetisation unit vector and $\hat{\sigma}$ is the unit vector of the induced spin polarisation at the TI-FM interface. This equation is the basis for the measurement method detailed below, with the following equations fully discussed by Mahendra *et al.* [37]. The effective magnetic field from the in-plane torque $\tau_{||}$ is given by $H_{\mathrm{OOP}} = \frac{\hbar J_s}{2eM_s t_{\mathrm{FM}}}(\hat{\sigma} \times \hat{m})$ [37].

If we define the spin Hall angle as the ratio at which spin current J_s is produced relative to the charge current passed through the TI J_{TI}, then spin Hall angle can be expressed in terms of the out-of-plane effective field [37]:

$$\theta_{\mathrm{H}} = \frac{J_s}{J_{\mathrm{TI}}} = \frac{2e}{\hbar} M_s t_{\mathrm{FM}} \frac{H_{\mathrm{OOP}}}{J_{\mathrm{TI}}} \tag{5.2}$$

In addition to the in-plane torque there is also an out-of-plane component due to the increased spin density at the interface, which is proportional to $\tau_{||} \propto (\hat{\sigma} \times \hat{m})$, with an associated in-plane magnetic field H_T proportional to $\hat{\sigma}$ [37].

Therefore, to properly assess the spin Hall angle and the charge-to-spin conversion efficiency, determinations of H_{OOP} and H_{T} are required. To achieve this, the anomalous and planar Hall effects were measured. This required separating these effects from the significant contribution from the normal Hall effect, which was achieved by taking Hall

measurements at opposite current polarities, as both H_{OOP} and H_{T} are odd functions, in contrast to the normal Hall effect. The difference between the Hall resistance at opposite polarities will henceforth be referred to as $\Delta R_{\mathrm{H}} = \Delta R_{\mathrm{PHE}} + \Delta R_{\mathrm{AHE}}$.

The PHE is an in-plane angular dependency on the Hall resistance driven by anisotropic magnetoresistance [37, 158, 159]. The angular dependence is governed by the relation [37]:

$$R_{\mathrm{PHE}} = R^{0}_{\mathrm{PHE}} \sin 2\alpha \tag{5.3}$$

Using this relation in combination with the geometry shown in Fig. 5.4, it can be seen that when $H_{\mathrm{ext}} >> H_{\mathrm{T}}$ we get $\delta \approx (H_{\mathrm{T}} \cos\alpha)/H_{\mathrm{ext}}$, where δ is the angle between the magnetisation and the external magnetic field H_{ext}. Therefore the change in R_{PHE} can be written as [37, 160]:

$$\begin{aligned}
\Delta R_{\mathrm{PHE}} &= \frac{\partial R_{\mathrm{PHE}}}{\partial \alpha}\delta = \frac{\partial (R^{0}_{\mathrm{PHE}} \sin 2\alpha)}{\partial \alpha}\delta \\
&= 2R^{0}_{\mathrm{PHE}} \cos 2\alpha \cos\alpha \frac{H_{\mathrm{T}}}{H_{\mathrm{ext}}} \\
&= R^{0}_{\mathrm{PHE}} (\cos\alpha + \cos 3\alpha) \frac{H_{\mathrm{T}}}{H_{\mathrm{ext}}}
\end{aligned} \tag{5.4}$$

In addition, there is also out-of-plane torque caused by the Oersted field (H_{Oe}) driven by charge current flow through the TI layer. This is considered at the same time as H_{T}, so $H_{\mathrm{T}} \rightarrow H_{\mathrm{T}} + H_{\mathrm{Oe}}$ in the equations above.

The other significant contribution to the total Hall resistance is the anomalous Hall effect, the physical basis of which has been discussed in Subsection 1.2.2. The definition of the anomalous Hall effect is the ratio between the current I_x and the voltage measured transverse to it V_y when the applied field H_z is zero, i.e. $R_{\mathrm{AHE}}(H_z) = V_y(H_z)/I_x$.

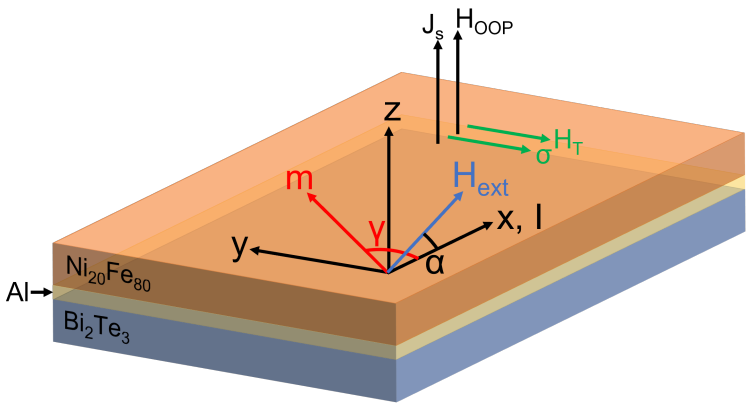


Figure 5.4: Diagram of the sample and measurement geometry for the AHE and PHE measurements undertaken in this chapter, including the direction of effective fields associated with the spin-orbit interaction, Oersted field, and spin-accumulation at the film's surface.

Experimentally, the anomalous Hall effect can be realised by measuring the Hall resistance as a function of applied magnetic field and measuring the deviation from the fitted function. As a result, the combined Hall resistance of the normal and anomalous Hall effect can be approximated as:

$$R_H(H_z) = R_{\mathrm{H}}^0 + R_{\mathrm{AHE}} \approx R_{\mathrm{H}}^0 + \frac{\partial R_{\mathrm{AHE}}}{\partial H_z} H_z \tag{5.5}$$

where R_{H}^0 is the resistance due to the Hall effect, H_z is an applied out-of-plane magnetic field. Therefore, the change in the anomalous Hall resistance will vary with H_{OOP} [160]:

$$\Delta R_{\mathrm{AHE}} = R_{\mathrm{AHE}}(+I) - R_{\mathrm{AHE}}(-I) \approx 2\frac{\partial R_{\mathrm{AHE}}}{\partial H} H_{\mathrm{OOP}} \cos\alpha \tag{5.6}$$

Now returning to the combined difference in Hall resistance $\Delta R_{\mathrm{H}}(I,\alpha) = \Delta R_{\mathrm{PHE}} + \Delta R_{\mathrm{AHE}}$ and measuring resistances with pairs of currents with opposite polarities [37, 160]:

$$\Delta R_{\mathrm{H}}(I,\alpha) = 2R_{\mathrm{PHE}}\frac{H_{\mathrm{T}} + H_{\mathrm{Oe}}}{H_{\mathrm{ext}}}(\cos\alpha + \cos 3\alpha) + 2\frac{\partial R_{\mathrm{AHE}}}{\partial H} H_{\mathrm{OOP}} \cos\alpha \tag{5.7}$$

For fitting, the prior equation can be expressed as:

$$\Delta R_{\mathrm{H}}(I,\alpha) = A + B\cos\left(\alpha - D\right) + C\cos\left(3(\alpha - D)\right) \tag{5.8}$$

Where A is a constant correction accounting for device/experimental asymmetry, $B-C = 2(\partial R_{\mathrm{AHE}}/\partial H)H_{\mathrm{OOP}}$, $C = 2R_{\mathrm{PHE}}(H_{\mathrm{T}} + H_{\mathrm{Oe}})/H_{\mathrm{ext}}$ and D is an angular offset due to systematic error in measuring the angle.

This relation means that rotating the sample in-plane, and therefore varying the angle between the applied current and the applied magnetic field, can be described using the relation given in Equ. 5.8. Taking the values of the fitting parameters B and C in particular allows H_{OOP} and H_{T} to be determined, and therefore the spin Hall angle to be calculated using Equ. 5.2.

5.4 Results

Four samples of various thicknesses were patterned and measured at the Clarendon Laboratory. However, a combination of device imperfections and device burnout caused by high current densities resulted in only a single sample providing quality data in PHE measurements. This sample was a multi-layer consisting of 8 nm of Bi_2Te_3, ∼1 nm of Al, 17.1 nm of $Ni_{20}Fe_{80}$ and 1.5 nm of Al as a cap. This Al capping layer was removed via chemical etching during the sample processing to protect it from oxidation. This step was then repeated to allow for a thinner oxidised layer, enabling the deposition of chrome-gold contacts, which improved the conduction of the sample. However, issues remain, as high currents destroyed this sample before an anomalous Hall measurement could be taken. To resolve this issue, the $\partial R_{\mathrm{AHE}}/\partial H$ was taken from another sample and scaled according to the difference in thickness between the two ferromagnetic layers (17 nm against 11 nm), accounting for the different current densities that would pass

through the TI. This provides an approximation when an accurate measure was not possible due to device burnout by assuming a linear thickness dependence of $\partial R_{\mathrm{AHE}}/\partial H$. Repeat measurements on new growths were not possible as the experimental setup was modified to no longer accept devices of the design shown in Section 5.2.

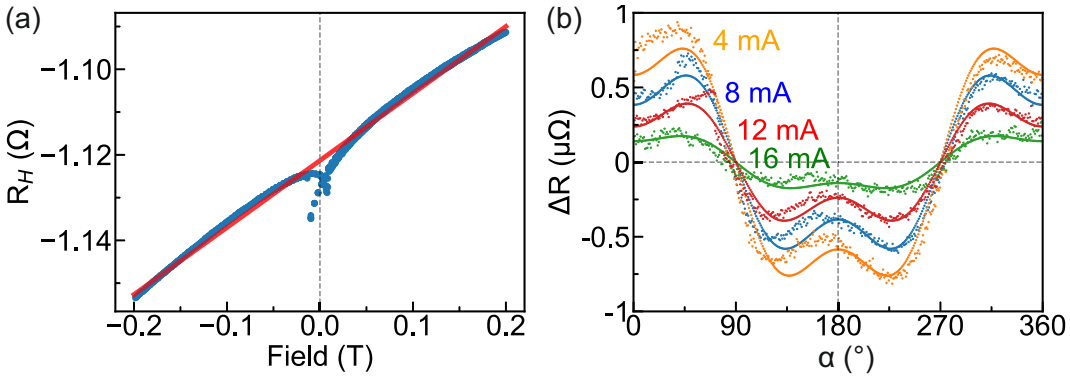


Figure 5.5: Anomalous and planar Hall effect measurements on Bi_2Te_3-$Ni_{20}Fe_{80}$ bilayers. (a) AHE measurements for a bilayer with an $Ni_{20}Fe_{80}$ thickness of 11 nm. An anomaly around zero field can be observed, probably due to electronic issues in the measurement setup. (b) PHE measurements at multiple input currents for a bilayer with 8 nm and 17 nm thicknesses of Bi_2Te_3 and $Ni_{20}Fe_{80}$, respectively. Data is fitted according to Equ. 5.8.

Figure 5.5 shows anomalous and planar Hall effect data used in the calculations. Figure 5.5(a) shows the anomalous Hall effect for a sample with 11 nm of $Ni_{20}Fe_{80}$, with a linear fit yielding $(157\pm1)\,\Omega$ for $\partial R_{\mathrm{AHE}}/\partial H$. Scaling this using the ratio of thicknesses of the ferromagnetic layer (17 nm/11 nm), to account for the extra magnetic ions resulting in a stronger AHE, yields a value of $(242\pm1)\,\Omega$ for the sample measured for the PHE. The dip seen in the centre of Fig. 5.5(a) can be explained due to either issues with the magnet power supply at low fields, or other similar effects in the measurement setup around the field reversal point. These points were considered anomalous and excluded from the fit.

Parameter	Gradient ($\mathbf{m\Omega\,mA^{-1}}$)	Intercept ($\mathbf{m\Omega}$)
A	-0.051±0.02	0.32±0.07
B	0.053±0.003	-0.02±0.01
C	0.02±0.01	0.01±0.03
$B-C$	0.04±0.01	-0.03±0.04

Table 5.1: Table of fitting parameters for the lines of best fit for the PHE parameters shown in Fig. 5.6.

Figure 5.5(b) shows the PHE measurements at multiple currents for a sample with a layer structure of 8 nm-17 nm of Bi_2Te_3 and $Ni_{20}Fe_{80}$, respectively. This data is shown fitted using Equ. 5.8, with plots of the fitting parameters against applied current shown in Fig. 5.6. These parameters themselves can be fitted to show how they vary with current, with B and C holding particular significance, with the difference between the two being equal to $2(\partial R_{\mathrm{AHE}}/\partial H)H_{\mathrm{OOP}}$, which can be shown via Equ. 5.7. The parameters from these fits are shown in Table 5.1, with the value of $B-C$ at 12 mA being used to find a value for H_{OOP}, resulting in a value of (0.93±0.34) mT.

Parameter	Value
$B-C$ at 12 mA	450±160 $\mu\Omega$
$\frac{\partial R_{\mathrm{AHE}}}{\partial H_z}$	242±1 $\mathrm{m\Omega\,T^{-1}}$
H_{OOP}	0.93±0.34 mT
t_{FM}	17±2 nm
w_{Hall}	57±5 μm
M_S	(6.38±0.82)×10^5 $\mathrm{A\,m^{-1}}$
ρ_{TI}	0.67±0.10 $\mu\Omega$ mm
ρ_{FM}	1.2±0.1 $\mu\Omega$ mm
J_{TI}	(6.9±5.0)×10^9 $\mathrm{A\,m^{-2}}$

Table 5.2: Table showing the parameters relevant to calculating the spin-Hall angle of the 8 nm-17 nm Bi_2Te_3-$Ni_{20}Fe_{80}$ bilayer. Each of these values is explained in the Section 5.4.

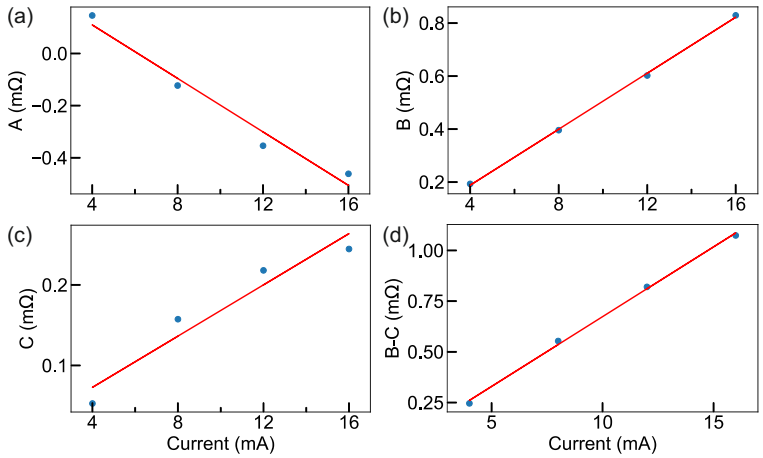


Figure 5.6: Fitting parameters from Fig. 5.5. (a) Plot of the parameter A against current, a correction for device asymmetry. (b, c) Graph of the parameters B and C, respectively, which are coefficients for the Sine functions shown in Equ. 5.8, with their physical meanings shown in Equ. 5.7. (d) Displays the difference of parameters B-C, which has a physical expression of $2(\partial R_{\mathrm{AHE}}/\partial H)H_{\mathrm{OOP}}$.

In addition to the parameters gained from AHE and PHE data fitting ($\partial R_{\mathrm{AHE}}/\partial H_z$ and $B - C = 2(\partial R_{\mathrm{AHE}}/\partial H)H_{\mathrm{OOP}}$, respectively), there are the geometric parameters of the device, with $t_{\mathrm{FM}} = (17\pm2)\,\mathrm{nm}$ being the thickness of the ferromagnetic layer and w_{Hall} is the width of the channel in the Hall bar. The former of these was measured via fitting XRR data, and the latter was determined using image analysis tools on a microscope in the cleanroom, an example of which is shown in the annotations of Fig. 5.3(a). Finally, there are the electric and magnetic properties of the film, with M_s being the magnetisation saturation of the device extracted from room temperature VSM $M(H)$ loop shown in Fig. 5.7. The remaining parameters were determined via control measurements on single-layer films to measure the resistivities of the TI and ferromagnetic layer (ρ_{TI} and ρ_{FM}), yielding results of $(0.67\pm0.1)\,\mu\Omega\,\mathrm{mm}$ and $(1.2\pm0.1)\,\mu\Omega\,\mathrm{mm}$ for the TI and FM layers, respectively. These values were then used to calculate the current

density in the TI, J_{TI}, by using the ratio of the resistivities of each layer to determine the proportion of the current that flows through the TI.

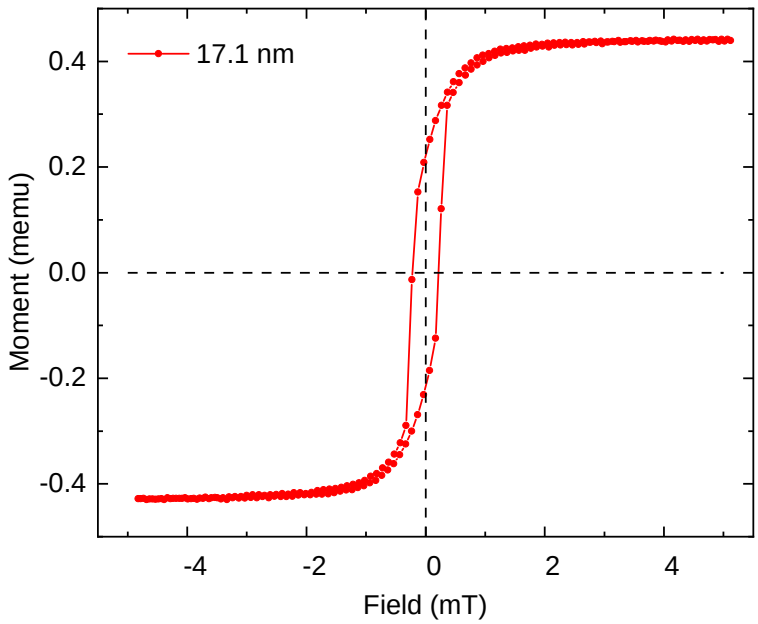


Figure 5.7: $M(H)$ loop of the TI-FM bilayer measured in the PHE data. This loop was used to measure the saturation magnetisation, giving a value of $(6.38\pm0.82)\times10^5\,\mathrm{A\,m^{-1}}$.

Substituting the values from Tables 5.2 and 5.1 into Equ. 5.2 yields a value of $\theta_{\mathrm{H}} = 4.4 \pm 5.7$, with the significant error coming from the uncertainty in the fitting of the PHE data, alongside the uncertainty in the thickness of the different layers, resulting in compounding error in the calculation of resistivities.

5.5 Discussion

In this chapter, we have shown that TI films produced via magnetron sputtering can exert torques on adjacent magnetic films, potentially allowing for future work in producing devices for spin switching of ferromagnetic layers. The value of $\theta_{\mathrm{H}} = 4.4 \pm 5.7$, compares similarly to the value of 2.88 ± 0.03 for a $\mathrm{Bi}_x\mathrm{Se}_{1-x}$-CoFeB heterostructure with an 8 nm

thick topological insulator layer obtained with planar Hall effect measurements [37]. This is promising given the Al spacer, which reduces coupling between layers by increasing the distance over which the torque operates. This suggests that the nanocrystalline film offers a minor performance increase; however, more precise measurements and a future systematic study of SOT against grain size would be required to confirm this.

Comparing to similar studies in literature in order to determine future improvements, thinner TI layers layers presented by Mahendra *et al.* exhibit spin Hall angles as high as 18.62 ± 0.13 at a layer thickness of 4 nm, with the significant increase observed attributed to an observed reduction in grain size from 18 nm to 6 nm between the 8 nm and 4 nm thick TI films [37]. Similar TI-FM systems report a range of values for θ_{H}, ranging from 0.01 to 52, with different systems and measurement methods yielding different results [148, 151]. Notably, the value of 52 was measured using a 'tilting magnetisation' method with a BiSb-based structure, without supporting planar Hall or Spin-Torque-Ferromagnetic Resonance (ST-FMR) measurements [148]. ST-FMR uses an RF current while sweeping an in-plane magnetic field to generate an oscillating torque. This results in the magnetisation of the ferromagnetic layer oscillating and therefore oscillating resistance due to anisotropic magnetoresistance. This, in combination with both the RF current and oscillating resistance being detected at the output, with the symmetric and anti-symmetric parts allowing the calculation of the in-plane and out-of-plane torques exerted on the FM layer, leads to a determination of the spin Hall angle [37, 140, 146]. It should be noted that the 4 nm thick $\mathrm{Bi}_x\mathrm{Se}_{1-x}$-CoFeB heterostructure presented by Mahendra *et al.* yielded a lower value of $\theta_{\mathrm{H}} = 8.67 \pm 1.08$ when measured using the ST-FMR, showing the disagreement between different methodologies even on the same systems [148, 161, 162].

While this chapter has detailed the fabrication of Bi_2Te_3-$Ni_{20}Fe_{80}$ bilayers, yielding a comparatively high spin Hall angle despite the presence of the Al spacer layer, issues with the measurement setup limited further progress. As such, future work should be undertaken to reduce the uncertainty in the results presented in this chapter, which proved infeasible at the time due to a change in the measurement system that allowed more accurate ST-FMR measurements to be performed. This required re-patterning of films as new device architectures were introduced. These new devices proved difficult to produce, given the limited number of available films, as most had already been processed. Further growth was no longer an option, as the growth chamber had been reconfigured for other projects. This, accompanied by multiple changes in equipment, prevented a more systematic study from being conducted, hindering the exploration of factors such as grain size, film thickness, and material choice in the heterostructure.

Chapter 6

Conclusions

This thesis has focused on the incorporation of magnetic order into topological insulators using a variety of methods. Chapter 3 details the growth and characterisation of two different transition metal-doped TIs, Mn:Bi_2Te_3 and Cr:Sb_2Te_3. Growth was successful for both materials, but each presented unique challenges. Section 3.2 produced a series of films of different nominal Mn concentrations, exhibiting magnetic ordering with transitions at approximately 10 and 43.3 K, indicating that Mn is incorporated into the lattice non-uniformly. This was supported by the structural data, which showed secondary phases in XRD. At high Mn concentrations of 12%, the formation of a phase more similar to $MnBi_2Te_4$ can be observed. TEM data revealed several defects and off-axis growth, complemented by EDS and HAADF images that highlight areas of increased Mn concentration, thereby supporting the conclusion that secondary phases form in specific regions.

This appears to be the probable cause of the linearly decreasing moment with an increase in Mn concentration, as observed via peak asymmetry measured in XMCD. The mechanism for this is the formation of $MnTe_x$ secondary phases that order antiferromagnetically, as well as the increase in Mn, which enhances superexchange interactions

and results in a breakdown of long-range magnetic ordering. These effects could also be exacerbated by Mn situating itself in the van der Waals gap, potentially coupling to the substitutionally doped Mn ions. All of these effects explain the reduction in moment, and even the lowest Mn concentration sample (1.6%), aligns with this linear trend, suggesting that substitutional doping is saturated even at this low concentration. This work could be advanced in the future through the study of site-specific magnetic ordering to gain a more comprehensive understanding of Mn site preferences, of coupling interactions, and to estimate the doping limit. This could be achieved via neutron diffraction, comprehensive electron microscopy and X-ray photoelectron spectroscopy studies.

Section 3.3 shows that, like Mn-doped Bi_2Te_3, Cr-doped Sb_2Te_3 has a window of viable growth parameters that will produce ferromagnetic films, with discontinuities in dM/dT at ∼38 and 82 K, suggesting that once again two magnetic phases are present. These films were observed, via XMCD, to have a depth-dependent magnetic response, suggesting a surface Cr^{3+} character and a bulk Cr^{2+} character. Unlike the Mn-doped case, Cr doping does not appear to form ordered secondary phases at low concentrations, only exhibiting crystalline Cr_xTe_y above a 10% nominal dopant concentration. However, Sb_2Te_3 films presented unique structural challenges, with reciprocal space maps revealing that undoped films will occasionally grow with an unknown rotation from the expected c-plane lattice. Additionally, evidence of a narrow band of higher Cr content, combined with a drop in local Sb concentration, suggests there is potential for amorphous Cr_xTe_y to form. Both the rotation of the Sb_2Te_3 lattice and the Cr-rich layer require extensive TEM to characterise fully.

Chapter 4 explores the formation of $MnBi_2Te_4$ seen at high Mn concentrations in Section 3.2. This resulted in the growth of $MnBi_2Te_4$ thin films with various stoichiometries,

during which a non-linearity between sputter powers across different targets and element concentration was observed. Upon further investigation, it was found that an increase in Mn caused the film's structure to revert to a weakly ordered Bi_2Te_3 state, rather than $MnBi_2Te_4$. This structural difference results in changes in magnetic properties, with both films exhibiting ferromagnetic ordering with a T_C of $\sim$30 K. However, a film with correct stoichiometry shows a second transition visible at $\sim$8 K, indicative of a possible antiferromagnetic transition. Unfortunately, when measured on XMLD, these films show no reliable response. This means that despite the films' near nanometre surface roughness, antiferromagnetic order cannot be observed with X-ray magnetic spectroscopy. The cause of this is uncertain; although the film shows few signs of secondary phase formation, it appears that the magnetic ordering is extremely sensitive to disorder within the film. Lattice defects commonly present in sputtered films, combined with interstitial and substitutionally doped Mn, could disrupt the superexchange pathway required for A-type antiferromagnetism. This seems to be sufficient to suppress long-range magnetic ordering in the film while preserving atomic-scale magnetism. Refinements to the annealing process, capping to prevent Te desorption and improving substrate matching could improve composition and crystallinity such that antiferromagnetic order is stable enough for XMLD measurements to be successfully undertaken in thin film $MnBi_2Te_4$.

Chapter 5 presents SOT measurements of a Bi_2Te_3-$Ni_{20}Fe_{80}$ bilayer device, showing that nanocrystalline topological insulators can display competitive SOTs when compared to similar devices, with a spin Hall angle of $\theta_H = 4.4 \pm 5.7$. This is a very positive result, as the presence of a sub-nanometre Al spacer layer, grown to prevent intermixing between the TI and FM layers, will probably reduce coupling between the layers. However, these results are not conclusive. High errors arise from the planar Hall effect method used and

repeat measurements were limited by the number of available samples and the relatively high current densities required, which increased the risk of device burn out. Therefore, expanding the work with a new batch of films, improving device fabrication, and utilising ST-FMR measurements for more precise results could allow the performance of the nanocrystalline TIs to be systematically explored. Steps to achieve this have already been taken, with a set-up capable of ST-FMR measurements installed for future studies. This required a new device geometry that offers both a higher density of devices per film and does not rely on wire bonding, thanks to an adjustable sample stage with pins that connect to RF cables. While other growth projects took priority for this thesis, all the necessary equipment is now in place to advance this work further.

Overall, the exploration of magnetic order in topological insulator thin films has yielded promising results, with further refinement of growth parameters potentially enhancing compositional control and enable the fabrication of films with improved crystallinity. Furthermore, a comprehensive exploration of various TIs and dopants, such as $(Bi,Sb)_2(Te)_3$, could reveal an ideal system that optimally incorporates magnetic dopants. During the course of this thesis, there has been continued interest in magnetic TIs, including transition metal doped TIs for quantum computing [163], searching for new systems that exhibit topological surface states [164–166], and further explorations into the intrinsic magnetic topological insulator $MnBi_2Te_4$ [102, 167, 168]. In addition, further study of topological phases such as topological superconductivity, Majorana fermions [169–171], and Weyl semimetals [12, 158, 172, 173] is ongoing. This shows that there remains a strong impetus to study novel topological materials and phases, with the potential to explore new physics as well as applications in spintronics and quantum computing.

Appendix A

List of Acronyms and Abbreviations

1D	One Dimensional
2D	Two Dimensional
2DEG	Two Dimensional Electron Gas
3D	Three Dimensional
AFM	Atomic Force Microscopy
AHE	Anomalous Hall Effect
ARPES	Angle-Resolved Photoemission Spectroscopy
BF	Bright Field
CB	Conduction Band
EDS	Energy Dispersive X-ray Spectroscopy
EELS	Electron Energy Loss Spectroscopy
ESRF	European Synchrotron Radiation Facility
FIB	Focused Ion Beam
FM	Ferromagnet
FMR	Ferromagnetic Resonance
FY	Florescence Yield

GI-XRD	Grazing Incidence X-ray Diffraction
HAADF	High Angle Annular Dark Field
LY	Luminescence Yield
MBE	Molecular Beam Epitaxy
MTI	Magnetic Topological Insulator
PHE	Planar Hall Effect
QAHE	Quantum Anomalous Hall Effect
QHE	Quantum Hall Effect
QSHE	Quantum Spin Hall Effect
RIE	Reactive Ion Etching
RSM	Reciprocal Space Maps/Mapping
SBZ	Surface Brillion Zone
SEM	Scanning Electron Microscopy
SHE	Spin Hall Effect
SOC	Spin-Orbit Coupling
SOT	Spin-Orbit Torque
SQUID	Superconducting Quantum Interference Device
STEM	Scanning Transmission Electron Microscopy
ST-FMR	Spin-Torque-Ferromagnetic Resonance
TEM	Transmission Electron Microscopy
TEY	Total Electron Yield
TI	Topological Insulator
TRIM	Time-Reversal Invariant Momenta
TRS	Time Reversal Symmetry

VB	Valence Band
VSM	Vibrating Sample Magnetometry
XMCD	X-ray Magnetic Circular Dichroism
XMLD	X-ray Magnetic Linear Dichroism
XRD	X-ray Diffraction
XRR	X-ray Reflectivity

Appendix B

Details on the Preparation of Substrates

Substrates were shipped as pre-cut 2-inch wafers, arriving coated in adhesive on the unpolished side and a protective polymer coating on the polished side. To completely remove these substances from the substrate and provide a clean, smooth surface for growth, a multi-step process using different solvents is required. This process used both hot and cold solvents and followed the following steps:

- Boil in Acetone for 3 minutes.
- Sonicate in cold Acetone for 3 minutes.
- Boil in Isopropanol for 3 minutes.
- Sonicate in cold Isopropanol for 3 minutes.
- Boil in Methanol for 3 minutes.
- Sonicate in cold Methanol for 3 minutes.
- Sonicate in cold deionised water for 3 minutes.

- Dry using nitrogen gas

The solvents were boiled on a hot plate, and each stage used a different piece of glassware to limit cross-contamination from the previous stage of cleaning. The nitrogen drying ensured minimal amounts of solvent were degassed into the chamber.

Bibliography

[1] C. L. Kane and E. J. Mele, Phys. Rev. Lett. **95**, 146802 (2005).

[2] C. L. Kane and E. J. Mele, Phys. Rev. Lett. **95**, 226801 (2005).

[3] Y. Zhang, Y.-W. Tan, H. L. Stormer, and P. Kim, Nature **438**, 201 (2005).

[4] B. A. Bernevig and S.-C. Zhang, Phys. Rev. Lett. **96**, 106802 (2006).

[5] F. D. M. Haldane, Phys. Rev. Lett. **61**, 2015 (1988).

[6] R. B. Laughlin, Phys. Rev. Lett. **50**, 1395 (1983).

[7] C.-Z. Chang, J. Zhang, X. Feng, J. Shen, Z. Zhang, M. Guo, K. Li, Y. Ou, P. Wei, L.-L. Wang, Z.-Q. Ji, Y. Feng, S. Ji, X. Chen, J. Jia, X. Dai, Z. Fang, S.-C. Zhang, K. He, Y. Wang, L. Lu, X.-C. Ma, and Q.-K. Xue, Science **340**, 167 (2013).

[8] L. Fu and C. L. Kane, Phys. Rev. Lett. **100**, 096407 (2008).

[9] L. Fu and C. L. Kane, Phys. Rev. Lett. **102**, 216403 (2009).

[10] D. Pesin and A. H. MacDonald, Nat. Mater. **11**, 409 (2012).

[11] H. Wang, H. Wu, J. Zhang, Y. Liu, D. Chen, C. Pandey, J. Yin, D. Wei, N. Lei, S. Shi, H. Lu, P. Li, A. Fert, K. L. Wang, T. Nie, and W. Zhao, Nat. Commun. **14**, 5173 (2023).

[12] B. A. Bernevig, C. Felser, and H. Beidenkopf, Nature **603**, 41 (2022).

[13] Q. L. He, T. L. Hughes, N. P. Armitage, Y. Tokura, and K. L. Wang, Nat. Mater. **21**, 15 (2022).

[14] Y. S. Hor, P. Roushan, H. Beidenkopf, J. Seo, D. Qu, J. G. Checkelsky, L. A. Wray, D. Hsieh, Y. Xia, S. Y. Xu, D. Qian, M. Z. Hasan, N. P. Ong, A. Yazdani, and R. J. Cava, Phys. Rev. B **81**, 195203 (2010).

[15] M. D. Watson, L. J. Collins-McIntyre, L. R. Shelford, A. I. Coldea, D. Prabhakaran, S. C. Speller, T. Mousavi, C. R. M. Grovenor, Z. Salman, S. R. Giblin, G. van der Laan, and T. Hesjedal, New J. Phys. **15**, 103016 (2013).

[16] J. S. Lee, A. Richardella, D. W. Rench, R. D. Fraleigh, T. C. Flanagan, J. A. Borchers, J. Tao, and N. Samarth, Phys. Rev. B **89**, 174425 (2014).

[17] T. P. Ginley, Y. Wang, and S. Law, Crystals **6**, 154 (2016).

[18] K. Carva, J. Kudrnovský, F. Máca, V. Drchal, I. Turek, P. Baláž, V. Tkáč, V. Holý, V. Sechovský, and J. Honolka, Phys. Rev. B **93**, 214409 (2016).

[19] S. Hosokawa, J. R. Stellhorn, T. Matsushita, N. Happo, K. Kimura, K. Hayashi, Y. Ebisu, T. Ozaki, H. Ikemoto, H. Setoyama, T. Okajima, Y. Yoda, H. Ishii, Y.-F. Liao, M. Kitaura, and M. Sasaki, Phys. Rev. B **96**, 214207 (2017).

[20] V. N. Antonov, L. V. Bekenov, S. Uba, and A. Ernst, Phys. Rev. B **96**, 224434 (2017).

[21] D. Zhang, A. Richardella, D. W. Rench, S.-Y. Xu, A. Kandala, T. C. Flanagan, H. Beidenkopf, A. L. Yeats, B. B. Buckley, P. V. Klimov, D. D. Awschalom,

A. Yazdani, P. Schiffer, M. Z. Hasan, and N. Samarth, Phys. Rev. B **86**, 205127 (2012).

[22] J. Teng, N. Liu, and Y. Li, J. Semicond. **40**, 081507 (2019).

[23] N. M. A. Hadia, S. H. Mohamed, W. S. Mohamed, M. Alzaid, M. T. Khan, and M. A. Awad, J. Mater. Sci.: Mater. Electron. **33**, 158 (2022).

[24] N. S. Kander, S. Islam, S. Guchhait, and A. K. Das, Appl. Phys. A **129**, 253 (2023).

[25] R. Yu, W. Zhang, H.-J. Zhang, S.-C. Zhang, X. Dai, and Z. Fang, Science **329**, 61 (2010).

[26] J.-M. Zhang, W. Ming, Z. Huang, G.-B. Liu, X. Kou, Y. Fan, K. L. Wang, and Y. Yao, Phys. Rev. B **88**, 235131 (2013).

[27] X. Kou, M. Lang, Y. Fan, Y. Jiang, T. Nie, J. Zhang, W. Jiang, Y. Wang, Y. Yao, L. He, and K. L. Wang, ACS Nano **7**, 9205 (2013).

[28] M. Ye, W. Li, S. Zhu, Y. Takeda, Y. Saitoh, J. Wang, H. Pan, M. Nurmamat, K. Sumida, F. Ji, Z. Liu, H. Yang, Z. Liu, D. Shen, A. Kimura, S. Qiao, and X. Xie, Nat. Commun. **6**, 8913 (2015).

[29] A. Tcakaev, V. B. Zabolotnyy, R. J. Green, T. R. F. Peixoto, F. Stier, M. Dettbarn, S. Schreyeck, M. Winnerlein, R. C. Vidal, S. Schatz, H. B. Vasili, M. Valvidares, K. Brunner, C. Gould, H. Bentmann, F. Reinert, L. W. Molenkamp, and V. Hinkov, Phys. Rev. B **101**, 045127 (2020).

[30] Y. H. Choi, N. H. Jo, K. J. Lee, J. B. Yoon, C. Y. You, and M. H. Jung, J. Appl. Phys. **109**, 07E312 (2011).

[31] W. Zhao, D. Cortie, L. Chen, Z. Li, Z. Yue, and X. Wang, Phys. Rev. B **99**, 165133 (2019).

[32] A. I. Figueroa, G. van der Laan, L. J. Collins-McIntyre, G. Cibin, A. J. Dent, and T. Hesjedal, J. Phys. Chem. C **119**, 17344 (2015).

[33] L. B. Abdalla, L. Seixas, T. M. Schmidt, R. H. Miwa, and A. Fazzio, Phys. Rev. B **88**, 045312 (2013).

[34] B. Deng, Y. Zhang, S. B. Zhang, Y. Wang, K. He, and J. Zhu, Phys. Rev. B **94**, 054113 (2016).

[35] S. E. Harrison, P. Schönherr, T. Hesjedal, Y. Huo, and J. S. Harris, Appl. Phys. Lett. **105**, 153114 (2014).

[36] P. Schönherr, D. Kojda, V. Srot, S. F. Fischer, P. A. van Aken, and T. Hesjedal, APL Mater. **5**, 086110 (2017).

[37] M. DC, R. Grassi, J.-Y. Chen, M. Jamali, D. R. Hickey, D. Zhang, Z. Zhao, H. Li, P. Quarterman, Y. Lv, M. Li, A. Manchon, K. A. Mkhoyan, T. Low, and J.-P. Wang, Nat. Mater. **17**, 800 (2018).

[38] K. v. Klitzing, G. Dorda, and M. Pepper, Phys. Rev. Lett. **45**, 494 (1980).

[39] K. v. Klitzing, Physica B+C **126**, 242 (1984).

[40] I. Žutić, J. Fabian, and S. D. Sarma, Rev. Mod. Phys. **76**, 323 (2004).

[41] T. Jungwirth, J. Wunderlich, and K. Olejník, Nat. Mater. **11**, 382 (2012).

[42] M. I. D'yakonov and V. I. Perel', JETP Lett. **13**, 467 (1971).

[43] M. I. Dyakonov and V. I. Perel, Phys. Lett. A **35**, 459 (1971).

[44] N. Nagaosa, J. Sinova, S. Onoda, A. H. MacDonald, and N. P. Ong, Rev. Mod. Phys. **82**, 1539 (2010).

[45] X.-L. Qi and S.-C. Zhang, Phys. Today **63**, 33 (2010).

[46] B. A. Bernevig, T. L. Hughes, and S.-C. Zhang, Science **314**, 1757 (2006).

[47] M. König, S. Wiedmann, C. Brüne, A. Roth, H. Buhmann, L. W. Molenkamp, X.-L. Qi, and S.-C. Zhang, Science **318**, 766 (2007).

[48] P. Hofmann, in *Magnetism and Synchrotron Radiation: Towards the Fourth Generation Light Sources*, edited by E. Beaurepaire, H. Bulou, L. Joly, and F. Scheurer (Springer International Publishing, Cham, 2013) pp. 211–238.

[49] F. Reinert, G. Nicolay, S. Schmidt, D. Ehm, and S. Hüfner, Phys. Rev. B **63**, 115415 (2001).

[50] E. I. Rashba, Sov. Phys. Solid State **2**, 1109 (1960).

[51] Y. A. Bychkov and E. I. Rashba, J. Phys. C: Solid State Phys. **17**, 6039 (1984).

[52] H. A. Kramers, Koninkl. Ned. Akad. Wetenschap. Proc. 33 959 (1930).

[53] E. Wigner, *Group theory: and its application to the quantum mechanics of atomic spectra*, Vol. 5 (Elsevier, 1959).

[54] Y. L. Chen, J. H. Chu, J. G. Analytis, Z. K. Liu, K. Igarashi, H. H. Kuo, X. L. Qi, S. K. Mo, R. G. Moore, D. H. Lu, M. Hashimoto, T. Sasagawa, S. C. Zhang, I. R. Fisher, Z. Hussain, and Z. X. Shen, Science **329**, 659 (2010).

[55] D. Hsieh, Y. Xia, L. Wray, D. Qian, A. Pal, J. H. Dil, J. Osterwalder, F. Meier, G. Bihlmayer, C. L. Kane, Y. S. Hor, R. J. Cava, and M. Z. Hasan, Science **323**, 919 (2009).

[56] I. N. Karnaukhov, Phys. Lett. A **381**, 1967 (2017).

[57] C.-Z. Chang, P. Wei, and J. S. Moodera, MRS Bulletin **39**, 867 (2014).

[58] J. Sarkar, Chapter 2 - sputtering and thin film deposition, in *Sputtering Materials for VLSI and Thin Film Devices* (William Andrew Publishing, Boston, 2014) pp. 93–170.

[59] G. S. Anderson, W. N. Mayer, and G. K. Wehner, J. Appl. Phys. **33**, 2991 (1962).

[60] G. F. Harrington and J. Santiso, J. Electroceram. **47**, 141 (2021).

[61] S. Dolabella, A. Borzì, A. Dommann, and A. Neels, Small Methods **6**, 2100932 (2022).

[62] J. Bibby, A. Singh, E. Heppell, J. Bollard, B. Achinuq, S. J. Haigh, G. Van Der Laan, and T. Hesjedal, Crystals **15**, 54 (2025).

[63] J. Als-Nielsen and D. McMorrow, in *In Elements of Modern X-ray Physics* (John Wiley Sons, Ltd, 2011) pp. 69–112.

[64] M. Yasaka, Rikaku J. **26** (2010).

[65] R. C. Jaklevic, J. Lambe, A. H. Silver, and J. E. Mercereau, Phys. Rev. Lett. **12**, 159 (1964).

[66] A. I. Figueroa, in *Magnetic Nanoparticles: A Study by Synchrotron Radiation and RF Transverse Susceptibility* (Springer International Publishing, Cham, 2015) pp. 13–30.

[67] G. van der Laan and A. I. Figueroa, Coordin. Chem. Rev. **277-278**, 95 (2014).

[68] G. van der Laan, Phys. Rev. Lett. **82**, 640 (1999).

[69] P. Kuiper, B. G. Searle, P. Rudolf, L. H. Tjeng, and C. T. Chen, Phys. Rev. Lett. **70**, 1549 (1993).

[70] E. Arenholz, G. van der Laan, R. V. Chopdekar, and Y. Suzuki, Phys. Rev. B **74**, 094407 (2006).

[71] G. van der Laan and B. T. Thole, Phys. Rev. B **43**, 13401 (1991).

[72] B. T. Thole, P. Carra, F. Sette, and G. van der Laan, Phys. Rev. Lett. **68**, 1943 (1992).

[73] P. Carra, B. T. Thole, M. Altarelli, and X. Wang, Phys. Rev. Lett. **70**, 694 (1993).

[74] K. W. Edmonds, N. R. S. Farley, T. K. Johal, G. Van Der Laan, R. P. Campion, B. L. Gallagher, and C. T. Foxon, Phys. Rev. B **71**, 064418 (2005).

[75] I. Boulares, G. Shi, E. Kioupakis, P. Lošťák, C. Uher, and R. Merlin, Solid State Commun. **271**, 1 (2018).

[76] S. E. Harrison, S. Li, Y. Huo, B. Zhou, Y. L. Chen, and J. S. Harris, Appl. Phys. Lett. **102**, 171906 (2013).

[77] Y. Zhao, C.-Z. Chang, Y. Jiang, A. DaSilva, Y. Sun, H. Wang, Y. Xing, Y. Wang, K. He, X. Ma, Q.-K. Xue, and J. Wang, Sci. Rep. **3**, 3060 (2013).

[78] N. S. Kander, S. Biswas, S. Guchhait, T. Singha, and A. K. Das, J. Mater. Sci.: Mater. Electron. **34**, 1198 (2023).

[79] L. Collins-McIntyre, *Transition-metal doped Bi2Se3 and Bi2Te3 topological insulator thin films*, Ph.D. thesis, Oxford University, UK (2015).

[80] L. Duffy, *Magnetic order in three-dimensional topological insulators*, Ph.D. thesis, University of Oxford (2018).

[81] J. H. Yao, K. R. Elder, H. Guo, and M. Grant, Phys. Rev. Lett. **47**, 14110 (1993).

[82] P. W. Voorhees, J. Stat. Phys. **38**, 231 (1985).

[83] S.-Y. Xu, M. Neupane, C. Liu, D. Zhang, A. Richardella, L. A. Wray, N. Alidoust, M. Leandersson, T. Balasubramanian, J. Sánchez-Barriga, O. Rader, G. Landolt, B. Slomski, J. H. Dil, J. Osterwalder, T.-R. Chang, H.-T. Jeng, H. Lin, A. Bansil, N. Samarth, and M. Z. Hasan, Nat. Phys. **8**, 616 (2012).

[84] A. Singh, V. S. Kamboj, J. Liu, J. Llandro, L. B. Duffy, S. P. Senanayak, H. E. Beere, A. Ionescu, D. A. Ritchie, and T. Hesjedal, Sci. Rep. **8**, 17024 (2018).

[85] N.-J. Steinke, S. L. Zhang, P. J. Baker, L. B. Duffy, F. Kronast, J. Krieger, Z. Salman, T. Prokscha, A. Suter, and S. Langridge, Phys. Rev. B **106**, 224425 (2022).

[86] Q. Lu, P. Li, Z. Guo, G. Dong, B. Peng, X. Zha, T. Min, Z. Zhou, and M. Liu, Nat. Commun. **13**, 1650 (2022).

[87] H. Lu, Y. Huang, Q. Guo, K. Wang, M. He, Z. Yin, D. Wang, T. Liu, J. Wang, G. Yu, and J. Teng, J. Phys. D: Appl. Phys. **56**, 045302 (2023).

[88] V. S. Vinila, J. Isac, S. Thomas, N. Kalarikkal, and A. R. Abraham, in *Design, Fabrication, and Characterization of Multifunctional Nanomaterials* (Elsevier, 2022) pp. 319–341.

[89] L. J. Collins-McIntyre, M. D. Watson, A. A. Baker, S. L. Zhang, A. I. Coldea, S. E. Harrison, A. Pushp, A. J. Kellock, S. S. P. Parkin, G. van der Laan, and T. Hesjedal, AIP Adv. **4**, 127136 (2014).

[90] Y. H. Choi, N. H. Jo, K. J. Lee, H. W. Lee, Y. H. Jo, J. Kajino, T. Takabatake, K.-T. Ko, J.-H. Park, and M. H. Jung, Appl. Phys. Lett. **101**, 152103 (2012).

[91] Y.-P. Zhu, X. Chen, X.-R. Liu, Y. Liu, P. Liu, H. Zha, G. Qu, C. Hong, J. Li, Z. Jiang, X.-M. Ma, Y.-J. Hao, M.-Y. Zhu, W. Liu, M. Zeng, S. Jayaram, M. Lenger, J. Ding, S. Mo, K. Tanaka, M. Arita, Z. Liu, M. Ye, D. Shen, J. Wrachtrup, Y. Huang, R.-H. He, S. Qiao, Q. Liu, and C. Liu, Nature **626**, 523 (2024).

[92] Y. Tokura, K. Yasuda, and A. Tsukazaki, Nat. Rev. Phys. **1**, 126 (2019).

[93] A. I. Figueroa, T. Hesjedal, and N.-J. Steinke, Appl. Phys. Lett. **117**, 150502 (2020).

[94] J. Bibby, A. Singh, E. Heppell, J. Bollard, B. Achinuq, J. A. do Nascimento, C. Murrill, V. K. Lazarov, G. van der Laan, and T. Hesjedal, Crystals **15**, 896 (2026).

[95] A. I. Figueroa, G. Van der Laan, L. J. Collins-McIntyre, S.-L. Zhang, A. A. Baker, S. E. Harrison, P. Schönherr, G. Cibin, and T. Hesjedal, Phys. Rev. B **90**, 134402 (2014).

[96] D. Zhang, M. Shi, T. Zhu, D. Xing, H. Zhang, and J. Wang, Phys. Rev. Lett. **122**, 206401 (2019).

[97] M. M. Otrokov, I. I. Klimovskikh, H. Bentmann, D. Estyunin, A. Zeugner, Z. S. Aliev, S. Gaß, A. U. B. Wolter, A. V. Koroleva, A. M. Shikin, M. Blanco-Rey, M. Hoffmann, I. P. Rusinov, A. Y. Vyazovskaya, S. V. Eremeev, Y. M. Koroteev, V. M. Kuznetsov, F. Freyse, J. Sánchez-Barriga, I. R. Amiraslanov, M. B. Babanly, N. T. Mamedov, N. A. Abdullayev, V. N. Zverev, A. Alfonsov, V. Kataev, B. Büchner, E. F. Schwier, S. Kumar, A. Kimura, L. Petaccia, G. Di Santo, R. C. Vidal, S. Schatz, K. Kißner, M. Ünzelmann, C. H. Min, S. Moser, T. R. F. Peixoto, F. Reinert, A. Ernst, P. M. Echenique, A. Isaeva, and E. V. Chulkov, Nature **576**, 416 (2019).

[98] S. Li, T. Liu, C. Liu, Y. Wang, H.-Z. Lu, and X. C. Xie, Natl. Sci. Rev. **11**, nwac296 (2024).

[99] J. Li, Y. Li, S. Du, Z. Wang, B.-L. Gu, S.-C. Zhang, K. He, W. Duan, and Y. Xu, Sci. Adv. **5**, 5685 (2019).

[100] C. Lei and A. H. MacDonald, Phys. Rev. B **108**, 125424 (2023).

[101] Q. Li, S.-K. Mo, and M. T. Edmonds, Nanoscale **16**, 14247 (2024).

[102] A. Y. Vyazovskaya, M. Bosnar, E. V. Chulkov, and M. M. Otrokov, Commun. Mater. **6**, 88 (2025).

[103] A. Bib, F. Nietschke, A. U. B. Wolter, S. Gaß, R. C. Vidal, T. R. F. Peixoto, D. Pohl, C. Damm, A. Lubk, R. Hentrich, S. K. Moser, C. Fornari, C. H. Min, S. Schatz, K. Kißner, M. Ünzelmann, M. Kaiser, F. Scaravaggi, B. Rellinghaus,

K. Nielsch, C. Hess, B. Büchner, F. Reinert, H. Bentmann, O. Oeckler, T. Doert, M. Ruck, and A. Isaeva, Chem. Mater. **31**, 2795 (2019).

[104] P. Chen, Q. Yao, J. Xu, Q. Sun, A. J. Grutter, P. Quarterman, P. P. Balakrishnan, C. J. Kinane, A. J. Caruana, S. Langridge, A. Li, B. Achinuq, E. Heppell, Y. Ji, S. Liu, B. Cui, J. Liu, P. Huang, Z. Liu, G. Yu, F. Xiu, T. Hesjedal, J. Zou, X. Han, H. Zhang, Y. Yang, and X. Kou, Nat. Electron. **6**, 18 (2023).

[105] Y. Bai, Y. Li, J. Luan, R. Liu, W. Song, Y. Chen, P.-F. Ji, Q. Zhang, F. Meng, and B. Tong, Natl. Sci. Rev. **11**, nwad189 (2024).

[106] Y. Shi, Y. Bai, Y. Li, Y. Feng, Q. Li, H. Zhang, Y. Chen, Y. Tong, J. Luan, and R. Liu, Phys. Rev. Mater. **8**, 124202 (2024).

[107] P. Wang, J. Ge, J. Li, Y. Liu, Y. Xu, and J. Wang, Innovation **2**, 100098 (2021).

[108] S. Li, M. Gong, S. Cheng, H. Jiang, and X. C. Xie, Natl. Sci. Rev. **11**, nwad262 (2024).

[109] T. Jansen, E. Kochetkova, A. Isaeva, A. Brinkman, and C. Li, Commun. Mater. **5**, 214 (2024).

[110] K. He, npj Quantum Mater. **5**, 90 (2020).

[111] J. Bibby, E. Heppell, J. Bollard, E. L. Arnold, J. Herrero-Martín, G. van der Laan, and T. Hesjedal, Phys. Status Solidi - Rapid Res. Lett. , 10:e2500329 (2025).

[112] J. Kampmeier, S. Borisova, L. Plucinski, M. Luysberg, G. Mussler, and D. Grützmacher, Cryst. Growth Des. **15**, 390 (2015).

[113] L. J. Collins-McIntyre, S. E. Harrison, P. Schönherr, N.-J. Steinke, C. J. Kinane, T. R. Charlton, D. Alba-Veneroa, A. Pushp, A. J. Kellock, S. S. P. Parkin, J. S. Harris, S. Langridge, G. van der Laan, and T. Hesjedal, Europhys. Lett. **107**, 57009 (2014).

[114] J. Sun, S. Liu, F. Xiu, and W. Liu, in *2024 IEEE International Magnetic Conference - Short papers (INTERMAG Short papers)* (2024) pp. 1–2.

[115] J.-Q. Yan, Q. Zhang, T. Heitmann, Z. Huang, K. Y. Chen, J.-G. Cheng, W. Wu, D. Vaknin, B. C. Sales, and R. J. McQueeney, Phys. Rev. Mater. **3**, 064202 (2019).

[116] H. Tan and B. Yan, Phys. Rev. Lett. **130**, 126702 (2023).

[117] X. Wu, C. Ruan, P. Tang, F. Kang, W. Duan, and J. Li, Nano Lett. **23**, 5048 (2023).

[118] C. Bigi, L. Qiao, C. Liu, P. Barone, M. C. Hatnean, G.-R. Siemann, B. Achinuq, D. A. Mayoh, G. Vinai, and V. Polewczyk, Phys. Rev. B **108**, 054419 (2023).

[119] E. L. Arnold, J. M. Riley, L. B. Duffy, A. I. Figueroa, R. Held, K. M. Shen, D. G. Schlom, P. D. C. King, M. Hoesch, and G. van der Laan, Phys. Rev. Mater. **9**, 024410 (2025).

[120] S. K. Sharma, H. R. Prakash, S. Ram, and D. Pradhan, AIP Conf. Proc. **1942**, 130044 (2018).

[121] B. A. Jensen, W. Tang, X. Liu, A. I. Nolte, G. Ouyang, K. W. Dennis, and J. Cui, Acta Mater. **181**, 595 (2019).

[122] K. Vero and J. P. Borah, Sci. Rep. **14**, 19015 (2024).

[123] J. Sitnicka, K. Park, P. Skupiński, K. Grasza, A. Reszka, K. Sobczak, J. Borysiuk, Z. Adamus, M. Tokarczyk, A. Avdonin, I. Fedorchenko, I. Abaloszewa, S. Turczyniak-Surdacka, N. Olszowska, J. Kołodziej, B. J. Kowalski, H. Deng, M. Konczykowski, L. Krusin-Elbaum, and A. Wołoś, 2D Mater. **9**, 15026 (2021).

[124] J. C. Slonczewski, J. Magn. Magn. Mater. **159**, L1 (1996).

[125] L. Berger, Phys. Rev. B **54**, 9353 (1996).

[126] V. M. Edelstein, Solid State Commun. **73**, 233 (1990).

[127] J.-i. Inoue, G. E. W. Bauer, and L. W. Molenkamp, Phys. Rev. B **67**, 033104 (2003).

[128] D. Awschalom and N. Samarth, Physics **2**, 50 (2009).

[129] I. Adagideli, G. E. W. Bauer, and B. I. Halperin, Phys. Rev. Lett. **97**, 256601 (2006).

[130] A. Manchon and S. Zhang, Phys. Rev. B **78**, 212405 (2008).

[131] A. Manchon and S. Zhang, Phys. Rev. B **79**, 094422 (2009).

[132] K. Obata and G. Tatara, Phys. Rev. B **77**, 214429 (2008).

[133] I. Mihai Miron, G. Gaudin, S. Auffret, B. Rodmacq, A. Schuhl, S. Pizzini, J. Vogel, and P. Gambardella, Nat. Mater. **9**, 230 (2010).

[134] T. Nan, S. Emori, C. T. Boone, X. Wang, T. M. Oxholm, J. G. Jones, B. M. Howe, G. J. Brown, and N. X. Sun, Phys. Rev. B **91**, 214416 (2015).

[135] Y.-C. Lau, D. Betto, K. Rode, J. M. D. Coey, and P. Stamenov, Nat. Nanotech. **11**, 758 (2016).

[136] I. M. Miron, K. Garello, G. Gaudin, P.-J. Zermatten, M. V. Costache, S. Auffret, S. Bandiera, B. Rodmacq, A. Schuhl, and P. Gambardella, Nature **476**, 189 (2011).

[137] L. Liu, C.-F. Pai, Y. Li, H. W. Tseng, D. C. Ralph, and R. A. Buhrman, Science **336**, 555 (2012).

[138] C. O. Avci, K. Garello, C. Nistor, S. Godey, B. Ballesteros, A. Mugarza, A. Barla, M. Valvidares, E. Pellegrin, and A. Ghosh, Phys. Rev. B **89**, 214419 (2014).

[139] K. Ando, S. Takahashi, K. Harii, K. Sasage, J. Ieda, S. Maekawa, and E. Saitoh, Phys. Rev. Lett. **101**, 036601 (2008).

[140] L. Liu, T. Moriyama, D. C. Ralph, and R. A. Buhrman, Phys. Rev. Lett. **106**, 036601 (2011).

[141] A. Dyrdał and J. Barnaś, Phys. Rev. B **92**, 165404 (2015).

[142] D. MacNeill, G. M. Stiehl, M. H. D. Guimaraes, N. D. Reynolds, R. A. Buhrman, and D. C. Ralph, Phys. Rev. B **96**, 054450 (2017).

[143] P. Li, W. Wu, Y. Wen, C. Zhang, J. Zhang, S. Zhang, Z. Yu, S. A. Yang, A. Manchon, and X.-x. Zhang, Nat. Commun. **9**, 3990 (2018).

[144] C.-W. Peng, W.-B. Liao, T.-Y. Chen, and C.-F. Pai, ACS Appl. Mater. Interfaces **13**, 15950 (2021).

[145] I.-H. Kao, R. Muzzio, H. Zhang, M. Zhu, J. Gobbo, S. Yuan, D. Weber, R. Rao, J. Li, and J. H. Edgar, Nat. Mater. **21**, 1029 (2022).

[146] A. R. Mellnik, J. S. Lee, A. Richardella, J. L. Grab, P. J. Mintun, M. H. Fischer,

A. Vaezi, A. Manchon, E.-A. Kim, N. Samarth, and D. C. Ralph, Nature **511**, 449 (2014).

[147] P. Deorani, J. Son, K. Banerjee, N. Koirala, M. Brahlek, S. Oh, and H. Yang, Phys. Rev. B **90**, 094403 (2014).

[148] N. H. D. Khang, Y. Ueda, and P. N. Hai, Nat. Mater. **17**, 808 (2018).

[149] E. Longo, L. Locatelli, M. Belli, M. Alia, A. Kumar, M. Longo, M. Fanciulli, and R. Mantovan, Adv. Mater. Interfaces **8**, 2101244 (2021).

[150] E. Longo, M. Belli, M. Alia, M. Rimoldi, R. Cecchini, M. Longo, C. Wiemer, L. Locatelli, P. Tsipas, A. Dimoulas, G. Gubbiotti, M. Fanciulli, and R. Mantovan, Adv. Funct. Mater. **32**, 2109361 (2022).

[151] A. Manchon, J. Železný, I. M. Miron, T. Jungwirth, J. Sinova, A. Thiaville, K. Garello, and P. Gambardella, Rev. Mod. Phys. **91**, 035004 (2019).

[152] J. C. Slonczewski, J. Magn. Magn. Mater. **247**, 324 (2002).

[153] A. R. Will-Cole, J. L. Hart, M. Matzelle, A. Podpirka, N. Bhattacharjee, S. K. Patel, S. H. Tolbert, A. Bansil, J. J. Cha, D. Heiman, and N. X. Sun, Phys. Rev. Mater. **7**, 024406 (2023).

[154] L. A. Walsh, C. M. Smyth, A. T. Barton, Q. Wang, Z. Che, R. Yue, J. Kim, M. J. Kim, R. M. Wallace, and C. L. Hinkle, J. Phys. Chem. C **121**, 23551 (2017).

[155] C.-F. Pai, Y. Ou, L. H. Vilela-Leão, D. C. Ralph, and R. A. Buhrman, Phys. Rev. B **92**, 064426 (2015).

[156] X. Fan, H. Celik, J. Wu, C. Ni, K.-J. Lee, V. O. Lorenz, and J. Q. Xiao, Nat. Commun. **5**, 3042 (2014).

[157] J. Kim, J. Sinha, M. Hayashi, M. Yamanouchi, S. Fukami, T. Suzuki, S. Mitani, and H. Ohno, Nat. Mater. **12**, 240 (2013).

[158] L. Medel Onofre and A. Martín-Ruiz, Phys. Rev. B **108**, 155132 (2023).

[159] A. A. Taskin, H. F. Legg, F. Yang, S. Sasaki, Y. Kanai, K. Matsumoto, A. Rosch, and Y. Ando, Nat. Commun. **8**, 1340 (2017).

[160] M. Kawaguchi, K. Shimamura, S. Fukami, F. Matsukura, H. Ohno, T. Moriyama, D. Chiba, and T. Ono, Appl. Phys. Express **6**, 113002 (2013).

[161] J. Han, A. Richardella, S. A. Siddiqui, J. Finley, N. Samarth, and L. Liu, Phys. Rev. Lett. **119**, 077702 (2017).

[162] Y. Wang, D. Zhu, Y. Wu, Y. Yang, J. Yu, R. Ramaswamy, R. Mishra, S. Shi, M. Elyasi, K.-L. Teo, Y. Wu, and H. Yang, Nat. Commun. **8**, 1364 (2017).

[163] Y. Liu, A. Lee, K. Qian, P. Zhang, Z. Xiao, H. He, Z. Ren, S. K. Cheung, R. Liu, and Y. Li, Nat. Mater. **24**, 559 (2025).

[164] T. Zhou, C. Xu, and W. Ren, Nat. Rev. Mater. , 1 (2025).

[165] X. Wu, Z. Chen, Y. Bai, B. Huang, Y. Dai, and C. Niu, Phys. Rev. B **109**, 235407 (2024).

[166] X. Wang, J. Wang, H. Ding, and M. Pan, Surf. Sci. Rep. **80**, 100660 (2025).

[167] S. Xu, Z. Shi, M. Yang, J. Zhang, H. Xu, H. Feng, N. Cheng, Q. Gao, J. Wang, and W. Hao, Phys. Rev. B **112**, 045124 (2025).

[168] C. Zhang, X. Lu, N. Wang, T. Huang, H. Zhang, N. Cao, A. Wang, X. Zhou, K. Watanabe, and T. Taniguchi, Nat. Commun. **16**, 5587 (2025).

[169] M. M. Sharma, P. Sharma, N. K. Karn, and V. P. S. Awana, Supercond. Sci. Technol. **35**, 083003 (2022).

[170] M. Mandal, N. C. Drucker, P. Siriviboon, T. Nguyen, A. Boonkird, T. N. Lamichhane, R. Okabe, A. Chotrattanapituk, and M. Li, Chem. Mater. **35**, 6184 (2023).

[171] D. Zhu, Z.-Y. Zhuang, Z. Wu, and Z. Yan, Phys. Rev. B **108**, 184505 (2023).

[172] Q. Lu, P. V. S. Reddy, H. Jeon, A. R. Mazza, M. Brahlek, W. Wu, S. A. Yang, J. Cook, C. Conner, and X. Zhang, Nat. Commun. **15**, 6001 (2024).

[173] M. Zhong, N. T. T. Vu, W. Zhai, J. R. Soh, Y. Liu, J. Wu, A. Suwardi, H. Liu, G. Chang, and K. P. Loh, Adv. Mater. **37**, 2506236 (2025).